2022

Dynamics and Turnover of Lipid and Protein Domains in Cells and Supported Bilayers

Alan Weisgerber
University of Denver

Recommended Citation

Weisgerber, Alan, "Dynamics and Turnover of Lipid and Protein Domains in Cells and Supported Bilayers" (2022). *Electronic Theses and Dissertations*. 2159.
https://digitalcommons.du.edu/etd/2159

Dynamics and Turnover of Lipid and Protein Domains in Cells and Supported Bilayers

Abstract

Protein and lipid clustering is an important mechanism for cell processes such as exo- and endo-cytosis and creating functional signaling complexes. It has been seen that both lipids and proteins are involved with the formation of cluster domains on cell membranes, yet little is known about the interplay between the two. In this work I began with visualizing lipid sorting to artificially induced curvature in supported lipid bilayers, with lipid tails affecting the sorting differently to curvature. These results demonstrate that lipids sort to curvature on curved, supported lipid bilayers. The sorting depends on the number of lipids in the tails with two-tailed lipids accumulating more at regions of curvature. The work then transitions to protein clustering. A plasma membrane SNAP Receptor (SNARE) protein, Syntaxin 1a (Syx1a), is known to cluster and these clusters are sites of membrane fusion in neuroendocrine cells. Syx1a was measured using dynamic measurements (FRAP and single molecule tracking), first by looking at substrate dye interactions to ensure dynamics were not altered by unintended interactions between dye and substrate. Following these studies it was determined that the commonly used poly-L-lysine substrate interacts with commonly used red fluorescent dye (Alexa Fluor 594), as a result Fibronectin is used for further studies. Single molecule dynamics of Syx1a at clusters using a novel system of nanobody interacting with enhanced green fluorescent protein (EGFP) labeled Syx1a reveals not only single molecule dynamics but cluster locations. Studies were performed to see how truncation of Syx1a affects mobility along with cholesterol depletions. Syx1a is more mobile at the center of clusters than elsewhere on the cell surface and that truncation of the Habc domain slightly slows this process. Removal of cholesterol greatly inhibited the motion at the cluster center and generally inhibited mobility thought the membrane. Overall, the work described within elucidates how clusters form on cell and synthetic membranes.

Document Type

Dissertation

Degree Name

Ph.D.

Department

Chemistry and Biochemistry

First Advisor

Michelle K. Knowles

Subject Categories

Biogeochemistry | Chemistry | Earth Sciences | Other Chemistry

Publication Statement

Dynamics and Turnover of Lipid and Protein Domains in Cells and Supported Bilayers

---

A Dissertation

Presented to

the Faculty of the College of Natural Sciences and Mathematics

University of Denver

In Partial Fulfillment

of the Requirements for the Degree

Doctor of Philosophy

---

by

Alan Weisgerber

August 2022

Advisor: Michelle Knowles, PhD

Author: Alan Weisgerber
Title: Dynamics and Turnover of Lipid and Protein Domains in Cells and Supported Bilayers
Advisor: Michelle Knowles, PhD
Degree Date: August 2022

Abstract

Protein and lipid clustering is an important mechanism for cell processes such as exo- and endo-cytosis and creating functional signaling complexes. It has been seen that both lipids and proteins are involved with the formation of cluster domains on cell membranes, yet little is known about the interplay between the two. In this work I began with visualizing lipid sorting to artificially induced curvature in supported lipid bilayers, with lipid tails affecting the sorting differently to curvature. These results demonstrate that lipids sort to curvature on curved, supported lipid bilayers. The sorting depends on the number of lipids in the tails with two-tailed lipids accumulating more at regions of curvature. The work then transitions to protein clustering. A plasma membrane SNAP Receptor (SNARE) protein, Syntaxin 1a (Syx1a), is known to cluster and these clusters are sites of membrane fusion in neuroendocrine cells. Syx1a was measured using dynamic measurements (FRAP and single molecule tracking), first by looking at substrate dye interactions to ensure dynamics were not altered by unintended interactions between dye and substrate. Following these studies it was determined that the commonly used poly-L-lysine substrate interacts with commonly used red fluorescent dye (Alexa Fluor 594), as a result Fibronectin is used for further studies. Single molecule dynamics of Syx1a at clusters using a novel system of nanobody interacting with enhanced green fluorescent protein (EGFP) labeled Syx1a reveals not only single molecule dynamics but cluster locations. Studies were performed to see how truncation of Syx1a affects mobility along with cholesterol depletions. Syx1a is more mobile at the center of clusters than elsewhere on the cell surface and that truncation of the Habc domain slightly slows this process. Removal of cholesterol greatly inhibited the motion at the cluster center and generally inhibited mobility thought the membrane. Overall, the work described within elucidates how clusters form on cell and synthetic membranes.

Acknowledgements

I would like to acknowledge the important role my family played in helping me achieve this goal, it would not have been possible without them. I would also like to acknowledge my wonderful lab mates for their help in experiments and data processing. I would like to thank Dr. Todd Wells for feedback on experiments and data processing along with general advice on graduate school. I would like to thank Dr. Michelle Knowles for the opportunities she provided me and the patience she had while I learned.

Table of Contents

List of Figures

Chapter One: Background

1.1 Cell Membrane Organization

The plasma membrane of eukaryotic cells is a complex mixture of lipids and proteins that defines the cell boundary and separates intracellular content from the extracellular environment. At its base level, the membrane is composed of a variety of lipids that are driven to form a structure that is entropically favorable, with polar headgroups facing out and hydrophobic tails facing inwards [1]. This structure forms a lipid bilayer that surrounds the intracellular content and makes up the plasma membrane. The bilayer is a fluid structure, and its leaflets are asymmetric with lipid and protein content unique for each leaflet [1]. Some proteins span the membrane, and are used for cell signaling, and content transfer between the intracellular and extracellular spaces. These proteins range from glycoproteins used for cell recognition to G-protein-coupled receptors (GPCRs) that are used to initiate signaling cascades, ion channels that allow for polarization and depolarization, structural proteins that can induce membrane curvature, and SNARE proteins that span the plasma membrane and allow for membrane fusion with intracellular vesicles [1]. Along with proteins the plasma membrane contains sterols such as cholesterol that enhance its fluidity and help facilitate organization of proteins and lipids in the membrane and can assist in the creation of membrane curvature.

In this dissertation, I focus on the organization of lipid domains as a function of plasma membrane shape (Chapter 3), SNARE proteins on the plasma membrane and how SNARE protein clusters are affected by lipid content (Chapter 4).

1.2 Curvature Facilitated Organization of Lipids

The plasma membrane, while fluid, allows for heterogenous organization of protein, lipid, and sterol content and one way it achieves this is by changing the membrane shape. Although it is not certain whether membrane shape fluctuations serve to recruit molecules that stabilize the transitory curvature or if the accumulation of molecules happens first and this leads to membrane bending. The bilayer is a fluid structure with non-uniform topology of both negative and positive curvature. The presence of curvature facilitates both lipid and protein sorting within the plasma membrane [2]–[5]. Evidence of lipid sorting due to curvature can be seen during fusion pore formation, with changes in liquid ordered phases observed at sites of curvature [4], [6]. The hypothesis behind this sorting is that lipid compositions have specific bending modulus and will preferentially sort to regions of curvature [7]. Lipid tail and head groups have a direct role in curvature sorting abilities with Phosphatidylinositol (PI) and Phosphatidylethanolamine (PE) showing positive (Figure 1.1, brown) and negative curvature (Figure 1.1, purple) preferences, respectively [2], [8]. The physio-chemical characteristics that are responsible for this is that outer leaflets of curvature consist of cylindrical and inverted conical shaped lipids such as lyso lipids and inner leaflets contain conical lipids with highly curved regions rich in unsaturated lipids such as Phosphatidic Acid (PA) [3], [8]. In Chapter 3, sorting of single tailed lipids is characterized on regions of membrane curvature.

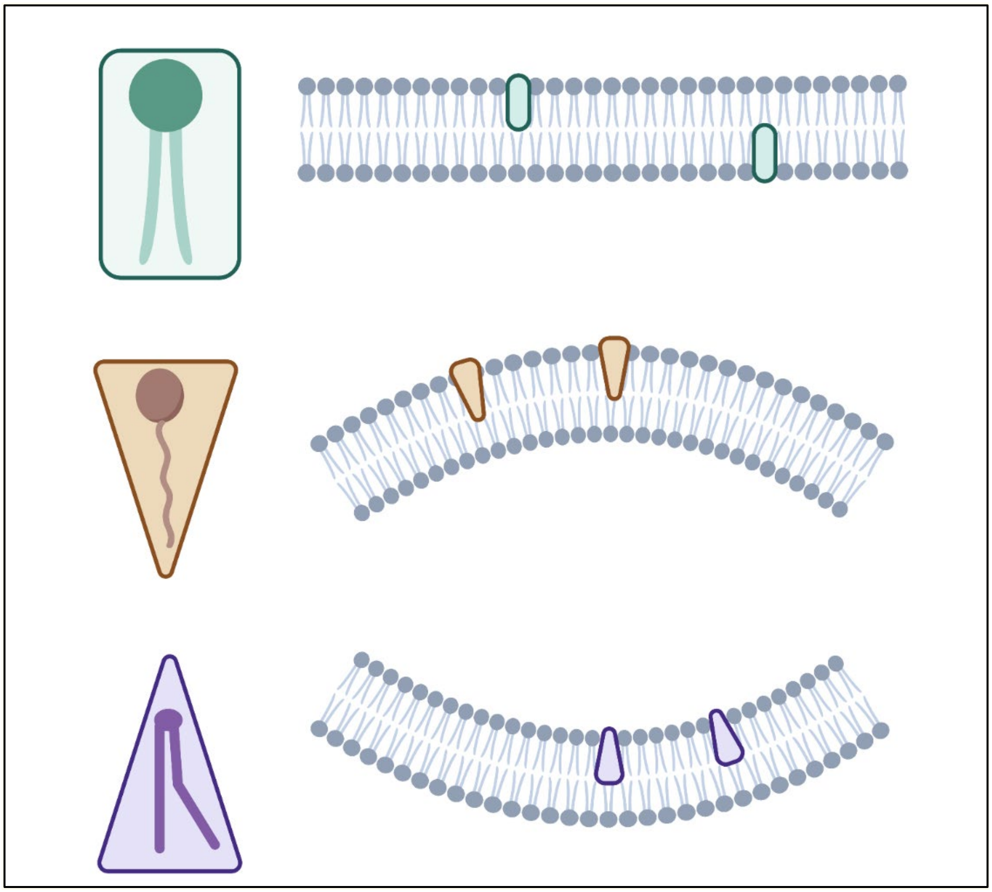

Figure 1.1 Simple cartoon depicting cylindrical lipids with flat surface area (top), inverted cone lipids with positive curvature (middle), and cone lipids with negative curvature (bottom). Cartoon created with Biorender.

1.3 Curvature Facilitated Organization of Proteins

Curvature can also be responsible for protein sorting with proteins such as COPI, Clatherin and Cholera Toxin subunit B (CtB) assembling at regions of curvature and in some cases helping to deform membranes into curved regions [4], [9]. Curvature sensing regions of proteins such as Bin, Amphiphysin, and Rvs (BAR) domains and Amphipathic helices are found in proteins that interact with the plasma membrane and sort to regions of curvature [10], [11]. This mechanism of curvature sensing varies between proteins, with some proteins sensing geometry of the membrane while others detect lipid packing defects with the BAR domains and the Amphipathic Lipid Packing Sensor (ALPS) motifs performing these actions respectively [12].

1.4 Protein-Protein Interaction Facilitated Organization: SNARE proteins

Clustering of proteins in the plasma membrane can also occur through protein-protein interactions. Examples of this can be seen with GPCRs, SNARE proteins, and ion channels, which have been seen to cluster together through homo and hetero protein-protein interactions [13], [14]. GPCR clustering, both homo and hetero forms, results in signal amplification and altered ligand binding as well as G protein coupling and increased signaling efficacy [15], demonstrating that clustering of proteins is one way to regulate their function. Another example of protein clustering is found in SNARE proteins with Syx1a. It has been shown that Syx1a forms clusters, and that these clusters are sites of vesicle docking [16], [17]. SNARE protein clusters are one of the most characterized membrane complexes, however, the molecular level interactions and the role of the lipid environment are not well-understood; this is the focus of Chapter 4. The size of these clusters has been characterized in past works with cluster diameter ranging from 50 to 60 nm, containing 50–75 number of Syx1a molecules [18], and an average cluster density of 19.6 clusters per um^2 [19]. Mobility of these clusters has also been observed before and after stimulation in fixed hippocampal neurons and INS1 cells [18], [20].

SNARE proteins play a vital role in membrane fusion, with Syx1a clustering being an essential step in the fusion process. These Syx1a clusters are thought to recruit partner SNARE proteins to drive membrane fusion. Syx1a along with synaptosomal associated protein 25 (SNAP-25) inhabit the plasma membrane and cooperate with vesicle-associated membrane protein 2 (VAMP-2)/synaptobrevin on the vesicle membrane. Together, these three SNARE proteins provide the necessary energy for membrane fusion through interaction between their hydrophobic coiled-coil domains, causing a transition from trans-SNARE complex, where VAMP2 resides in a different membrane than SNAP25 and Syx1a, to a cis-SNARE complex, where all proteins lie in the plasma membrane [21]. While synaptic vesicle fusion can occur with a minimum of three SNARE complexes, it is common that up to 70 copies of the SNARE complex are involved with cluster formation [22], [23]. Association of multiple SNARE complexes requires many copies of single trans-SNARE proteins, resulting in clustering at future sites of fusion [16].

Syx1a a transmembrane t-SNARE protein, clusters at sites of docking vesicles and provides kinetic energy to perturb the plasma membrane and bring vesicle and plasma membrane into contact. Syx1a, a QSNARE, is a transmembrane protein that consists of 288 residues in length that contains multiple helical domains with its C-terminus end spanning the cell membrane (Figure 1.2). Syx1a contains an Habc{29-146} domain near its N-terminus, which consists of three short helical structures, Ha, Hb, and Hc, which interact with each other. This domain is conserved in other membrane bound Syx1a molecules and likely plays a role in granule docking and interacts with Munc18 [24], [25]. The next distinguishing feature is the alpha helical SNARE-motif{191-295} with Gln226 being a key residue in stabilizing the core SNARE complex when interacting with SNAP-25 and VAMP-2, this motif is also responsible for contributing to the zippering action with the previously mentioned proteins [26], [27]. It is suggested that this motif, which consists of a heptad repeat, is involved in the clustering of Syx1a and plays a role in movement restriction [24], [28], [29]. The last notable feature and the C-terminal end consists of a helical transmembrane domain{266-288}. This region is responsible for anchoring the protein in the plasma membrane. Aside from anchoring in the plasma membrane, the TMD has been shown to form weak homodimers and is a possible contributor to clustering [30]–[32]. Through coarse grain simulations using the TMD of Syx1a, it was shown that clustering occurs in conjunction with cholesterol and GM induced curvature [33].

Figure 1.2 Simple cartoon representation of the transmembrane protein Syx1a. The Habc domain (red) protects the SNARE motif from unwanted interactions and helps to direct the protein to the plasma membrane via interactions with Munc18. The SNARE motif is responsible for interactions with other SNARE proteins and provides the driving force behind fusion. Polybasic region (PB, yellow) interacts with lipid head groups such as PI(4,5)P2. Transmembrane domain (TMD, blue) is embedded in the plasma membrane.

1.5 Lipid Facilitated Clustering

Lipid protein interactions have also been found to play a role in protein clustering, with local lipid content helping to sequester proteins [34], [35]. Lipid rafts, a term used here to define dynamically organized regions of the plasma membrane that contain cholesterol and saturated lipids like sphingolipids and glycosphingolipids, are thought to play a role in transmembrane signaling and clustering of proteins [36]. Proteins such as MAL, tumor necrosis factor α receptors, insulin receptors and G-proteins have been shown to cluster in lipid rafts [36], [37]. Syx1a clusters were also looked at with respect to Detergent Resistant Membranes (DRMs) and were found to be distinct yet also dependent on cholesterol [30]. There is evidence of Syx1a interacting with PI(4,5)P2 lipid rich domains, with the juxtamembrane domain (Figure 1.2, PB region, yellow) of Syx1a, a highly positively charged domain of Syx1a [19], [35]. This co clustering of PI(4,5)P2 along with Syx1a is through to help with recruitment of vesicles to the plasma membrane with synaptotagmin-1 interacting with the PI(4,5)P2 domains [19].

Cholesterol content also plays a role in lipid and protein clustering with cholesterol depletion causing cluster dispersion in membrane sheets [30]. Membrane sheets were created through sonication of PC12 cells to remove the tops of the cells, followed by antibody labeling of Syx [30]. Cholesterol depletion with Methyl Beta Cyclodextrin (MBCD) caused depletion of clusters and dispersion of Syx1a in a uniform manner throughout the membrane [30]. Addition of cholesterol to reconstituted POPC liposomes shows that Alexa647-labeled Syx1a clustered with increasing concentrations of cholesterol [35].

Lipid and protein clustering is essential for cellular function but is difficult to study due to its dynamic nature. In this work we look at both protein and lipid sorting in supported lipid bilayers and in live cells, using common fluorescent microscopy techniques. We find that protein sorting on the cell membrane is influenced by protein domains and cholesterol content, with mobility enhanced or reduced depending on cholesterol content.

Chapter Two: Methodology

2.1 Introduction to Fluorescence

Advancements in fluorescent microscopy have made it desirable tool for studying membranes, membrane bound proteins, and their physiological dynamics, though visualization and measurements. The essence of fluorescent microscopy is that of visualizing and capturing fluorescent molecules and their cumulative intensities and motions. Simplistically, fluorescent microscopy involves selective fluorophore excitation through use of a light source such as a lamp or laser followed by observation and capturing of the resulting longer wavelength fluorescence emission through microscope optics and camera. This information is then digitized by a computer and can be studied and manipulated by various methods [38], [39]. Simple techniques such as two channel imaging allows for the measurement of two probes, with colocalization measurements quantifying overlap and possible interaction of tagged species [40]. FRAP is a technique that simply involves photobleaching the fluorophores in an area of sample and monitoring the recovery through diffusion of the bleached region to study bulk dynamics of molecules [41]. This method is widely used and considered to be one of the best methods for investigation of molecular dynamics in live cells [41]. Fluorescence resonance energy transfer (FRET) is a technique that allows for distance dependent measurement of two species in which energy of donor fluorophore is transferred to an acceptor fluorophore. This technique allows for molecular proximity measurements on the scale of 2-6 nm [42]. Experimental advancements such as FRAP, TIRF, FRET, and recently super resolution microscopy, to name a few, have given investigators the ability to not only measure dynamics and molecular interactions but visualize them. These tools are instrumental in studying and understanding cell membranes, both in how they are organized and the dynamics and interactions that the many components have with each other. Along with techniques and new imaging methods, new designs of organic probes and fluorescent proteins makes fluorescent microscopy an incredible tool for studying a variety of biological structures and processes.

2.2 Fluorescence Recovery After Photobleaching

Fluorescence Recovery After Photobleaching (FRAP) is a technique developed in 1976 Axelrod et al, as a means to study two-dimensional mobility of fluorescent particles that could be applied to cells and biological systems [43], [44]. FRAP is accomplished by using a focused laser to briefly and irreversibly photobleach the fluorophores in a small region of the sample. This region is then observed by the same excitation laser, with recovery occurring by means of lateral mobility of the surrounding unphotobleached fluorophores [43], [44]. This technique can be applied to biological and synthetic specimens with fluorescent proteins or organic fluorophores probing lipids or proteins. The data acquired from FRAP can be fit and used to determine a variety of information about the sample, such as transport process, being that of random diffusion or uniform directed flow, mobility coefficients such as diffusion coefficient or flow velocity, and fraction of probed sample that is mobile [44]. FRAP, a simple, cheap, and easy to perform technique has become one of the most widely used techniques for quantification of dynamics of proteins and organelles in live cells [43].

2.3 Total Internal Reflection Fluorescence

Total internal reflection fluorescence microscopy TIRF is a microscopy technique that allows for selective illumination a sample near the sample sample-coverslip interface. This technique allows for high signal to noise imaging of the cell surface and minimal out of focus fluorescence [45]. The technique is accomplished by exploiting lights behavior when propagating through a high index of refraction medium such as glass then transitioning to a low index of refraction medium such as imaging buffer. This change in index of refraction that the beam of light is subjected to causes the light to have internal reflection based on the refractive indices of the materials it is traversing [46]. The internal reflection of the incident light produces an evanescent wave, by means of an electromagnetic field, that is able to penetrate the sample subtly and excite fluorescent probes [46]. This evanescent wave penetration decays exponentially and only penetrates roughly 100 nm, depending on the wavelength used [45], [46]. This selective illumination of only the sample-glass interface allows for high signal to background and prevents out of focus illumination such as the cytosolic content of the cell [45]. This method of imaging has been used on a variety of subjects ranging from receptors at the plasma membrane, exocytosis, proteins of the endocytic pathway, and cell-substrate contacts [45]. This technique has given researchers who are looking at the cell surface and cell membrane a powerful tool to selectively image physiological events with a high signal to noise.

2.4 Single Particle Tracking

Single Particle Tracking (SPT) is a technique in which individual fluorescent molecules are observed with high spatial and temporal resolution in order to observe dynamic features of the tagged biomolecules [47], [48]. This method has provided insight into numerous biological processes such as gene regulation and ligand-receptor interactions by allowing observation of single-molecules involved in biological events [47], [48]. For SPT to be successful, high signal-to-background fluorescence must be achieved. As a result, the previously described TIRM is desired, along with insightful probe selection allowing for photostability and high quantum yields, and a high sensitivity wide-field detector such as a charge-coupled devices (CCD) camera [47]–[50]. With a correct setup, SPT measurements involve imaging single fluorescent molecules tagged to a target biomolecule and recording their motion as a trajectory [49]. These trajectories reveal insight into events such as diffusion, adsorption, and desorption dynamics [49]. If the sample consists of a low density of fluorescent probes with low background fluorescence, the point spread function (PSF) can be applied to each individual signal allowing for subdiffraction limit localization of molecules, allowing for high resolution localization [49], [50]. These processes give way to data analysis through mean squared displacement (MSD) measurements described by the space explored as a function of time lag [47], [50]. These measurements can be used to calculate the diffusion coefficient through the ensemble average MSDs gathered, allowing the mobility behavior of molecules to be described [47], [50]. SPT allows for direct visualization of molecules of interest with subdiffraction accuracy in a way that can be quantified and characterized.

The methods described above were used to characterize the dynamics and clustering of fluorescently labeled lipids and proteins in the subsequent chapters. Specifically, colocalization and SPT were used to measure the dynamics of lipid sorting on curved bilayers (Chapter 3) and SPT, FRAP, and colocalization measurements were used in (Chapter 4) to measure single molecule interactions at locations of clustered Syx and to detect colocalization with fusion events (Chapter 5).

Chapter 3: Lipid Sorting to Curvature

The plasma membrane is a highly compartmentalized, dynamic material and this organization is essential for a wide variety of cellular processes. Nanoscale domains allow proteins to organize for cell signaling, endo- and exocytosis, and other essential processes. Even in the absence of proteins, lipids have the ability to organize into domains as a result of a variety of chemical and physical interactions. One feature of membranes that affects lipid domain formation is membrane curvature. To directly test the role of curvature in lipid sorting, we measured the accumulation of two similar lipids, 1,2-Dihexadecanoyl-*sn*-glycero-3-phosphoethanolamine (DHPE) and hexadecanoic acid (HDA), using a supported lipid bilayer that was assembled over a nanopatterned surface to obtain regions of membrane curvature. Both lipids studied contain 16 carbon, saturated tails and a head group tag for fluorescence microscopy measurements. The accumulation of lipids at curvatures ranging from 28 nm to 55 nm radii was measured and fluorescein labeled DHPE accumulated more than fluorescein labeled HDA at regions of membrane curvature. We then tested whether single biotinylated DHPE molecules sense curvature using single particle tracking methods. Similar to groups of fluorescein labeled DHPE accumulating at curvature, the dynamics of single molecules of biotinylated DHPE was also affected by membrane curvature and highly confined motion was observed.

This work was done collaboratively with Dr. Philip Cheney and he is a co-first author with myself. Alec Feuerbach acquired data as an undergraduate in the lab. Publication Link: https://www.mdpi.com/2077-0375/7/1/15/htm

3.1 Introduction

Membranes are organized into nanoscale domains of lipids and proteins for optimal physiological function [51]. These domains act to accumulate the protein machinery needed for a variety of essential cellular processes, such as secretion [16], [23], [24] and signaling [52], [53], and the local lipid environment directly affects the function of a variety of ion channels [54], [55]. Like membrane and membrane-associated proteins, lipids also sort within the cell. On the cell surface, domains enriched with sphingolipids and cholesterol are thought to form ordered domains [51]. Within the cell, different membrane compartments contain different lipid compositions, with the trans-Golgi network actively sorting sphingolipids and sterols for delivery to the plasma membrane [56]. Interestingly, exogenously added lipids also sort and the tails of the lipids are a key feature by which they can be organized [57]. Overall, cells are highly heterogeneous in their distribution of proteins and lipids.

To better grasp the mechanisms by which membrane associated molecules are organized in cells, supported lipid bilayers have been used for approximately 30 years as a simple mimic for cellular membranes [58]. Supported lipid bilayers are chemically tunable, fluid, and amenable to fluorescence imaging methods. Even in bilayers containing only simple lipid mixtures, in the absence of proteins, lipid sorting is observed [59]–[62]. A thorough and recent review describes the two mechanisms that can drive lipid sorting in lipid-only systems [63]. These include lipid–lipid phase separation, where lipids organize based on similar tail saturation and the sorted domains are stabilized by cholesterol. In this mechanism, a multi-component mixture of lipids is required and changes in membrane shape can both spontaneously occur and stabilize domains [64]. The second mechanism by which lipid microdomains form requires lipid mixtures that are not globally phase-separated, but rather have micro-emulsions or regions where lipids locally separate. These micro-emulsions can be stabilized in a variety of ways, including the addition of surfactants that ease the line tension at the interface between lipid domains or by local regions of membrane curvature [63]. In both mechanisms, membrane shape plays a role in sorting lipids or stabilizing lipid domains.

Membrane shape has recently been identified as an instigator and stabilizer of lipid domain formation[3], [4], [7], [65]–[68][3], [4], [7], [65], [66], [68], but the mechanism by which lipids sort into curved regions is not clear. Curvature based lipid sorting has been observed in experimental work where curved tubular membranes are created from giant unilamellar vesicles [67], [69] and in curved bilayers [70] for lipid mixtures. In these experiments, curvature aids in phase separation. One model for curvature assisted lipid sorting suggests that lipids are recruited based on their intrinsic molecular shape. However, the coupling between molecular shape and membrane shape is likely very weak [71]. Another way to sort lipids at regions of curvature is by the flexibility of domains. A disordered lipid domain has higher flexibility than an ordered domain and takes less energy to bend. Finally, a third model depends on the formation of defect sites in a lipid bilayer [68], [72]. Hydrophobic curvature packing defects form as a flat bilayer is bent and these defect sites are potential binding locations for defect sensing molecules. In each of these mechanisms it is likely that the addition of protein stabilizes lipid domains formed on regions of membrane curvature [67].

Although accumulation of proteins and lipids at curvature is observed in a variety of experiments [68], [73]–[77], single molecules have demonstrably different behavior [77]. So far, single proteins have not been observed accumulating at curvature, suggesting that a cluster of molecules is needed for accumulation or that the affinity for curvature is quite low and hard to observe in single molecule experiments, where the concentration is inherently low. This is demonstrated in research on the membrane associated protein amphiphysin [78] and the epsin N-terminal homology (ENTH) domain [77]. The curvature association of these proteins depends on the amount bound to the membrane with a higher concentration leading to more accumulation of protein at curvature. However, a variety of membrane associated proteins have been studied, and no experiments address the interactions between single lipid molecules and membrane curvature.

In this work, we measure the dynamics of lipids at regions of membrane curvature and flat regions on a supported lipid bilayer where the curved and flat regions are connected. As opposed to single liposome based methods for measuring proteins at curvature [68], molecules within a bilayer can diffuse from one region of curvature to another. The motivation for designing this curved, lipid surface is to better mimic the cell surface, which is thought to be ruffled. With a biochemical mimic, the shape and chemical composition are separately controlled and lipid accumulation can be directly attributed to the shape in the membrane.

Here, we use a nanoparticle-patterned substrate that supports a lipid bilayer to create spatially isolated and readily identified regions of membrane curvature as described in Figure 3.1. The membrane shape can be adjusted by changing the nanoparticle substrate and the chemical composition of the bilayer is separately tuned. Using fluorescence microscopy methods, we measured the mobility and localization of a common two-tailed lipid, DHPE, with either a biotin-streptavidin or fluorescein molecule attached to the head group. A fluorescein labeled single tailed fatty acid of the same length (16 carbon saturated tail) was also measured (hexadecanoic acid or HDA). Accumulation of lipids at sites of curvature was observed for both fluorescein labeled DHPE (Fl-DHPE) and HDA (Fl-HDA), with Fl-DHPE accumulating ore. Single molecule experiments also show that the dynamics of a molecule depend on whether or not it is located at a region of curvature. Molecules at curvature move, but are highly confined. Molecules on flat regions are very mobile but avoid moving onto regions of curvature. Overall, lipids accumulate at sites of curvature, but single molecules do not accumulate more at curvature or easily transition from curved to flat regions.

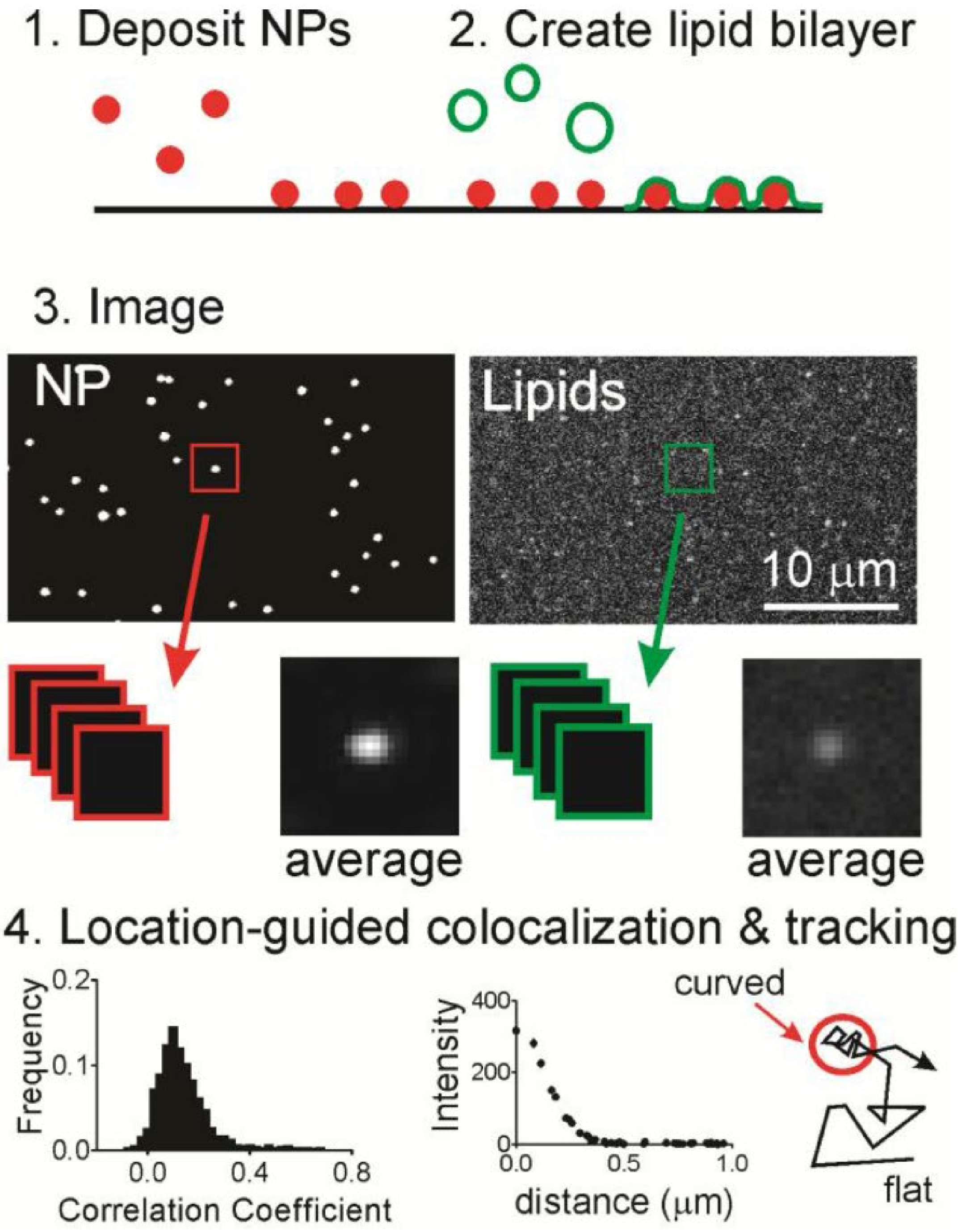

Figure 3.1 The general scheme of the experiment and analysis. (Step **1**) Fluorescent NPs are deposited on a clean glass surface followed by (Step **2**) incubation with liposomes for the preparation of a supported lipid bilayer; (Step **3**) fluorescence microscopy is performed and images of NPs and fluorescently labeled lipids are sequentially obtained at the same location. NP positions are located and both images are cropped at these positions to give pairs of images; and (Step **4**) the Pearson's correlation coefficient is calculated for each pair of images, the average plot of intensity as a distance

from the center pixel (termed a “radial plot”), and single particle tracking is performed on the two-color data (described left to right).

3.2 Materials and Methods

Curved Supported Lipid Bilayer Materials and Preparation

All fluorescent nanoparticles, fluorescently labeled lipids, biotinylated lipids and fluorescently labeled streptavidin were purchased from Life Technologies, Carlsbad, CA, USA. This includes: 5-hexadecanoyl-aminofluorescein (Fl-HDA), N-(Fluorescein-5-thiocarbonyl)-1,2-dihexadecanoylsn-glycero-3-phosphoethanolamine (Fl-DHPE), N-((6-(biotinoyl)amino)hexanoyl)-1,2-dihexadecanoylsn-glycero-3-phosphoethanolamine (biotin-X-DHPE), Streptavidin-Alexa 547 (Strep-546), Marina Blue 1,2-dihexadecanoyl-sn-glycero-3-phosphoethanolamine (MB-DHPE). 1-Palmitoyl-2-oleoyl-sn-glycero-3-phosphocholine (POPC) was purchased from Avanti Lipids, Alabaster, AL, USA. Buffer and glass cleaning reagents were purchased from Sigma Aldrich, St. Louis, MO, USA.

Nanoparticle patterned substrates were created by depositing fluorescent fluospheres on a cleaned glass surface followed by liposome deposition [65]. Specifically, 8-well glass dishes (Lab-Tek Chambered Borosilicate Coverglass System, Thermo Fisher,Waltham, MA, USA) were cleaned by washing in 0.1% sodium dodecyl sulfate (SDS), deionized water and then 1% bleach, followed by storage in deionized water. On the day of bilayer preparation, 8-well dishes were cleaned with 2% Hellmanex, Hellma Analytics, Müllheim, Germany, for one hour, followed by extensive rinsing with buffer. The buffer were used for all experiments was 4-(2-hydroxyethyl)-1-piperazineethanesulfonic acid (HEPES) buffer (30 mM HEPES, 140 mM NaCl, 2 mM CaCl2, pH 7.4).

After cleaning, yellow-green fluorescent (505 nm excitation/515 nm emission, 45 nm diameter) or red fluorescent (580 nm excitation/605 nm emission, 48 or 100 nm diameter) carboxylate modified polystyrene nanoparticles (Thermo Fisher) were deposited on the glass slide. The nanoparticles were then covered with a lipid bilayer using standard liposome deposition techniques [79]. This involves making liposomes by probe sonication of lipid films (0.125 mM lipids in buffer). Liposomes were extruded through a 100 nm filter (Avanti Polar Lipids, Alabaster, AL, USA) and then incubated with the nanopatterned surface for 1 h at 37 °C. The increased temperature was necessary and fluid bilayers were not obtained at room temperature with our deposition conditions. Membrane fluidity was tested with FRAP, using Fl-DHPE or Fl-HDA, or by imaging single molecule motion using total internal reflection fluorescence microscopy. Confocal microscopy was performed to measure colocalization between nanoparticles and lipids.

In confocal imaging measurements, the lipid bilayers contained 98% POPC and either Fl-DHPE (2%) or Fl-HDA (2%). In single molecule imaging measurements, the lipid bilayers contained POPC (97.9%), MB-DHPE (2%) and biotin-X-DHPE (0.1%). The dynamics of Biotin-X-DHPE lipids were detected by in situ labeling with Alexa Fluor 546 (Thermo Fisher) conjugated to streptavidin (Strep-546). The concentration of labeled lipid used was determined by the amount needed for FRAP experiments on MB-DHPE and then kept constant for all samples.

The term “radius of curvature” (ROC) is calculated by the diameter of the NP plus the thickness of a bilayer (5 nm added to each side) and then divided by 2 to obtain the radius. For 100 nm NPs deposited, this corresponds to a ROC of 55 nm; for 45 nm NPs deposited, this corresponds to 28 nm.

Confocal Microscopy

To measure membrane fluidity and colocalization between NPs and labeled lipids, a point-scanning confocal microscope (Olympus Fluoview, Olympus, Center Valley, PA, USA) capable of fluorescence recovery after photobleaching (FRAP) was used. For two color imaging, the red and green fluorescence were taken sequentially with a 100× objective set at 3× zoom such that one pixel was equal to 82 nm. The red channel containing NPs was excited with a 559 nm laser and emission was collected from 575 to 675 nm. The green channel was excited with the 488 nm line of an Argon ion laser and emission was collected from 500 to 545 nm. Images of nanoparticles and labeled lipids were acquired at a rate of 12.5 μs/pixel. When FRAP was performed, a 488 nm laser was used to excite and photobleach fluorescein labeled lipids in a 10.25 μm diameter circular area. FRAP sequences were acquired with a dwell time of 2 μs/pixel and a size of 512 × 512 pixels. All imaging was performed at approximately 23–25 °C.

FRAP sequences were analyzed using ImageJ (version 1.50, National Institutes of Health, Bethesda, MA, USA) and Prism (version 7.0, GraphPad, La Jolla, CA, USA). All frames were adjusted for photobleaching by comparing to a reference area outside the bleached area. The FRAP average intensities were normalized to the highest (usually pre-bleach images) and lowest values (the bleach image) by dividing by the highest intensity and subtracting the lowest. The diffusion coefficient (D) and the mobile fraction was calculated by fitting, as described in the results [80].

Total Internal Reflection Fluorescence (TIRF) Microscopy

Single particle tracking experiments were performed using a TIRF microscope (Nikon, Tokyo, Japan) equipped with a 60× 1.45 NA objective and a 2.5× magnifier for a final resolution of 107 nm/pixel. A 491 nm laser was used to excite the NPs, and a 561 nm laser was used to excite of the Strep-546. Emission was detected on an EMCCD camera (Andor iXon 897+, Andor Technology Ltd., Belfast, UK). The nanoparticles remain stationary and an image was taken by exciting with 491 nm prior to dynamic measurements of the protein tagged lipids at 561 nm. A dual-color, TIRF dichroic was used (Chroma, Bellows Falls, VT, USA) with emission filters (Omega Optical, Brattleboro, VT, USA) at 525/45 nm and 595/60 nm. The dichroic filter passed both the green and red fluorescence and was specifically engineered for TIRF imaging to maintain beam quality. Image series were captured with an exposure time of 30.28 ms and a frame-to-frame interval of 45.6 ms using µManager [81].

Single Molecule Tracking Analysis

Thirty-five movies of lipid bilayers containing labeled SB-DHPE were analyzed in MATLAB (R2016b, MathWorks, Natick, MA, USA) using routines adapted from

Blair and Dufresne [82], which are based on commonly used, particle tracking routines [83]. To analyze the movie data, individual images were filtered and locations identified with sub-pixel resolution. Locations were connected from frame to frame in a way that minimizes the total displacement of particles. Particles that did not move during the entire image sequence were excluded from the analysis. Each track location was compared to the NP positions, which were also found with sub-pixel resolution after band-pass filtering, and marked as colocalized if the lipid particle positions were waiting within 2 pixels of the stationary NPs. From the tracks, the amplitude of the displacement was calculated, as described previously [22]. Diffusion coefficients were then calculated from displacement histograms of colocalized and non-colocalized as described in the results.

Location-Guided Colocalization Image Analysis

Location-guided colocalization methods were used and these methods are visually summarized in Figure 3.1. Two main calculations were performed: a radial plot and Pearson’s correlation function. Both of these analyses begin in the following way: (1) fluorescent NPs, which mark locations of curvature, were identified using spot-finding methods based on freely available code [82]; (2) NP locations were kept if they were further than 9 pixels of another NP or further than 12 pixels from the image edge. The distances were chosen based on the average NP separation and the cropped image size; (3) images were cropped from these location in both the NP and the lipid channel. Afterwards, the distribution of Pearson’s correlation coefficients was calculated for each pair of images, and the average radial plot of the cropped lipid images. This was done by averaging all pixels that are a specific distance from the center pixel. MATLAB code for the radial averaging function is available upon request. The correlation function calculation was obtained from Dr. Justin Taraska [84]. Pearson's correlation coefficient was calculated according to Equation (1):

$$c = \frac{\sum_{=1}^{n} \left(R_i - \langle R \rangle\right)\left(G_i - \langle G \rangle\right)}{\sqrt{\sum_{i=1}^{n} \left(R_i - \langle R \rangle\right)}\sqrt{\sum_{i=1}^{n} \left(G_i - \langle G \rangle\right)}} \tag{3.1}$$

where R is the red cropped image, G is the green cropped image and Ri is the intensity of the R image at pixel number i. The function sums over all pixels (n) in an image.

Melittin-Based Quenching Assay

Supported lipid bilayers were formed as described above with POPC:NBD-DHPE (2-(4-nitro-2,1,3-benzoxadiazol-7-yl)aminoethyl-DHPE (Avanti Polar Lipids, Alabaster, AL, USA)) at a 98:2 molar ratio on a nanoparticle patterned substrate containing red fluorescent 100 nm fluospheres (Thermo Fisher). TIRF images of the NBD fluorescence were measured in time at 10 Hz and sodium dithionite (5 mM in HEPES buffer) was added to quench the NBD dye after 30 s of imaging. The focus slightly drifts upon the addition but was refocused. At 117 s pore forming protein, melittin (Sigma Aldrich, St. Louis, MO, USA) was added for a final concentration of 1.76 µM. The average image intensity was measured for each time point and normalized by dividing by the first image intensity value.

GraphPad Prism and Microsoft Excel (version 2013, Redmond, WA, USA) were used for all other plots and data fitting and significance testing.

3.3 Results

To determine whether lipids accumulate at curvature, we used a supported lipid bilayer that contained localized regions of membrane curvature (Figure 3.1). Fluorescent nanoparticles (NPs) were deposited onto a cleaned glass surface (Figure 3.1, Step 1) and then liposomes containing fluorescently labeled or biotinylated lipids were incubated in the solution above at 37 °C for one hour (Figure 3.1, Step 2), during which time the liposomes fused with the surface to form an extended bilayer [35]. One key feature of this system is the lack of lipid–lipid phase separation. The bilayer contains 99% palmitoyl-2-oleoyl-sn-glycero-3-phosphocholine (POPC) and 1% Fl-DHPE or Fl-HDA. Note that all lipid chemical structures are shown in Figure 3.2. The only unique features capable of causing lipid sorting are the curved regions. After incubation and the removal of any unfused liposomes, fluorescence microscopy was performed to determine if labeled lipids co-localize with regions of curvature (Figure 3.1, Step 3).

To determine if labeled lipids accumulated at curved regions, the two-color images were cropped around every nanoparticle position and then analyzed in two ways (Figure 3.1, Step 4). First, the Pearson’s correlation coefficient was calculated to determine the extent of similarity in pairs of cropped images. A perfect match would have a coefficient of 1.0 and the inverse of an image would have a coefficient of −1.0. A score of 0 means there is no correlation. The second, quantitative measurement calculated from the cropped lipid images is the radial plot. This is a measurement of the intensity as a function of the distance from the center, where the region of curvature is located. From a series of images of single molecule dynamics, DHPE molecules were tracked relative to NP positions in time.

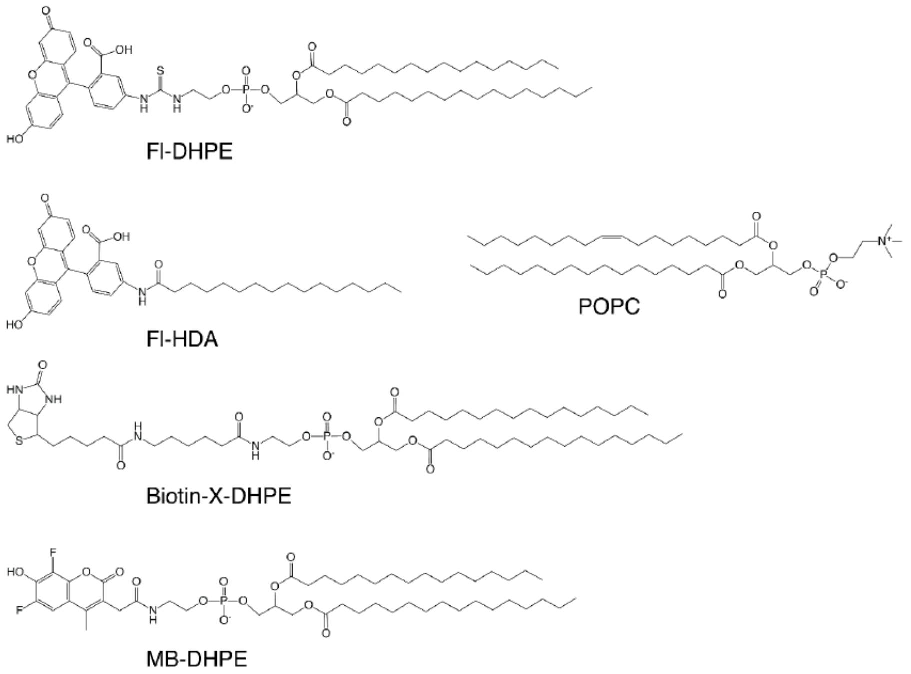

Figure 3.2 Chemical structures of the lipids used in this study. Fluorescein labeled DHPE (Fl-DHPE, Thermo Fisher Cat. Num. F362), Fluorescein labeled Hexadecanoic Acid (Fl-HDA, Thermo Fisher Cat. Num. H110), Biotin labeled DHPE (Biotin-X-DHPE, Thermo Fisher Cat. Num. B1616), Marina Blue® labeled DHPE (MB-DHPE, Thermo Fisher Cat. Num. M12652) and POPC (Avanti Polar Lipids Cat. Num. 850457).

Bilayer Characterization

To characterize the curved, supported lipid bilayer, lipid fluidity and the presence of a bilayer were measured. To measure fluidity, fluorescence recovery after photobleaching (FRAP) traces was measured for each sample. The average and standard deviation are plotted in (Figure 3.3a) for a radius of curvature (ROC) of 28 nm and in (Figure 3.3b) for an ROC of 55 nm. Bilayers are fluid when NPs are present and Fl-HDA and Fl-DHPE recover equally well.

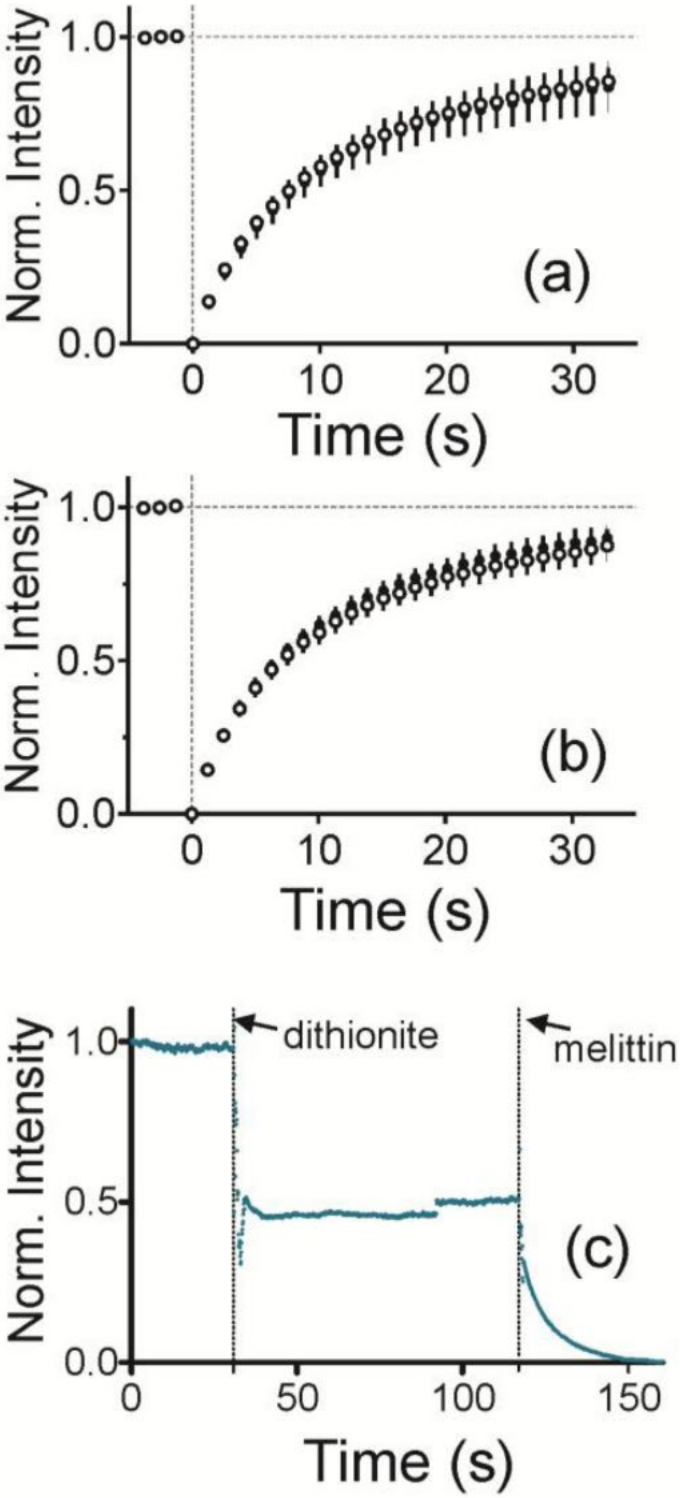

Figure 3.3 FRAP recovery for a 10 µm diameter region photobleached at time 0 s. (**a**) Fl-HDA (white circles) and Fl-DHPE (black circles) on samples that contain 28 nm ROC; (**b**) Fl-HDA (white circles) and Fl-DHPE (black circles) on samples that contain 55

nm ROC. Error bars are standard deviation; (**c**) NBD-DHPE fluorescence is quenched by dithionite. Once melittin, a pore forming protein, is added, fluorescence decreases to background levels.

To obtain quantitative information about the dynamics of lipids, the fluorescence recovery traces were fitted according to previously established protocols as shown in Equations (3.2) and (3.3) [43]. Fluorescence recovery data, Y (τ), was fit with a single exponential with the following equation:

$$Y(\tau) = Y_0 + (Y_{\text{infinity}} - Y_0)(1 - \exp(-k\tau)) \tag{3.2}$$

where Y is the intensity within the bleached region at times, τ, 0, and ∞. To obtain diffusion coefficients, the time to recover to half the intensity is calculated according to: $\tau_{1/2} = \ln(k/2)$. From this, the diffusion coefficient is:

$$D = (r^2/4\tau_{1/2})\gamma_D$$

(3.3)

where $\gamma_D = 0.88$ for a circular bleached area and r is the radius of the bleached spot. The fitting results are summarized in Table 3.1. Overall, there are no significant differences in any of the curves. This is partly due to having relatively few NPs in the bleach area; the NP density in these experiments is <0.01 NP/μm^2. Most of the dynamics measured in the FRAP assay relate to the fluidity of the lipids on the flat, glass surface.

Table 3.1 Diffusion coefficients and fraction mobile measured from FRAP recovery curves.

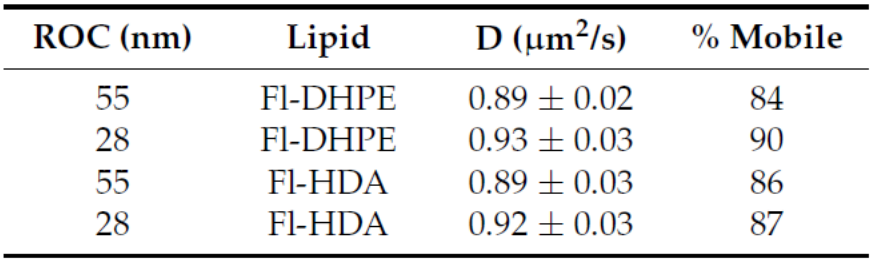

ROC (nm)	Lipid	D ($\mu m^2/s$)	% Mobile
55	Fl-DHPE	0.89 ± 0.02	84
28	Fl-DHPE	0.93 ± 0.03	90
55	Fl-HDA	0.89 ± 0.03	86
28	Fl-HDA	0.92 ± 0.03	87

To determine if the bilayer is two layers and impermeable, NBD labeled lipids were incorporated into both sides of the bilayer and then quenched with sodium dithionite (Figure 3.3c). As dithionite is not able to pass through an intact lipid bilayer, this reaction is used to demonstrate access to a leaflet of the bilayer [37]. This is observed by a drop in fluorescence upon addition of dithionite at 30 s. Fluorescence levels were off by up to approximately 48% of the initial fluorescence. Once melittin, a pore forming protein, is added, dithionite gains access to the leaflet closest to the solid support. This reduces the fluorescence to the background level.

Lipid Accumulation at Membrane Curvature

The accumulation of lipids at regions of membrane curvature was measured by quantifying the intensity of lipids at NP regions. The average images of Fl-DHPE and Fl-HDA cropped around NP locations are shown in Figure 3.4a. Here, the background has been subtracted and all images are scaled linearly and identically for direct, visual comparison. Fl-DHPE collected at a radius of curvature (ROC) of 55 nm in the highest amount and Fl-HDA collected in the least amount at an ROC of 28 nm. The projection of the membrane shape likely accounts for most of the differences between different curvatures, but the shape is consistent from one lipid to another, making the different lipids directly comparable. To quantify the intensity, a radial plot was calculated from each cropped image and the average radial plot is shown for DHPE and HDA at an ROC of 55 nm (Figure 3.4b) and for an ROC of 28 nm (Figure 3.4c). For both sizes, Fl-DHPE accumulated more at curvature than Fl-HDA.

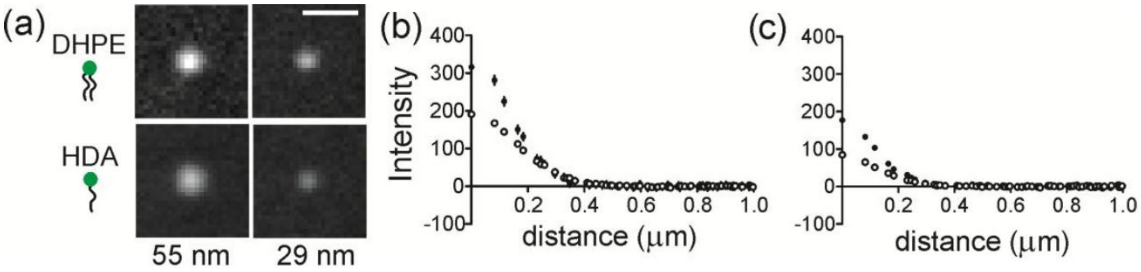

Figure 3.4 Location-guided colocalization measurements of fluorescent lipids at regions of membrane curvature. (**a**) cropped and averaged images for each size and lipid measured. All images have background subtracted and are scaled identically. Scale bar = 1.0 μm; (**b**) a radial plot of Fl-DHPE (black circles) and Fl-HDA (white circles) at regions with 55 nm radius of curvature; (**c**) a radial plot of Fl-DHPE (black circles) and Fl-HDA (white circles) at regions with 28 nm radius of curvature. The error bars represent the standard error of the mean (SEM).

The radial plot is a direct measure of the amount of labeled lipid present, but a second measurement of colocalization was calculated from pairs of images. Here, the Pearson's correlation coefficient was measured for each lipid–NP image pair and averaged. The full distribution is shown in Figure 3.5 and the average is shown in Figure 3.6. This suggests that lipids accumulate at curvature for all lipids and shapes measured, and the trend is similar to that observed in Figure 3.4 with DHPE colocalizing the most and HDA the least. Although the Pearson's correlation coefficients are quite small, DHPE is significantly higher than HDA, indicating that the lipids are weakly associated with curvature, but DHPE associates more. It is interesting to note that in our bilayer system, the bilayer composition is symmetric and higher degrees of sorting have been observed when we added lipids specifically to the upper leaflet only [65].

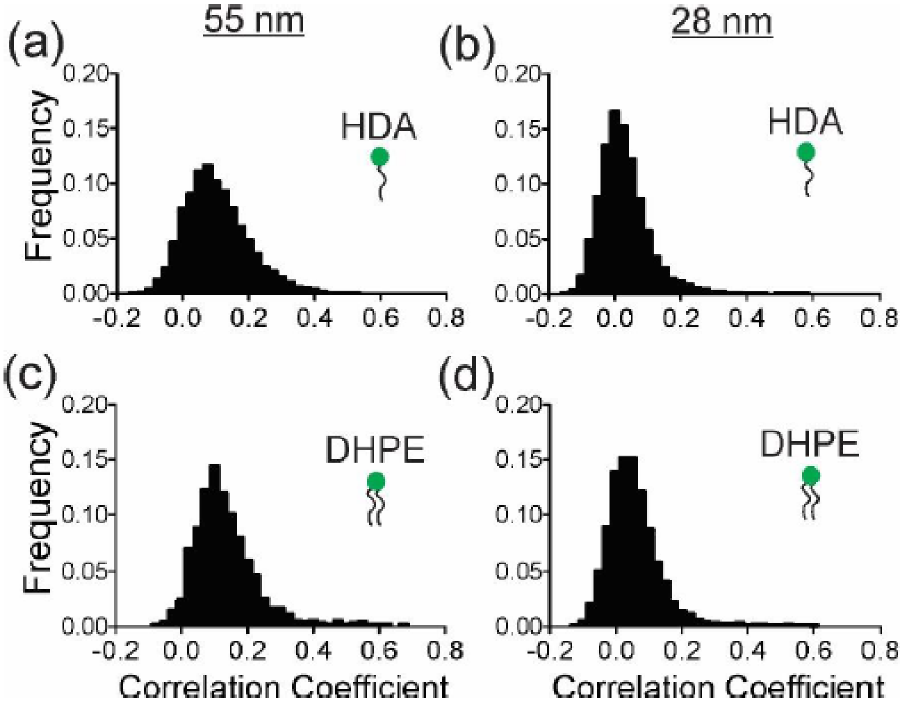

Figure 3.5 Distributions of the Pearson's correlation coefficient for HDA and DHPE at regions of membrane curvature. A) Fl-HDA at regions of curvature that have a ROC pf 55 nm. B) Fl-HDA at regions of curvature that have a ROC pf 28 nm. C) Fl-DHPE at regions of curvature that have a ROC pf 55 nm. D) Fl-DHPE at regions of curvature that have a ROC pf 28 nm.

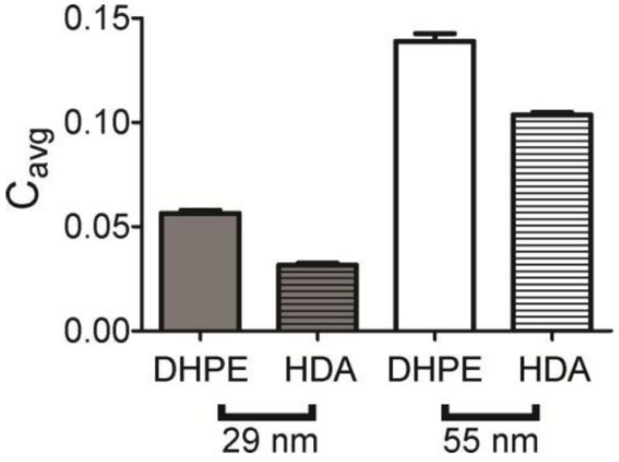

Figure 3.6 Pearson's correlation coefficient was calculated for NP: lipid pairs of images that were cropped from the same sample region. DHPE (solid bars) accumulates more than HDA (striped bars).

Single Molecule Lipid Dynamics

To address the dynamics of lipids specifically at regions of membrane curvature, we used single molecule imaging and tracking methods. The highest colocalizing lipid (Fl-DHPE) was chosen and is also commercially available with a biotin linkage in place of the fluorescein. However, since the imaging modality for single molecules is total internal reflection fluorescence (TIRF) microscopy, we only measured lipid bilayers containing small (ROC = 28 nm) features to stay within the excitation range (~100 nm depth) of the TIRF field. To prepare samples for single molecule imaging, Biotin-XDHPE (SB-DHPE) (0.1%) was incorporated into curved bilayers containing POPC and then tagged in situ with fluorescently labeled streptavidin (Strep-546). Figure 3.7a shows example trajectories that were observed at flat and curved regions of membrane, where the black dots are the NPs and the blue lines are the tracks of a single lipid. At first glance, molecules at curvature are more confined. To quantify the dynamics of trajectories, we calculated the amplitude of the displacements made for single lipids at regions of curvature and compared that to the displacements of single lipids on flat regions (Figure 3.7b,c). For a track to be considered to be at curvature, the position of the lipid must be within two pixels (214 nm) of the position of an NP and colocalization with curvature is, therefore, time dependent. Parts of a track can be colocalized, whereas other parts can be on flat regions. The steps of the track that start at curvature are counted as colocalized. Tracks are significantly more confined when at curvature, exhibiting more than a three-fold reduction in step amplitude relative to tracks on flat regions (Figure 3.7b).

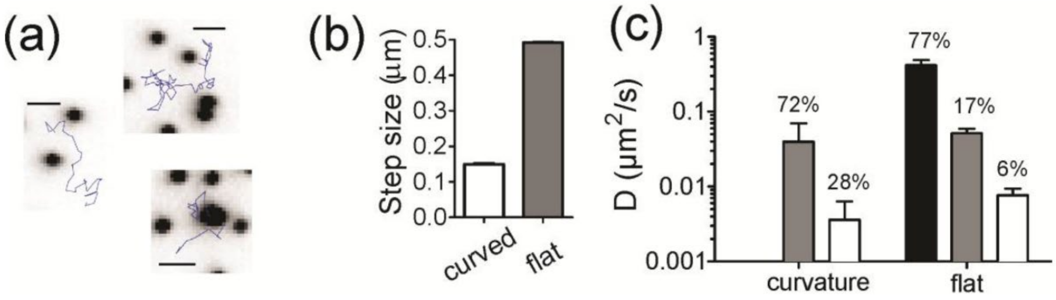

Figure 3.7 Single Biotin-X-DHPE molecules tagged with Streptavidin-Alexa546 were tracked on the curved supported lipid bilayers (ROC = 28 nm) in space and time. (**a**) example trajectories (blue) show the heterogeneous dynamics observed on both flat (white) and curved (black) regions. Scale bar = 1 µm; (**b**) the average step a molecule takes over 0.228 s (5 frames) when starting at a region of curvature (white) or at a flat region (grey); (**c**) the distribution of steps observed at curved and flat regions (shown in Figure 3.8) was fitted to Equation 3 to obtain the diffusion coefficients and the percentage of steps moving at that rate. The average D is plotted for $t = 0.091$, 0.228 and 0.456. Note that there is no fast component for the tracks that start at regions of curvature.

The distribution of step sizes (Figure 3.8) was fitted with the following equation to determine what fraction of the molecules were moving at certain speeds [85]

$$Y\,(r,t) = r\left[A_1\, exp\left(-\frac{r^2}{4D_1 t}\right) + A_2\, exp\left(-\frac{r^2}{4D_2 t}\right) + \; A_3\, exp\left(-\frac{r^2}{4D_3 t}\right)\right]$$

(3.4)

Three modes of motion were used to fit the dynamics of tracks on the flat regions of the surface, similar to what has been done previously [86]. The three modes of motion are: immobile (Figure 3.7c, white), slow (Figure 3.7c, grey) and fast (Figure 3.7c, black) The dynamics of lipid molecules on the regions of curvature, however, fit well with only two parameters (immobile and slow); the high speed motion observed on flat regions was not present in tracks that started at a curved regions. The diffusion coefficients from the fit results are summarized in Figure 3.7c and the contribution of each rate of diffusion is written as a percentage above the bars. Overall, the motion of lipids at regions of curvature is confined.

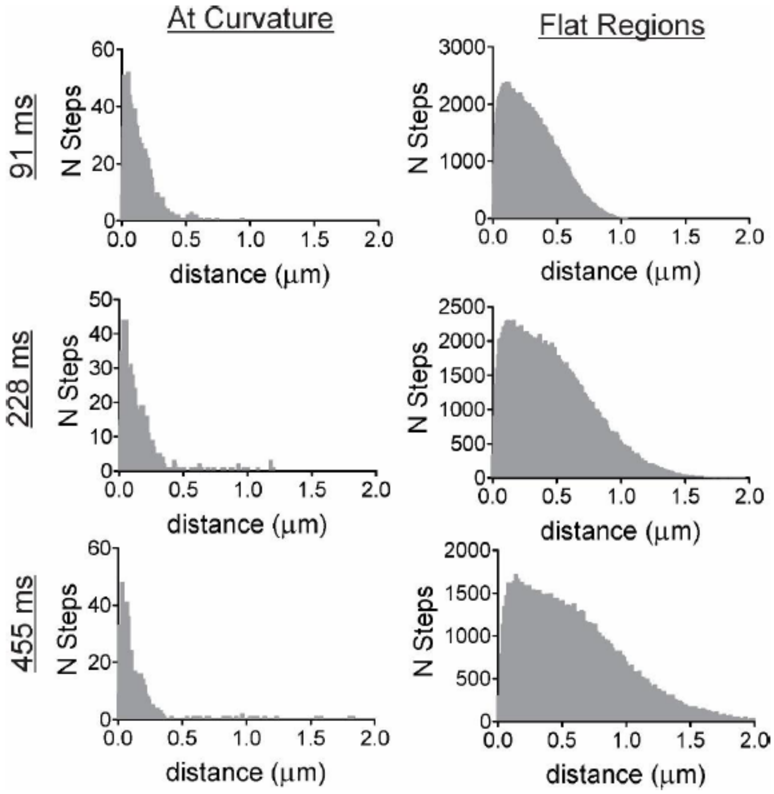

Figure 3.8 Distributions of the displacements made by single Strep-DHPE molecules. Tracks were separated into steps that start at curved regions (left) and flat regions (right) for 91, 228 and 455 ms time delays.

3.4 Discussion

One purpose of this work was to examine how different lipids sort as a function of membrane shape. Two lipids were tested; Fl-DHPE has two 16 carbon-long, saturated tails and Fl-HDA has one 16 carbon long, saturated tail. For both radii of membrane curvature measured (28 nm and 55 nm), Fl-HDA accumulates less to curved regions, but all lipids show some accumulation (Figures 3.4 and 3.6). Three models were put forth regarding the mechanism of lipid sorting at curvature. The first mechanism relies on the intrinsic shape of molecules. Cylindrically shaped lipid molecules, where the head and the tail of the lipids are approximately equal in occupied volume, prefer flat regions. DHPE and POPC are considered to be cylindrical lipids. Inverse conical shaped molecules, where the lipid head group takes up more volume than the lipid tails, prefer to sort into positively shaped curvature [87]. Single tailed lipids, like lysoPC and Fl-HDA, are inverse conical in shape. Although the coupling between membrane shape and molecular shape is weak [71], we would expect that Fl-HDA would accumulate more at curvature that Fl-DHPE and this was not observed (Figures 3.4 and 3.6).

The second mechanism of lipid sorting at curvature depends on phase separation, where the flexible, disordered lipid domains could be bent over the nanoparticles more easily than ordered lipid domains. In our system, lipid phase separation is not likely to occur as POPC makes up over 97% of the lipid composition.

The third mechanism of lipid sorting at regions of curvature involves a defect site model. In this model, defect sites in the membrane form as it curves, creating locations within the lipid bilayer where hydrophobic tails are more exposed to the external buffer [68], [72]. The number of defect sites increases with higher curvatures (smaller ROC) and these serve as binding locations for other molecules with exposed hydrophobic portions, such as palmitoylated proteins, lipids, or amphipathic helices [68]. The amount bound to curvature depends on two factors: the number of binding sites and the affinity of the molecule for a defect site. Since the number of binding sites is unlikely to be different when comparing Fl-HDA and Fl-DHPE on the same membrane shape, affinity for defect sites likely plays a role, with Fl-DHPE having higher affinity for defect sites than Fl-

HDA. Our results agree with past work comparing Fl-DHPE and Fl-HDA on single liposomes [68], suggesting that the support beneath the bilayer is not playing a role in sorting. In liposome based work, Fl-DHPE accumulated more on smaller liposomes and a trend was observed between the number of carbons in the tails and the amount that accumulates, with longer or multiple lipid tails accumulating more. Finally, the head group could play a larger role in lipid sorting than we have previously acknowledged. The differences between the HDA linkage and DHPE linkage to fluorescein are not identical (structures can be found in Figure 3.2). However, the role of the head group in sorting was measured previously and showed little effect on curvature sensing [68].

Even though sorting occurs with DHPE lipids, single molecule trajectories do not show preference to accumulate at curvature. Approximately 1.2% of the tracks observed resided within two pixels of an NP location. With an average of 404 NPs, each creating a 214 nm radius circle of area considered to be colocalized within 3000 μm^2 area for the movies analyzed, approximately 7.8% of the surface contains regions of colocalization. This suggests that molecules avoid curvature. It is also difficult to find trajectories that transition from flat to curved regions, yet FRAP data has shown that lipids' NP positions recover [65] and the single molecule tracking of SB-DHPE clearly demonstrates that movement of molecules at sites of curvature is very confined (Figure 3.7).

The lack of single molecule tracks favoring sites of curvature and colocalizing with nanoparticles is in agreement with the work of others, where ENTH proteins sorted to positive curvature on a wavy supported lipid bilayer, but when single proteins were tracked, no preference was observed [77]. Two alternative reasons why the fraction of single molecule tracks that colocalize to curvature is so low could be due to: (1) the resolution of the microscope. If two molecules were contained within the same region of membrane curvature, they would be counted as one track; (2) particles that did not move during the entire image sequence were excluded from the analysis and this may also lower the percent of lipids that were considered to be colocalized. Future experiments using photo-activatable probes or other methods of analysis could elucidate this further.

Even though the number of tracks that colocalized with curvature was lower than expected, single lipid molecules that resided at curved regions were affected by the membrane shape (Figure 3.7). The dynamics were confined, but molecules at sites of curvature likely escape to exchange over the course of minutes as we observed previously with FRAP measurements [65]. The rates of diffusion measured here for single lipids are slower than what has been measured previously by others [86]. For example, single molecule tracking experiments of a PIP2 binding protein domain measured a fast diffusion coefficient of 1.4 $\mu m^2/s$ on flat, supported bilayers when two lipid molecules were bound. This is approximately 2.5 times faster than our observations for SB-DHPE. One major difference in our experiments is the use of POPC instead of DOPC. POPC has a higher melting transition temperature (−2 °C) compared to DOPC (−17 °C) and is more viscous [88]. A second reason could be due to the fact that streptavidin acts as a cross-linker to lipids and has four biotin binding sites. However, only two are likely available on one side of the protein. If more lipids bind, movement would also be slower.

3.5 Conclusion

In conclusion, this work demonstrates a simple system for created curved lipid bilayer using a nanoparticle patterned surface. At regions of curvature, two-tailed

(DHPE) and one-tailed (HDA) molecules accumulate at curvature, with two tailed molecules accumulating more. When single molecules are tracked, DHPE molecules do not favor sites of curvature. Instead, the curvature acts to contain molecules within the curved region and exclude those on the flat regions, creating a local, nanoscale confinement zone for lipids.

Chapter 4: Tracking of Syx1a with Respect to Clustering and the role Substrate Selection

The clustering of proteins is essential for many cellular processes. In any experiment, the labeling and measurement of the process needs to not interfere with the process itself. Therefore, the dye labeling of transmembrane proteins for the study of clustering dynamics requires correct selection of the substrate and tracking dye. The beginning of this chapter focuses on how to make this selection and what worked best for studying Syx1a clustering dynamics [89]. The dynamics of a protein can be dramatically affected if the label interacts non-specifically with the substrate or with other molecules in the system. We first performed FRAP experiments to determine that substrate dye compatibility was desirable and that dynamics were unhindered by label-substrate interactions. In the second half of this chapter, single molecule tracking was performed to determine the dynamics of Syx1a clustering with full length, truncated, and with cholesterol depletion to see how dynamics and clustering were affected. We found that Syx1a is mobile on the plasma membrane but less mobile near the edges of clusters and this depends on the presence of the N-terminal, Habc, domain and cholesterol, both of which are needed for exocytosis. The depletion of cholesterol dramatically reduces the mobility of Syx1a within clusters and less so over the rest of the plasma membrane. This suggests that fluidity of Syx1a supramolecular clusters is needed for function.

A portion of this work has been published here ([89] https://doi.org/10.1016/j.bbadva.2021.100026). In these sections I am the first author and collected and analyzed data. The remainder of this chapter will be submitted for publication. In this work, I collected and analyzed data, assisted with writing the manuscript. Zdenek Otruba will be the second author. He is an undergraduate in the lab and performed the simulation and modeling of the numbers.

4.1 Membrane dynamics are slowed for Alexa594-labeled membrane proteins due to substrate interactions

The addition of fluorescent dyes to proteins, lipids and other biological molecules can affect a range of processes such as mobility, molecular interactions, localization, and, ultimately, function. The dynamics of a protein can be dramatically affected if the label interacts non-specifically with the substrate or with other molecules in the system. To test how dye-substrate interactions affect protein diffusion, fluorescence recovery after photobleaching (FRAP) measurements were designed to explicitly determine the role of the dye on the diffusion of a transmembrane protein, Syntaxin1a, expressed on the cell surface. Syntaxin1a, was tagged with EGFP on the extracellular side and an EGFP nanobody with or without a dye label was attached. FRAP was performed on Syx1a-EGFP and the choice of cell growth substrate affected mobility in the presence of a dye labeled nanobody. This work provides evidence for choosing fibronectin (Fn) over poly-L-lysine (PLL) in FRAP and single molecule tracking measurements when using Alexa594, a common probe for red fluorescent measurements. Alexa594-labeled nanobody but not unlabeled nanobody, dramatically reduced the mobility of Syx1a-EGFP when cells were cultured on PLL. However, when Fn was used, the mobility returned. Mobility measured by single molecule tracking measurements align with the FRAP measurements with Fn coated surfaces being more mobile than PLL.

4.1.1 Introduction

Recent advancements in imaging methods that probe protein mobility rely on the use of organic fluorescent dyes [90], [91], which are notably brighter and more photostable for imaging measurements. Therefore, organic dyes are widely used in single molecule tracking, super-resolution and fluorescence recovery after photobleaching (FRAP) experiments to study the localization, mobility and dynamics of proteins [91]–[93]. Fluorescent labels for cellular imaging are ideally designed when there is minimal interaction with the system; probes should be unbiased reporters for the location of a protein of interest. Therefore, probes need to avoid: 1) membrane insertion, 2) multimerization/aggregation, and 3) non-specific, substrate binding. These types of interactions will affect the measurement of membrane protein dynamics, typically leading to a reduction in the mobility of the protein studied.

There is clear evidence that commonly used dyes have unintended interactions with membranes, causing mobility to be hindered due to non-physiological artifacts. For example, lipid mixing kinetics are affected by the probe choice in viral fusion assays, with the dye R18 mixing at a lower efficiency than TexasRed [94]. Dyes interact and insert into membranes depending on the dye and membrane physico-chemical characteristics. In a large scale screen of 32 dyes for dye-membrane interactions, it was determined that that highly charged dyes have lower membrane interaction factors when compared to uncharged or singly charged dyes and, typically, larger dyes (red dyes) interact more with membranes [95]. In all-atom molecular dynamics simulations of dyes (Cy3, Cy5) with membranes the insertion of dyes into the membrane was initiated by a charge interaction between the lipid headgroup and the dye, followed by a slower insertion of the hydrophobic portion of the dye into the membrane [92]. To alleviate issues, dyes often contain charges to minimize non-specific interactions with cell membranes.

Multimerization has been an issue for a variety of probes, such as organic dyes attached to antibodies and fluorescent proteins [96], [97]. Multimerization can lead altered dynamics as membrane proteins have a larger drag through the membrane [86]. To combat this, dye labeled nanobodies, which are monovalent, single domain antibodies, have been a valid strategy for reducing the effects of multivalent binding observed with traditional antibodies [98]. The popularity of nanobodies as labeling entities for membrane proteins has grown over the past 10 years, with the design of nanobodies that recognize specific protein conformations [99] and ones that bind specifically to GFP [100]. In this work, a nanobody that binds EGFP on the surface of cells was purified, dye-labeled, and added to cells in culture prior to imaging.

A third interaction known to affect protein dynamics is that of the dye with the cell growth substrate. Recent work shows that different organic dyes adhere differentially to a variety of surface coatings [101], [102] and this interaction is likely due to the hydrophobicity of the dye, with hydrophilic dyes resulting in fewer non-specific bindings compared to hydrophobic dyes, which were correlated to lower mobility and higher instances of non-specific binding [101]. To assess cell growth substrate binding, immobility of a variety of dye-affibody conjugations with different targets were measured. The conclusion was that there were many factors to dye interactions were challenging to predict accurately, since substrate, dye selected, and protein of interest all play crucial roles [101]. As a result, all three materials should be tested and specifically chosen for the experiment.

Cell growth substrates vary widely in their overall charge, method of cell attachment and their ability to adhere to glass surfaces used in microscopy. In this work, poly-L-lysine (PLL) and fibronectin (Fn) were used. PLL is a polypeptide consisting of lysine amino acids, making PLL a positively charged substrate. Cells attach via nonspecific electrostatic interactions with the negatively charged cell membrane [103]. Fn is a glycoprotein that interacts with integrin receptors to facilitate cell attachment and spreading [103]–[105]. Fn is negatively charged (pI 5.5–6.0) and has a hydrophobic binding domain for cell attachment. Many dyes carry a negative charge to prevent insertion and interactions with cell membranes, potentially leading to non-specific binding to cell substrates [101], [102]. In this work, Alexa594 was used and contains an overall -2 charge.

Elucidating probe interactions with the cell growth substrate is challenging to determine because comparison to a probe-free measurement cannot typically be made; a fluorescent marker must be used for imaging. In this work, we overcome this and describe a FRAP-based assay that can specifically measure how dyes affect mobility. In this assay, the mobility of an externally exposed EGFP attached to a transmembrane protein on the cell surface (Syntaxin1a-EGFP) was measured. The effects of a nanobody to EGFP, with and without a dye label, on membrane protein dynamics was determined.

This differential type of measurement directly probes how the dye alters the dynamics. Several surface treatments were compared for their ability to non-specifically bind dyes. Alexa594-labeled nanobody but not unlabeled nanobody, dramatically reduced the mobility of Syx1a-EGFP. The dye's ability to affect mobility was identified to be due to an interaction with a commonly used substrate for cell adhesion, PLL. However, when Fn was used, the mobility returned. Single molecule tracking measurements align with the FRAP measurements with Fn coated surfaces being more mobile than PLL. Overall, we observed dye and surface coating dependent interactions that affected membrane protein dynamics and were able to alleviate this by using Fn.

4.1.2 Materials and Methods

All buffer reagents were purchased from Sigma Aldrich except when noted.

Substrate Coating: Coverglass (Ted Pella, 25mm round, #1.5 thickness) was coated with poly-L-lysine ("PLL", Sigma Aldrich, P4707) and/or fibronectin ("Fn", Gibco, 33016015). For PLL coating, glass was cleaned by soaking overnight in 0.1% bleach solution, followed by rinsing thoroughly in DI water. PLL was added to the coverglass and incubated at room temperature for 15 minutes then rinsed three times with DPBS containing Ca^{2+} and Mg^{2+}(Gibco). For Fn coated glass, several approaches were taken. A 3M solution of potassium hydroxide was used to etch glass following the methods described previously [106]. Coverglass was also taken straight from the package, dipped in ethanol and flamed for approximately 5 seconds, then coated with Fn. Results from both methods were similar, but flame treating is simpler to do. Fn was also coated to PLL coated coverslips, where PLL was applied as described above then Fn was incubated for 15 minutes or overnight. The concentration of Fn ranged from 2 µg/ml to 50 µg/ml and noted in the figure captions.

Cell Culture: PC12-GR5 cells were grown as described previously[19]. Briefly, cells were maintained on T25 flasks (Life Science Products, Frederick, Colorado) in 10% CO_2 and 37°C. Cells were passaged up to 40 times before thawing a new batch of cells. Transfection was performed with Lipofectamine 3000 (Thermo Fisher Scientific) according to manufacturer protocols but the amount DNA and Lipofectamine was reduced by half the recommendation to minimize cell damage. At 20-40 hours post-transfection cells were imaged in Imaging Buffer (140mM NaCl, 3mM KCl, 1mM $MgCl_2$, 3mM $CaCl_2$, 10mM D-Glucose, 10mM HEPES, pH 7.4). DNA plasmids Syx1a-EGFP-dCMV and Syx1a-EGFP were supplied from Wolfhard Almers [16], [22]. The dCMV promoter is a truncated promoter that dramatically reduces expression to be equivalent to the endogenous amount [16], [22]. This construct has been deposited at Addgene (#34631).

Nanobody Purification: BL21 cells were transformed with DNA expressing an anti-EGFP nanobody (Addgene, #49172) at 37°C in a 10 mL overnight starter culture with 2000x ampicillin 100 mg/mL. Starter cultures were then used to inoculate 1 L of Luria Broth (Alpha BioSciences, Baltimore, MD, L12-112) and grown until OD600 of 0.9 after which induction started with 1 mL 1M IPTG (GoldBio, St. Louis, MO) and temperature was changed from 37°C to 20°C. Cells were allowed to express for 24 hours after which they were spun down at 6000x*g* for 15 min at 4°C. Cells were then frozen at -80°C until purification occurred. Cells were thawed on ice and resuspended in 20 mL Lysis Buffer (300mM NaCl, 50mM Na_3PO_4, 5mM Imidazole, pH 8.0). Lysozyme was added for a final concentration of 1 mg/mL and incubated on ice for 30 minutes. Cells were then sonicated for 2 minutes on ice and centrifuged at 14,000 rpm using a F14-14 × 50cy rotor for 15 minutes at 4°C. Supernatant was then filtered with a 0.22 µm syringe filter and run on the FPLC with a HisTrap HP column. Purified protein was dialyzed into 0.1M Sodium Bicarbonate Buffer (pH 8.3) for quantification and dye labeling.

Dye labeling: AlexaFluor594 NHS ester was purchased from Thermo Fisher Scientific (A20004). Nanobody (NB) was labeled according to the protocols from manufacturers. NB was purified and concentrated to 1 mg/ml then labeled and separated using an Amicon Ultra-4 Centrifugal Filter. Labeled NB (NB*) was aliquoted and stored for up to 12 months at 4°C. Once the labeling capacity of a NB* diminished, usually 2 months of use, a new aliquot was thawed.

Confocal Microscopy and Fluorescence Recovery After Photobleaching (FRAP): Cells transected for 24 - 48 hours were first blocked with 10% BSA in DMEM and incubated for 1 hr at 37°C. After incubation the BSA mixture was removed and a solution containing 0.325 µg/mL nanobody in Imaging Buffer was added and incubated for 15 minutes at 37°C.

The cells were washed three times with 2 mL of imaging buffer then imaged. A point-scanning confocal microscopy (Olympus Fluoview 3000) was used for FRAP measurements. A 16 pixel diameter (3.98 μm), circular region of interest containing Syx1a-EGFP was bleached using 488 nm excitation. Images were recorded at 2.17 seconds per frame while using both 488 nm and 561 nm lasers to image EGFP and Alexa594-NB*, respectively. FRAP data consisted of three frames prior to bleaching, followed by 3 seconds of bleaching and then observation of recovery for 100 frames. FRAP imaging took place at 20 – 22°C. The recovery was measured, corrected for photobleaching, and normalized against the average of the pre-photobleached frames, as described in our past work [65]. Graphpad Prism was used for all plotting, fitting and t-testing.

Total Internal Reflection <u>Fluorescence Microscopy</u> (TIRFM) and Single Particle Tracking: The cells, initially blocked with a 10% BSA enriched media, were incubated with 0.013 μg/mL dye conjugated nanobody in Imaging Buffer for a period of 15 minutes prior to washing. Imaging was performed as described here [107], [108]. Briefly, an inverted Nikon microscope equip with a 60x, 1.49 NA TIRFM objective and a 2.5x lens to further expand the image such that 1 pixel = 107 nm. A 491 nm laser and a 561 nm laser were used to excite EGFP and Alexa594 labeled NB, respectively. The fluorescence emission was detected after passing through a dichroic beam splitter (Chroma, Bellows Falls, VT) then into a Dual-View (Optical Insights, Exton, PA) that splits the fluorescence into a green and red channel. The green channel (emission filter, Chroma 525/50 nm) was used to identify cells transfected with Syx1a-EGFP and the red channel (emission filter, Chroma 605/75 nm) was used for tracking Alexa594-NB*. The images were collected on an Andor iXon 897+ EMCCD with a gain of 300 at a rate of 20 Hz and MicroManager was used for image acquisition.

Syx1a-EGFP tracking was performed as described[19] using SPT methods are freely available for Matlab [82], [83]. Briefly, image sequences were bandpass filtered to remove high frequency, single pixel, noise and low frequency background noise. Spots were located based on a threshold and size, then tracking was performed to connect localizations from one frame to the next. The maximum distance a particle was allowed to travel between consecutive frames (50 ms) was 7 pixels, where one pixel is 107 nm. From the trajectories, the step size displacements were calculated with a time difference of 200 ms (4 frames). The step size displacement histograms were fit according to:

$$y(r,t) = r\left(A_1 \exp\left(-\frac{r^2}{4D_1 t}\right) + A_2 \exp\left(-\frac{r^2}{4D_2 t}\right)\right) \tag{4.1}$$

Where, r is the distance traveled, the step size, during the time t = 200 ms. D_1 and D_2 are diffusion coefficients and A_1 and A_2 are amplitudes that are related to the fraction mobile and fraction immobile molecules here.

4.1.3 Results

Alexa594 conjugated nanobody binds specifically to transfected cells

To determine if the Alexa594 conjugated anti-EGFP nanobody (Alexa594-NB*) specifically binds Syx1-EGFP, transfected cells were incubated with Alexa594-NB* and imaged using a <u>confocal microscope</u> (Figure 4.1). Areas of the well that contained both transfected and non-transfected cells were specifically imaged to determine the specificity of the NB*-cell interaction; transfected cells retain red fluorescent NB*, but cells that are not transfected do not. A transfected cell (Figure 4.1A) sits among a collection of untransfected cells as seen in the brightfield image (Figure 4.1C). Excitation of Alexa594 shows that the Alexa594-NB* conjugate selectively binds the Syx1A-EGFP expressing cell (Figure 4.1B), but not the neighboring, non-transfected cells. Upon zooming into a region of the cell, the intensity of the NB* fluorescence overlaps with the intensity of the Syx1a-EGFP fluorescence (Figure 4.1D). An overlay of the cropped regions shows that clusters of Syx1a-EGFP are colocalized with the Alexa594-NB*. This visual conformation demonstrates that the nanobody conjugate is binding the target through the interaction depicted in Figure 4.1E, and not adhering non-specifically to cells.

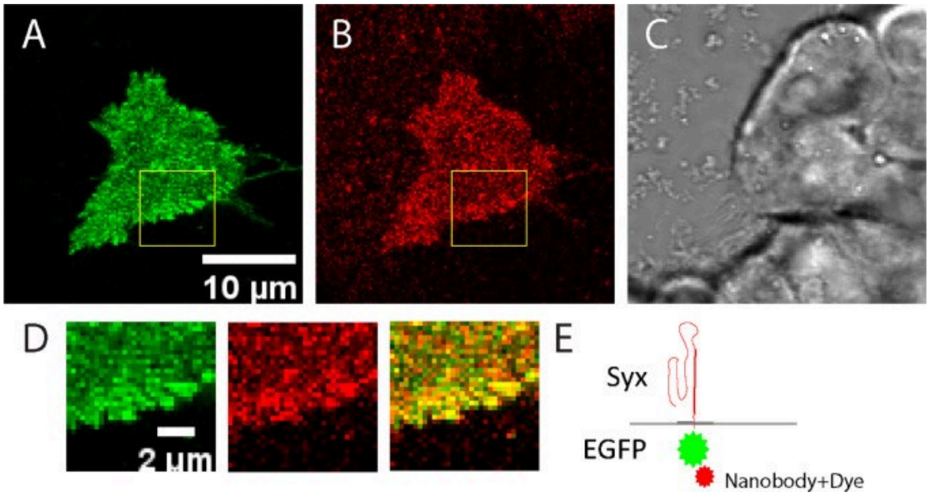

Figure 4.1 Live cells expressing Syx1A-EGFP plated on poly-L-lysine and incubated with anti-EGFP nanobody conjugated to Alexa594 (Alexa594-NB*) were imaged by confocal microscopy 24 hours post-transfection. A) 488 nm excitation of the EGFP on the outside of the cell attached to Syx1A. B) Excitation of Alexa594-NB* with 561 nm. C) Brightfield image of all cells present. D) Clusters are observed in a cropped region from A (green) and B (red) and overlaid (yellow). E) A schematic of the labeling system used for dye-substrate investigations. Syx1a-EGFP is transiently expressed on the surface of PC12 cells with EGFP on the cell exterior. Anti-GFP NB with or without dye is added in subsequent experiments.

The mobility of Syx1a-GFP is hindered by the presence of Alexa594 labeled NB and PLL surface coatings

FRAP was performed on Syx1a-EGFP (Figure 4.2) with no NB present, with unlabeled NB (NB) and with Alexa594-NB* (NB*) to determine if the NB or dye specifically affects the dynamics of Syx1a-EGFP. In all cases, the recovery of Syx1a-EGFP was below 100%, however immobile molecules are expected. It is well established that Syx1a forms clusters on the surface of cells [16], [23], [24], [28], [30] and these clusters are interchangeable with the surroundings [22], yet others observe that the mobile fraction between 0.6-0.7 [23]. In this work, Syx1a-EGFP recovered to 0.7 (Figure

4.2C). However, the mobility of Syx1-EGFP decreased in the presence of Alexa594-NB* when cells were grown on PLL (Figure 4.2). To determine if the loss of mobility was due to the dye or the NB, the mobility of Syx1-EGFP was measured in the presence of unlabeled NB and in the absence of NB. The results (Figure 4.2C-D) showed similar mobility for Syx1-EGFP with unlabeled NB and without NB added. The fraction mobile was reduced from 0.69 to 0.52, approximately a 25% reduction. However, the rate of recovery (Figure 4.2D) is not hindered; the molecules that are free are able to move normally. This suggests that the dye is interfering with the diffusion of Syx1-EGFP, creating an immobile portion.

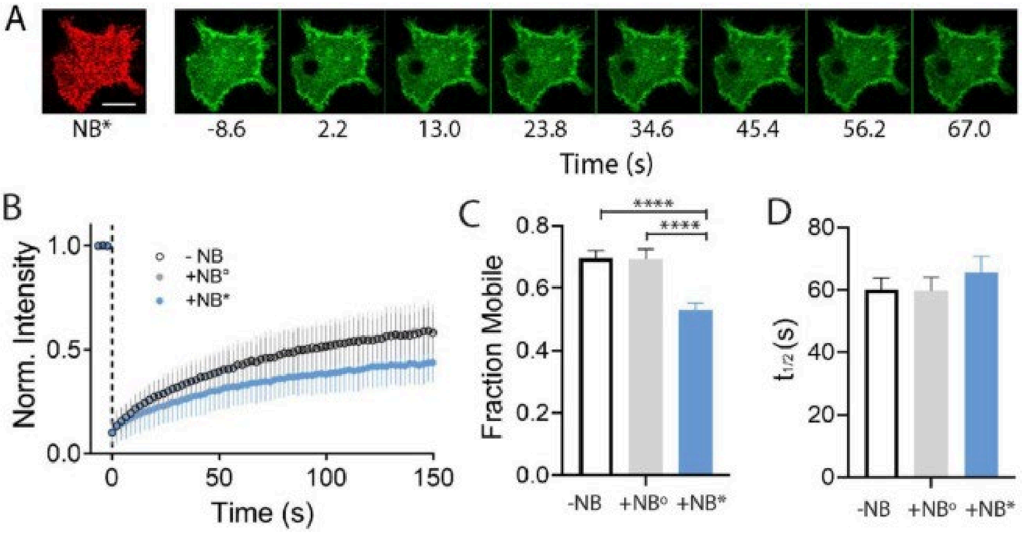

Figure 4.2 Poly-L-Lysine coated glass surfaces restrict the motion of transmembrane proteins bound to Alexa594 labeled nanobody, but not unlabeled NB. Cells were plated on poly-L-lysine (PLL), transiently transfected with Syx1aEGFP, then imaged and photobleached on a confocal microscope. NB, if present, was incubated on cells for 15 m prior to imaging and rinsed twice in imaging buffer. A) A confocal image of Alexa594-NB* (red) and a montage with images separated by 10.8 s (5 frames) of the photobleaching of Syx1a-EGFP. Scale bar, 10 µm. B) The FRAP recovery of Syx1a-EGFP with Alexa594-NB* present (+NB*, blue circles, N=18 cells), with unlabeled NB present (+NB°, grey circles, N=20 cells), and without NB present (-NB, empty circles, N=24 cells). C) The fraction mobile is reduced from 0.69 to 0.52 for samples with the dye present ($p < 0.0001$). D) The recovery rate, $t_{1/2}$, under the three conditions. Standard error is shown in all plots.

The mobility of Syx1a-GFP is restored by changing the surface coating to Fn. To determine the cause of the decreased mobility with Alexa594-NB*, the glass surface coating was changed. If the reduction of mobility is due to an interaction with the cell membrane, then the change in surface coating should not recover the loss of mobility. However, if the loss of mobility was due to the dye interacting with the surface coating, the change in surface coating could improve mobility. The Alexa594 dye is negatively charged and PLL is positively charged, which suggests that a dye-substrate interaction is likely. Therefore, Fn was tested as a new growth substrate. Fn has an overall negative charge, with a pI below 6, but the application of Fn to glass surfaces is not straightforward. Coverglass was etched with 3M potassium hydroxide to facilitate adhesion of Fn to the glass surface. Afterwards, FRAP was measured with identical conditions to Figure 4.2, with the exception that cells were grown on coverslips coated with Fn in place of PLL (Figure 4.3). The results demonstrate that the mobility of Syx1A-EGFP with the NB-dye conjugate was similar to that of cells without any NB added (Figure 4.3A-B). The fraction mobile was 0.71 and 0.70 for cells that contained no NB (-NB) and Alexa594-NB* (NB*), respectively (Figure 4.3C). The speed of the recovery, $t_{½}$, was also similar for Syx-EGFP in the presence and absence of Alexa594-NB* (Figure 4.3D). By changing the substrate to Fn, the restricted motion was fully recovered.

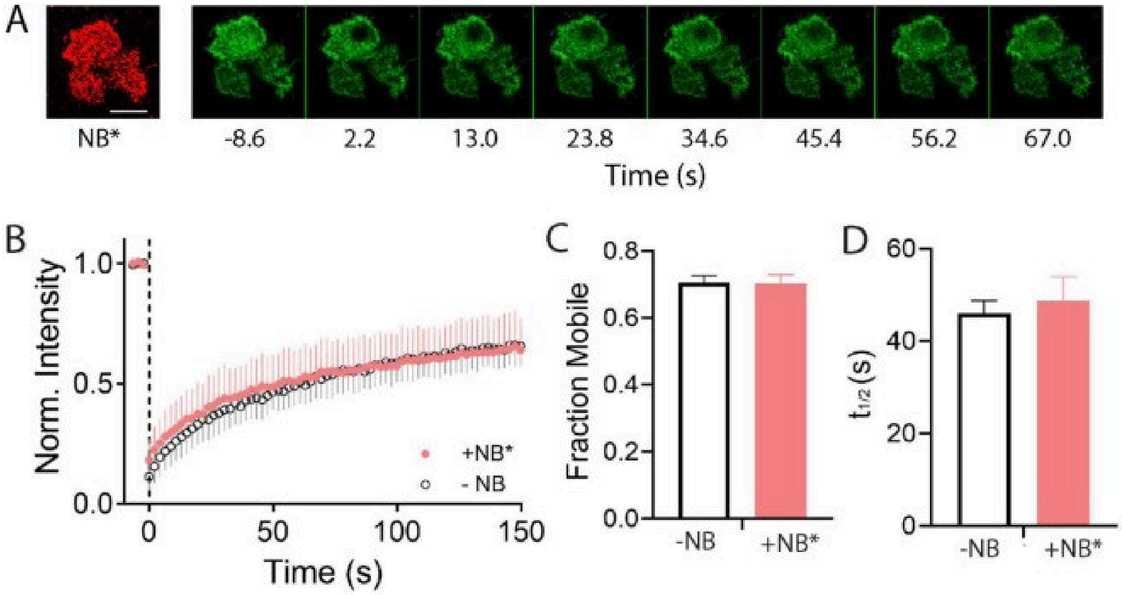

Figure 4.3 Fibronectin coated KOH-etched glass does not impede the motion of transmembrane proteins containing Alexa594 labeled nanobody. Glass was treated with KOH then coated with fibronectin (5 µg/ml) and cells were plated then transiently transfected with Syx1a-EGFP. A) A confocal image of Alexa594-NB* (red) and a montage with images separated by 10.8 s (5 frames) of the photobleaching of Syx1a-EGFP. Three cells are in the image. Scale bar, 10 µm. B) Recovery of Syx1a-EGFP (empty circles, *N* = 15 cells) and Syx1a-GFP with Alexa594-NB* (pink circles, *N* = 15 cells)), C) The fraction of Syx1a-GFP that remains mobile, and D) the rate of recovery with (NB*) and without the Alexa594-NB* (-NB). No statistically significant differences were observed between without NB and with labeled NB on fibronectin coated dishes. Standard error is shown in all plots.

Fibronectin adheres well to KOH etched glass, but this treatment process requires a challenging preparation because concentrated KOH is not ideal to use due to its corrosive nature and strong vapors, therefore glass was treated in other ways to facilitate Fn coating. We used PLL first then adhered Fn. This led to slow and inconsistent movement of Alexa594-NB* labeled Syx1a-EGFP in FRAP experiments (Figure 4.6). Increasing the concentration of Fn did not alleviate the slow motion (Figure 4.6B). Therefore, this method was discontinued. Next, glass was cleaned by dipping in ethanol and flamed, followed by Fn coating. This method was simple to perform and did not impede motion of the Alexa594-NB* labeled Syx1a-EGFP in FRAP experiments (Figure 4.4). The fraction mobile is the same with and without the Alexa594-NB* present (Figure 4.4C). Qualitatively, cells also appeared more spread out on flame treated glass coated with Fn as opposed to KOH etched glass treated with Fn. This is observable by comparing representative cells shown in Figure 4.3A and 4.4A.

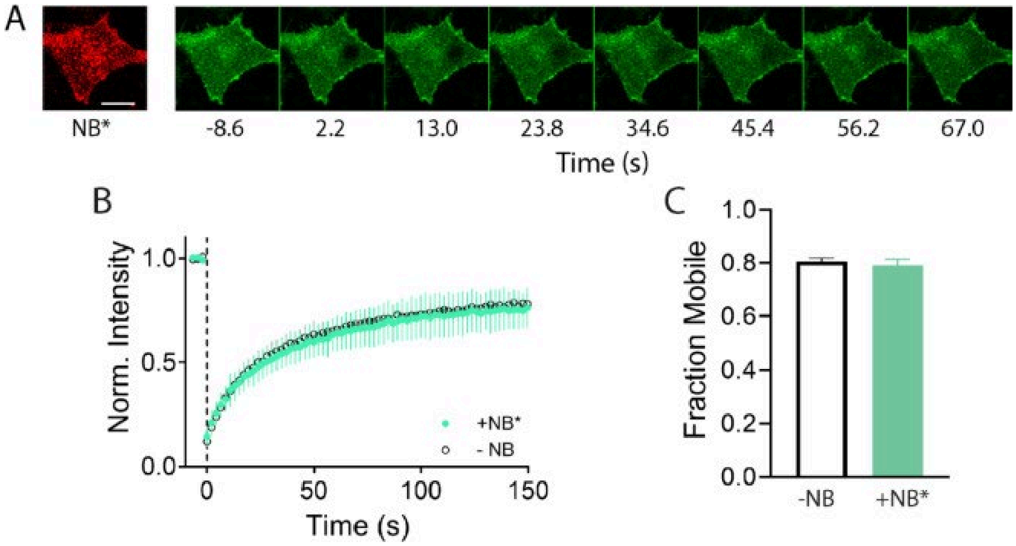

Figure 4.4 Fibronectin-coated, flame-treated glass does not impede the motion of transmembrane proteins containing Alexa594 labeled nanobody. Glass was treated by dipping in ethanol and flamed then coated with fibronectin (20 µg/ml) and cells were plated then transiently transfected with Syx1a-EGFP. A) A confocal image of Alexa594-NB* (red) and a montage with images separated by 10.8 s (5 frames) of the photobleaching of Syx1a-EGFP. Scale bar, 10 µm. B) Recovery of Syx1a-EGFP (empty circles, N=20 cells) and Syx1a-EGFP with Alexa594-NB* (green circles, N = 18 cells)), C) The fraction of Syx1a-EGFP that remains mobile with (NB*) and without the Alexa594-NB* (-NB). No statistically significant differences were observed between without NB and with labeled NB on Fn coated dishes. Standard error is shown in all plots.

Single Particle Tracking (SPT) methods show similar restrictions in dynamics with PLL coated surfaces

To determine if conclusions from FRAP experiments could be applied to other measurements of membrane protein dynamics, SPT experiments were performed on Alexa594-NB*. The NB* concentration was reduced 10-fold to facilitate tracking of single molecules. Molecules were imaged at 20 frames/second and then tracked. From the trajectories, the step size distributions and average step size for Alexa594-NB* on PLL and Fn over the course of 200 ms (4 frames) was measured (Figure 4.5). The average step size for Alexa594-NB* attached to Syx1a-EGFP is approximately double for Fn coated surfaces compared to PLL (Figure 4.5B). The histogram of the observed step sizes (Figure 4.5A) shows a larger immobilized portion for PLL with a higher portion of small step sizes when compared to Fn.

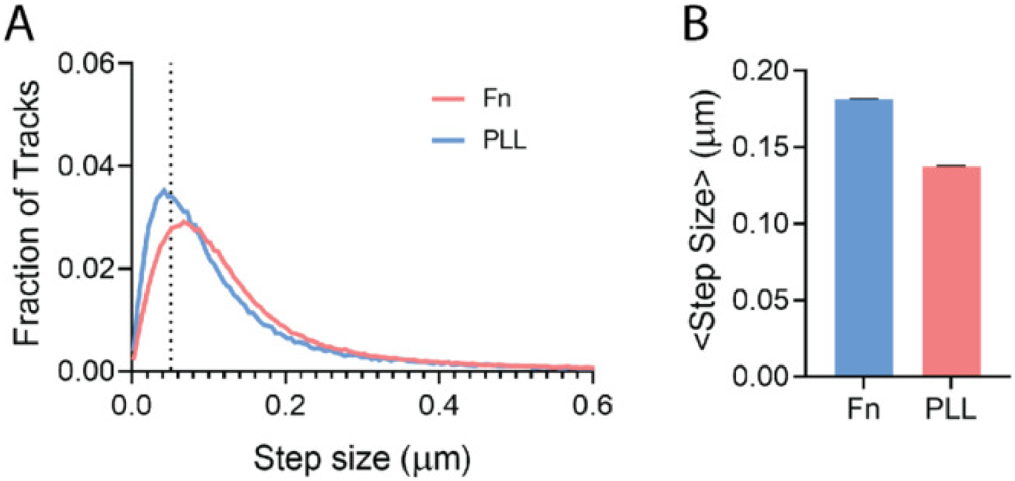

Figure 4.5 Single molecule trajectories show reduced mobility on PLL relative to Fn. Single Alexa594-NB* molecules were tracked on the surface of Syx1a-EGFP containing PC12 cells using TIRF microscopy**.** A) The distribution of step sizes for Alexa594-NB* on cells expressing Syx1a-EGFP and grown on either PLL or Fn coated coverglass. The dotted line is the mean step size from fully immobile particles adhered to PLL coated coverglass in the absence of cells. The step size was measured over 200 ms. B) The average step size on different surface coatings. Error bars are SEM.

To quantify the fraction of tracks that are immobile, Alexa594-NB* was immobilized by adhering to the surface of the PLL coated glass in the absence of cells. Immobilized NB* was tracked and the step size distribution was measured. All three distributions (immobilized, PLL and Fn) were fit to a two-component diffusion equation shown below, to determine the rate of motion and portion of slow and fast tracks on each substrate (Eqn 4.1).

The slow component of the immobilized NB* (shown as a dotted line in Figure 4.5A) was used to constrain the fit for Syx1a-EGFP labeled with Alexa594-NB* on PLL and Fn coated surfaces. From the fit of the step size distribution, the fraction of particles moving slowly was calculated; 17% of the tracks are immobile on Fn coated surfaces and 36% of the tracks are immobile on PLL coated surfaces.

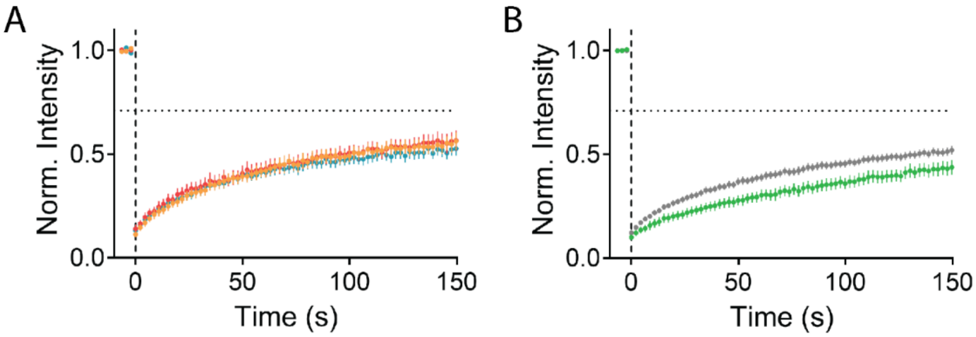

Figure 4.6 PLL then Fn coated glass impedes motion of Syx1a-EGFP**.** Glass was coated with PLL then A) 2 µg/ml of Fn The average of 5-7 cells was recorded on three

independent days for A (orange, blue and red) and the day to day variation is small. B) Fn concentration was 50 µg/ml (green) and compared to the average of the 2 µg/ml experiments (gray). The horizontal, dotted line is the plateau reached with Fn coated on KOH etched glass, shown in Figure 3. For all traces, error bars are SEM.

4.1.4 Discussion

One challenge for the accurate measurement of protein motion is that some membrane proteins are immobile due to pertinent biological interactions (*i.e.* clustering), whereas other membrane proteins, within the same cell, may be immobile due to issues with substrate interactions. Therefore, it is of utmost importance to reduce immobilization artifacts when measuring dynamics. In this work we describe a simple FRAP-based assay that allows for the specific characterization of the role of an organic dye on membrane protein motion by comparing the dynamics of Syx1a-GFP with a nanobody that has or doesn't have a red dye attached. We focus on a commonly used red fluorescent dye, Alexa594, and common surface coatings used for cell attachment.

To test for interactions that interfere with dynamic measurements, we used a differential, FRAP-based measurement, where the interference in protein diffusion due to the dye could be separately assessed relative to the interference due to the NB alone. The NB specifically binds transfected cells (Figure 4.1) where a model transmembrane protein, Syx1a-EGFP, presents EGFP on the exterior surface. In the control lacking any NB, Syx1a-EGFP recovers at about 70% (Figures 4.2B, 4.3B, 4.4B) on both Fn and PLL coated coverglass. This is in close agreement with others, where it is well established that Syx1a forms clusters on the surface of cells [16], [22], [23], [28], [30], [33] and these clusters are interchangeable with the surroundings [16], [23]. However, a portion (30-40%) of these molecules are immobile in FRAP measurements [23]. This recovery is increased when cytoplasmic domains of the protein that are known to interact with other molecules, such as the SNARE domain, are removed [23], suggesting that the immobile fraction is physiologically relevant.

Although cells adhere well to PLL coated coverglass, the dynamics of transmembrane proteins with dye labeled NB is inhibited. The Alexa594 dye on the NB hindered diffusion significantly more than the NB alone and the mobile fraction was reduced (Figure 4.2) from 0.69 to 0.52 (Figure 4.2B). Approximately ¼ of the mobile particles become immobile due to substrate interactions. This is not due to the NB alone because unlabeled NB does not show a decrease in mobility (Figure 4.2).We hypothesized that the negatively charged dye interacts with the positively charged PLL surface coating, as suggested by others [101], [109]. Interactions have been observed previously for Congo Red, a negatively charged dye, and PLL via electrostatic interactions through two sulfonate groups. In this work, a change in the pH to 11 abolished the interaction [109], however this was not an option for cells in culture. Therefore, the surface coating was altered to test how protein dynamics are affected by the choice of glass coating for cell adhesion. Upon changing to Fn, protein mobility returned (Figure 4.3) and the mobile fraction was restored. This demonstrates that the decrease in mobility on PLL is not due membrane interactions of the dye because the mobility is retained when the surface coating is changed to Fn. Therefore, this reduction in mobility is directly due to an interaction between the substrate and the dye, as others have suggested for different dyes and substrate combinations [101], [109].

Fibronectin came with challenges since it does not coat glass easily and several treatments of the glass were tested. Both KOH etched glass, which creates flat surfaces

[106], and flame treated glass were easily coated with Fn and retained mobility in FRAP measurements (Figure 4.3 and 4.4). However, when PLL was deposited prior to Fn to facilitate Fn adherence, dynamics were still hindered (Figure 4.6). This suggests that Fn may not fully cover the surface and additional Fn did not solve this issue (Figure 4.6B).

To determine if the mobility measured by FRAP was translatable to other dynamic measurements, SPT was performed on cells containing Syx1a-EGFP and Alexa594-NB*. Note that in SPT measurements the red fluorescent NB channel was tracked and in FRAP data, the green fluorescent Syx1a-EGFP was measured. Based on the FRAP measurements, we expected that approximately 20-30% of spots observed in single molecule tracking should be confined or immobile (Figures 4.2C, 4.3C, and 4.4C) on Fn coated surfaces and approximately 50% should be immobile on PLL coated surfaces (Figure 4.2C). Based on the step size distribution from single molecule trajectories, approximately 17% of tracks were immobile on Fn. This increased to 36% on PLL and SPT measurements appeared slightly more mobile than FRAP. The reason for the differences between the FRAP and SPT measurement of the immobile fraction is not entirely understood, but it is useful to note that the FRAP measurement measures the mobility over a larger distance with lower time resolution than SPT and often the rate of diffusion measured in SPT measurement is faster [110], [111]. In our work, the overall trend was the same; PLL immobilized the motion of transmembrane proteins significantly more than Fn.

Although mobility is an important factor for choosing substrates, Fn is also a natural choice for cell adherence. Fn is an extracellular matrix protein with binding sites that interact specifically with integrins, the glycoproteins responsible for cell binding and adhesion [104], [105], whereas PLL relies on cell adhesion through electrostatic interactions. PLL has been used extensively for growing a wide variety of cells, including PC12 cells like those used here [16], [22]. Fibronectin has also been used successfully with PC12 cells [103], [105], [112], [113]. However, other alternative coatings should be tested. Linearized PEG may be another good choice for a substrate coating with low interactions and no net charge [101] and a Tween20 based substrate coating may be another option for *in vitro* work requiring low substrate-dye interactions [114].

4.1.5 Conclusion

In conclusion, we recommend testing dyes with the substrates prior to cell dynamics measurements but demonstrate that Fn is a better choice than PLL for the Alexa594 dye tested here. Results here show that PLL is a poor choice of substrate for dynamics studies of transmembrane proteins with exogenous dye labeling (Figure 4.2). However, Fn shows no inhibition of dynamics in FRAP based measurements (Figure 4.3). Fn is easily coated onto glass that has been flame treated and cells readily attach (Figure 4.4). Additionally, a novel, FRAP-based assay was designed to directly compare the dynamics of an EGFP-labeled membrane protein with and without the addition of a dye conjugated NB and this assay aligns well with single molecule tracking experiments (Figure 4.5).

4.2 Syntaxin clusters and cholesterol affect the mobility of Syntaxin1a

Syx1a is essential for stimulated exocytosis in neuroendocrine cells. The membrane docking process involves the formation of nanoscale Syx1a domains on the plasma membrane once vesicles arrive and the loss of Syx1a during the fusion process. Syx1a nanodomains are both static yet empty and refill and the process by which these clusters maintain this balance is unclear. In this work, the dynamics of the Syx1a molecules is elucidated relative to the cluster position through a labeling strategy that allows both the bulk position of the Syx1a clusters to be visualized concurrent with the trajectories of single Syx1a molecules in PC12 cells. Single Syx1a molecules were tracked in time relative to cluster positions to decipher how Syx1a moves within a cluster and when clusters are not present. Syx1a is mobile on the plasma membrane but less mobile near the edges of clusters and this depends on the presence of the N-terminal, Habc, domain and cholesterol, both of which are needed for exocytosis. The depletion of cholesterol dramatically reduces the mobility of Syx1a within clusters and less so over the rest of the plasma membrane. This suggests that fluidity of Syx1a supramolecular clusters is needed for function.

4.2.1 Introduction

The organization of cell membranes is tightly regulated for proper function and this organization leads to nanoscale domain formation where the clustering of proteins can affect function. Many types of membrane proteins form supramolecular clusters to regulate activity [23], [115]–[117], or to transmit a signal to the interior of the cell [118]. Often the proteins within clusters interchange dynamically with free protein, located outside of a cluster [16], [23] while the clusters themselves appear static. SNARE proteins, the regulators of membrane fusion, form supramolecular clusters to facilitate the fast fusion of vesicles docked to the plasma membrane [16]. The exchange of molecules can affect cluster size and function, thus, the dynamics of membrane proteins and the exchange of free proteins within supramolecular clusters are of great interest as a mechanism of regulating secretion.

Secretion of dense core vesicles and synaptic vesicles occurs at sites where Syx1a molecules, a SNARE protein on the plasma membrane, accumulate [119] and several copies of Syx1a are required for fusion [120]. Syx1a clusters contain 60-80 copies of Syx, more than required for fusion, and clusters are stable in their location, yet empty and refill on the order of several seconds [22]. The Syx clusters are thought to form through interactions between the SNARE domain [28] or the transmembrane domain [30]–[32]; however the SNARE domain interactions are hindered by the N-terminal Habc domain, which acts as a flap that folds upon the SNARE domain to block interactions with the assistance of Munc18 [99]. Munc18 is found where Syx1a clusters at docking vesicles [121] with the Habc domain required for Syx1a to cluster properly at docking sites [16].

The membrane also plays an important role in the clustering and dynamics of Syx1a. Syx1a clusters depend on cholesterol [35] and the depletion of cholesterol corresponds to a loss of clusters in PC12 membrane sheets [30]. The loss of cholesterol also reduces vesicle mobility and fusion [122], [123]. It is generally thought that cholesterol is enriched in domains that contain ordered lipids and cholesterol acts to break up lipid acyl chain interactions, leading to a more fluid membrane at physiological temperature [124]. In several cell studies, the loss of cholesterol reduces mobility of a variety of plasma membrane proteins [125], suggesting this is a universal feature and not protein specific. Syx1a clusters also recruit PI(4,5)P2 by binding through a polybasic region near the transmembrane domain of Syx1a [126], however this is not required for Syx1a cluster formation, only fusion [127].

In this work, the mobility of single Syx1a proteins has been measured relative to Syx1a clusters. To measure both cluster and single molecules simultaneously, Syx1a-EGFP was transiently expressed in PC12 cells under a truncated promotor to limit overexpression [128]. The cluster positions are evident from Syx-EGFP and single molecules were visualized by sparsely labeling with a red fluorescent nanobody to EGFP [129]. The dynamics of Syx1a near clusters is surprisingly mobile, but this mobility depends on both the presence of cholesterol and the Habc domain. Loss of cholesterol hindered motion throughout the cell and truncation of Syx1a to remove the Habc domain led to a reduction in motion within clusters.

4.2.4 Materials and Methods

Table of reagents:

Reagent	**Manufacturer**	**Part Number**
DMEM	Gibco	11965-092
HS	Hyclone	SH30074.03
FBS	Atlanta Biologicals	S11150
Fibronectin	Gibco	33016-015
Lipofectamine 3000	Invitrogen	L3000-008
NaCl	Fisher	S271-3
KCl	ACROS	42409-0010
MgCl2	Sigma	M4880-100G
CaCl2	Sigma	
D-Glucose	Sigma	G8270-1KG

HEPES	Sigma	H3375-250G
LB	Alpha Biosciences	L12-1112
Ampicillin	Fisher	BP1760-25
IPTG	GoldBio	12481C50
MBCD	Sigma	C4555-5G
Versene	Gibco	15040-066

Cell Culture

PC12-GR5 cells were cultured in DMEM (high-glucose) supplemented with 5% HS and 5% FBS and stored at 37°C/5% CO_2 in T25 cell culture flasks (Life Science Products). Cell media was changed every two days. For imaging experiments cells were plated on coverslips containing 20µg/mL Fibronectin for a period of 24 hours prior to transfection with Lipofectamine 3000 as described in the manufacturers protocol, using 100 ng of desired plasmid. Cells were then imaged 24 hours post transfection using imaging buffer (140mM NaCl, 3mM KCl, 1mM MgCl2, 3mM CaCl2, 10mM D-Glucose, 10mM HEPES, pH 7.4). Cells were transfected with the WT or dNT Syx1a 24-48 hours prior to imaging. The high expressing CMV promotor was used for FRAP and the lower expressing, delta CMV promotor was used for TIRF imaging. For MβCD experiments, WT cells were subjected to 30 min of incubation with DMEM containing 15mM MβCD. Cells were washed 3x with imaging buffer prior to imaging.

Nanobody Purification and Labeling

Anti-EGFP nanobody plasmid was procured from (Addgene, #49172) and transformed into BL21 cells for purification. Starter cultures (10 mL) were made in LB media with 2000x amp (100 mg/ml) and used to inoculate 1L culture the next day. Cultures were grown at 37°C until OD600 reached 0.9, then temperature was changed to 20°C following induction with IPTG (1 mL,1M). The culture was given 24 hours to express the anti-EGFP nanobody, after which the bacteria was pelleted with a centrifuge at 6000 x g for 15 min at 4°C. Pellets were stored at -80°C until purified. For purification, pellets were thawed on ice and resuspended in 20 mL lysis buffer (300mM NaCl, 50mM Na3PO4, 5mM Imidazole, pH 8.0) and a concentration of 1 mg/mL Lysozyme was added and the lysate mixture was then sonicated for 2 minutes and then centrifuged at 14,000 rpm for 15 min at 4°C. The resulting supernatant was then filtered using a 0.22 µm syringe filter prior to being purified on the FPLC with a HisTrap HP column. The resulting fraction of interest was dialyzed with 0.1M Sodium Bicarbonate Buffer (pH 8.3) for concentration quantification and dye labeling.

Dye labeling with AlexaFluor594 was accomplished with AlexaFluor594 NHS ester from Thermo Fisher Scientific (A20004) and was done following the manufacturer's protocol. The Nanobody was concentrated to 1 mg/mL for labeling using Amicon Ultra-4 Centrifugal Filter. After labeling was completed, nanobody was separated from free dye using Amicon Ultra-4 Centrifugal Filter.

Total Internal Reflection Fluorescence Microscopy

Cells were imaged 24 hours post transfection. Samples were blocked with 10% BSA enriched DMEM and allowed to incubate with this solution for 15 minutes, after which samples were incubated with 0.013 ug/mL AlexaFluor594 anti-EGFP nanobody for 15 minutes. Samples were then rinsed 3 x with imaging buffer prior to imaging. For MBCD experiments, 50ug/mL MBCD was added to all steps.

For single molecule tracking experiments, data were taken with a DualView (Optical Insights) that splits the red and green fluorescence (565LP dichroic with 525/50 and 605/75 emission filters, Chroma Technologies) into separate channels onto an EMCCD (Andor iXon897). The red and green images were then aligned using 200 nm carboxylate modified, yellow-green fluospheres (ThermoFisher) and a home-built MATLAB code. Syx cluster positions were located by bandpass filtering with 9 pixels followed by spot finding with a pixel size of 5 and a variable threshold. Centroid positions were then detected on the bandpassed image. Tracking of the nanobody channel was accomplished by bandpass filtering to a pixel size of 7 and then spot finding over all frames with variable intensity threshold. The maximum distance a spot could move over one frame was 7 pixels, where one pixel is 0.107 um. Only tracks that were longer than 15 frames (50ms/frame) were used for subsequent analyses. The resulting tracking data along with cluster localizations were used to calculate the mean square displacement (MSD) and step size relation to cluster locations. All tracking code was initially written in IDL then made available in MatLab [82]. Analysis of tracks relative to cluster positions is new and described below.

Mobility was measured as a function of distance to the nearest cluster by first calculating step sizes (dt = 200 ms, 4 frames) and pairing that with the distance to the nearest cluster from the beginning of the step. The steps for all tracks were compiled and binned according to distances [0, 0.25, 0.5, 1, 2.5, 3.7, 256] in pixels. This was done for each cell. The bins for each cell were then averaged. The cells were then averaged and the SEM was calculated from cell to cell. For all tracking data the following number of cells was used: WT , dNT, WT with MBCD.

For all SyxWT tracking data, 21 cells from 3 days were analyzed. For SyxdNT 22 cells from 3 days were analyzed and for SyxWT treated with MBCD 23 cells from 3 days were analyzed. SyxWT control cells were measured on the same days as dNT and with the MBCD treated cells.

To calculate the precision in our single molecule tracking measurements, Alexa594-NB was adhered to a poly-L-lysine coated surface and imaged as described above. To determine the localization precision, the standard deviation of the position was calculated according to methods described previously [130]. The precision in x and y was the same and was 39 nm (n = 3 movies and 167,622 tracks).

Confocal Imaging and FRAP

Imaging and FRAP were performed on a point-scanning confocal microscopy (Olympus Fluoview 3000). The FRAP region was a 16 pixel diameter (3.98 μm) circular region with the bleaching laser being 488 nm. Imaging rate was 2.17 seconds per frame using the 488 nm laser. Pre-bleach imaging consisted of 3 frames followed by 3 seconds of bleaching. Post bleach imaging consisted of 100 frames for recovery to occur. FRAP occurred at room temperature 20-22C. FRAP data was measured and then corrected for photobleaching and normalized to the average of the pre-bleach frames as described in previous work [65]. Graphpad Prism was used for plotting, fitting and t-testing.

4.2.2 Results

To determine how Syx1a microdomains affect the motion of Syx1a molecules, Syx1a-EGFP was labeled at a low level with a red fluorescent anti-GFP nanobody (“Syx1a-

NB”) and tracked. Syx1a tracks were then compared to the Syx1a-EGFP cluster positions and dynamics were determined as a function of the proximity of Syx1a domains (Figure 4.7). Example Syx1a-NB trajectories are overlaid on Syx1a-GFP cluster images in Figure 4.7A-E, where blue in the track marks the start position. Syx1a is mobile and observed as leaving and entering clusters in A-C, however immobile Syx1a molecules are also observed at clusters (Figure 4.7D) and non-cluster positions (Figure 4.7E). To measure if the observed immobile Syx1a molecules were moving slowly or immobilized completely, the NB was immobilized on the glass surface, imaged and tracked for comparison (Figure 4.7F). On average, the Syx1a-NB moves at a rate of 0.05 $\mu m^2/s$, as measured by the initial slope of the mean square displacement in time of individual trajectories. This is significantly more mobile than the NB stuck to the glass surface, where the molecules move at a rate of 0.005 $\mu m^2/s$ (Figure 4.7G). The mobility of Syx1a-NB as a function of distance to the nearest cluster reveals that Syx1a molecules in the center of the cluster are free to move more than molecules that are a certain distance from the cluster center (0.2 µm) and the Syx1a molecules that are further from the cluster move at a rate slightly higher (Figure 4.7H).

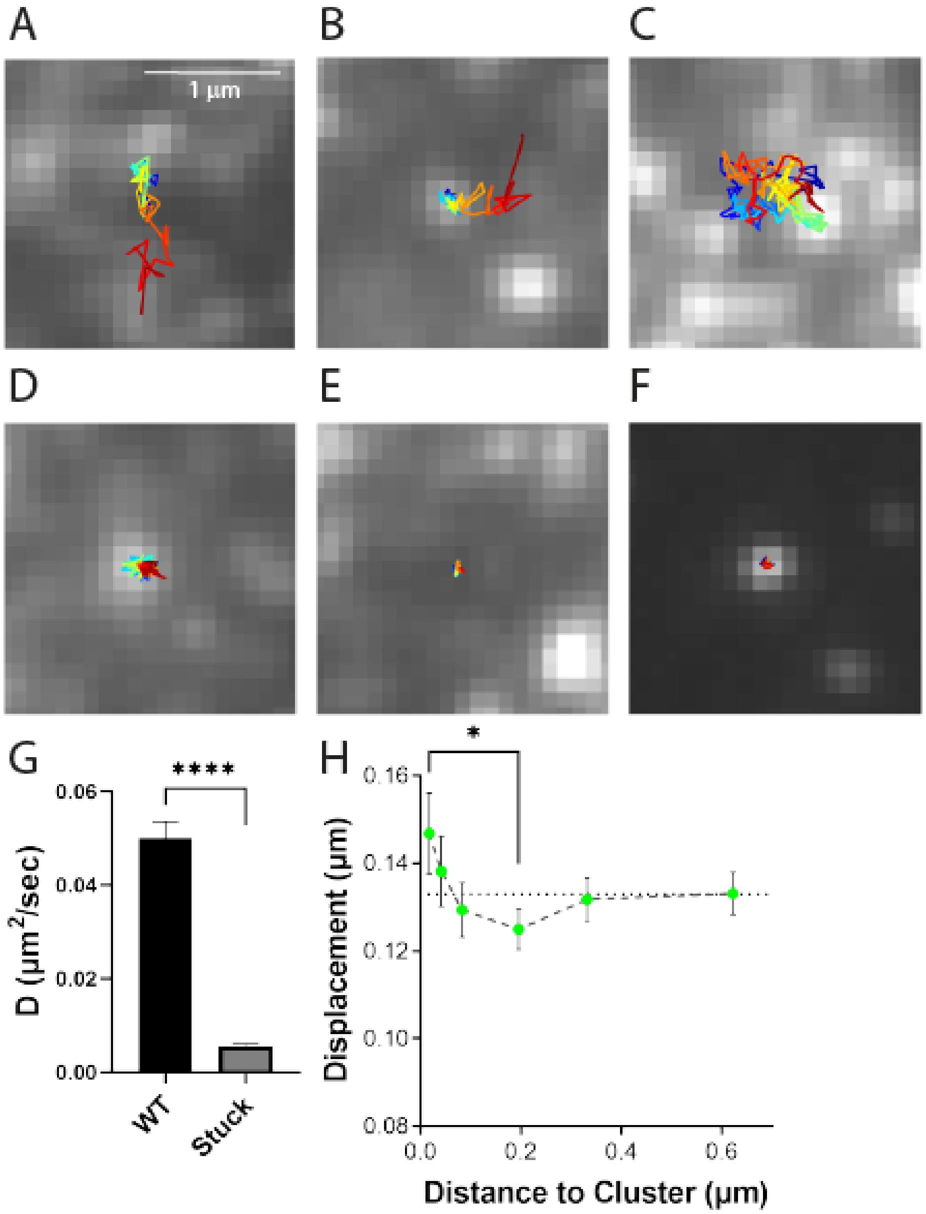

Figure 4.7 Tracking of a red fluorescent antiEGFP nanobody attached to Syx1a-EGFP ("Syx1a-NB") in PC12 cells. Example tracks in live cells are show in A-E, with F being the nanobody stuck to a glass surface. Tracks start blue and then turn red over the course of time. A) Molecule entering a cluster domain. B) Molecule leaving a cluster domain. C) Molecule entering and then leaving a cluster domain. D) Molecule immobile at cluster. E) Molecule immobile not at a cluster. F) Syx1a-NB stuck to a glass surface and tracked. G) Bulk diffusion coefficient from tracked WT cells (n = 21) compared to stuck NB on PLL (n = 6). H) Distance vs average displacement. Displacements were binned based on their distance to a cluster and averaged. Dashed line indicates the plateau of displacement far from clusters. Significance between bins 1 and 4.

The formation of clusters has been proposed to be due to SNARE domain interactions between Syx1a molecules [28] and this interaction is limited by the Habc domain [131]. To determine the role of the Habc domain and the SNARE domain, truncated forms of Syx (SyxdNT and SyxTMD) were used (Figure 4.8). The SyxdNT construct lacks the N-terminal regulatory domain that is known to fold onto the SNARE domain and thought to reduce SNARE domain interactions [131]. The SyxTMD lacks most of the SNARE domain and the N-terminal domain. If the Syx SNARE domain is responsible for clustering, Syx dynamics should be affected in the form that allows for more SNARE interactions (SyxdNT) and be reduced in the form that lacks the SNARE domain (SyxTMD). Figure 4.8A shows the constructs tested. All contain a GFP that resides on the outside of the cell, however, when labeling with the NB, no labeling occurred with the SyxTMD. Upon further investigation using confocal microscopy (Figure 4.8B-D), the SyxTMD was clearly trapped within the cell (Figure 4.8D), whereas surface labeling was observed for both SyxWT (Figure 4.8B) and SyxdNT (Figure 4.8C). Line scans of the confocal images further supports that fluorescence is increased at the cell membrane for SyxWT and SyxdNT, but not for SyxTMD. Additionally, both SyxWT and SyxdNT were able to be labeled by the addition of NB, further supporting that they are indeed on the plasma membrane and SyxTMD is not. Therefore, the tracking studies of SyxWT and SyxdNT were possible and SyxdNT revealed slightly, but not significantly reduced mobility on the cell surface. Clusters were observable, but others note that the clusters formed by SyxdNT do not colocalize as well to docked vesicles as Syx1a clusters [20]. The mobility of SyxdNT as a function of distance to a cluster was not significantly different anywhere along the curve, with no hindrance at the border of clusters or enhancement at the center of clusters as observed to Syx1a-NB dynamics.

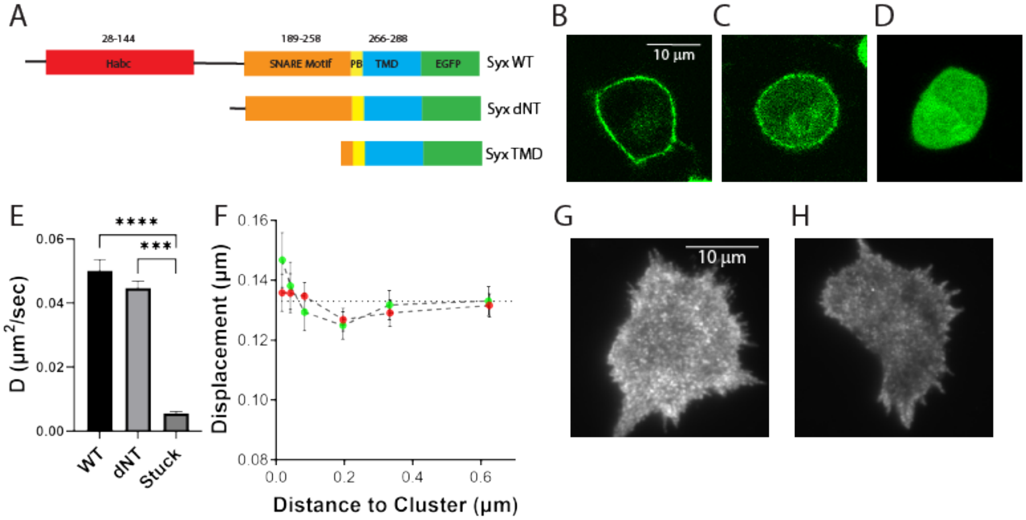

Figure 4.8 Syx1a dNT mutant tracked in PC12 cells. A) Representation of protein domains of Syx1a WT, Syx1a dNT, and Syx1a TMD. B – D) Confocal images of Syx1a WT, dNT, and TMD imaged halfway through the cell. E) Bulk diffusion coefficient from tracked WT cells (n = 21), dNT (n = 22), and stuck NB on PLL (n = 6). Distance vs average displacement. Displacements were binned based on their distance to a cluster and averaged. Dashed line indicates the plateau of displacement far from clusters. G) WT PC12 cell imaged on TIRF show clustering. H) dNT PC12 cell imaged on TIRF show clustering.

It is interesting that the rate of motion within clusters is higher than the motion 200 nm away. One hypothesis for why this could occur is due to the local lipid environment which can alter the viscosity and thickness of the membrane. To determine if the viscosity/thickness within clusters could be affecting the rate of motion, cholesterol was depleted from the membrane. The local lipid environment is known to be involved with the clustering of Syx. Cholesterol stabilizes raft-like domains and is needed for cluster formation [35] and cholesterol enhances the speed which molecules move in cell membranes [123], therefore we hypothesized that Syx1a motion would be reduced. Upon treatment of PC12 cells with MBCD, which depletes cholesterol, cells were dramatically transformed (Figure 4.9). SyxWT moved slower yet clusters were still clearly visible. The rate of diffusion dropped approximately 25% and often cells were reduced in size. Interestingly, the motion of molecules near cluster decreased the most (Figure 4.9D). This aligns well with a model in which cholesterol breaks up SNARE interactions, similar to that of cholesterol-lipid interactions. The clusters, enriched in Syx1a have more protein content and therefore depletion of cholesterol has a more profound affect on the dynamics (Figure 4.9D), suggesting that cholesterol is involved with enhancing the mobility of Syx1a within clusters and this likely occurs by altering the viscosity or membrane thickness locally.

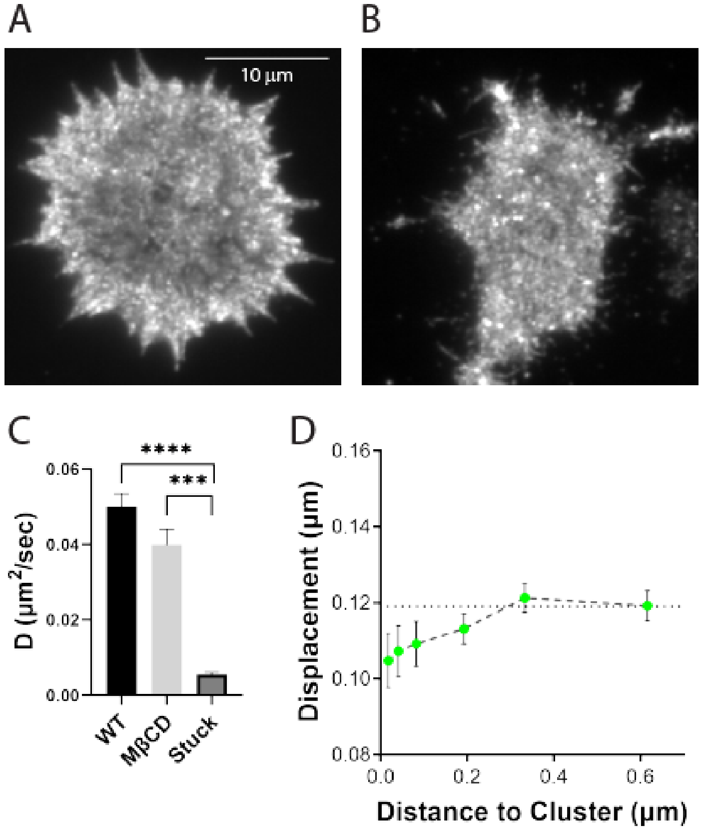

Figure 4.9 Treatment with MBCD prior to imaging. Cells were treated with 15mM MBCD for 30 minutes prior to imaging. A) PC12 cell transfected with WT Syx1a untreated with MBCD. B) PC12 cell transfected with WT Syx1a treated for 30 minutes prior to imaging. Bulk diffusion coefficient from tracked WT cells without MBCD treatment (n = 21), with MBCD treatment (n = 23) and stuck NB on PLL (n = 6). Distance vs average displacement. Displacements were binned based on their distance to a cluster and averaged to create data points in the graph. Dashed line indicates the plateau of displacement far from clusters.

As a secondary experiment to determine that mobility for both the dNT construct and cholesterol depletion appeared in ensemble measurements, FRAP was performed on PC12 cells expressing WT Syx1a and dNT Syx1a. Cholesterol depletion was performed the same as with SPT experiments with the exception that no nanobody was added during MBCD treatment. FRAP traces can be seen in (Figure 4.10A) with the bulk diffusion coefficient and percent recovery in (Figure 4.10B) and (Figure 4.10C) respectively. WT and dNT are similar in their diffusion coefficient, while Syx1a in cells depleted of cholesterol have greatly reduced mobility. WT has a larger percent recovery but not significantly different than dNT and MBCD, which exhibit similar recovery. This suggests that the observations for single molecule motion aligns well with the bulk in regards to Syx1a mobility.

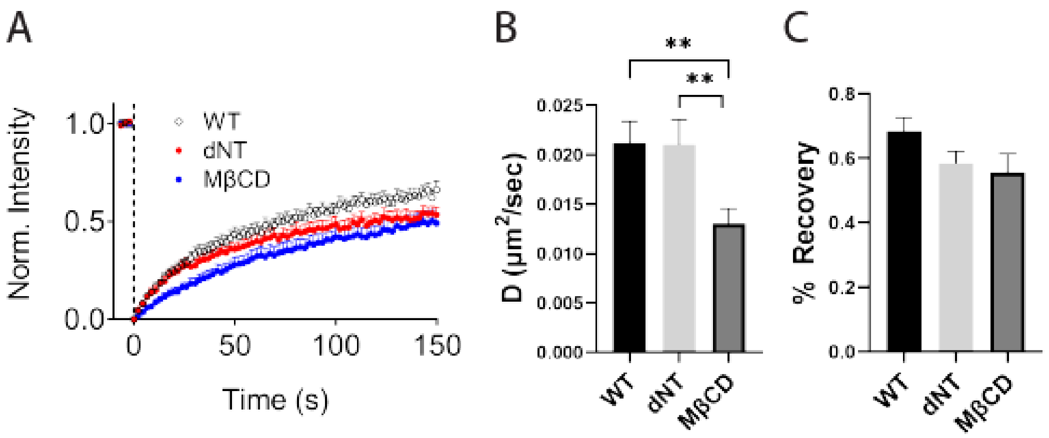

Figure 4.10 FRAP of PC12 cells expressing WT or dNT Syx1a and WT with addition of MBCD. A) FRAP trace of three sample types. B) Diffusion coefficients fit from the FRAP trace. C) Percent recovery of FRAP traces. WT (n = 16), dNT (n = 12), MBCD (n = 14).

4.2.3 Discussion

In this work we demonstrate a simple method to simultaneously measure Syx plasma membrane clusters and the dynamics of the individual proteins that enter and leave the clusters. By sparsely labeling with a red-fluorescent, anti-EGFP nanobody for tracking and more broadly by transfecting with an EGFP labeled protein for cluster localization, dynamics at cluster positions can be elucidated. The Syx1a-EGFP construct used was one with a truncated promotor to limit the expression but allowed for clustering to be observed (Figure 4.7A). The red fluorescent NB bound specifically to transfected cells that exposed EGFP on the exterior, which occurs during proper trafficking of Syx1a-EGFP. Truncated forms (SyxdNT) also was able to be surface labeled with NB (Figure 4.8H), however the SyxTMD was not trafficked properly (Figure 4.8D) and no NB fluorescence was retained. Therefore, the dynamics of Syx1a and SyxdNT were measurable as a function of Syx cluster positions.

Syx1a clusters are known to form beneath secretory vesicles after vesicles approach the plasma membrane and the formation of Syx1a clusters is essential for proper docking [24]. These clusters contain Munc18 [132], [133], which suggests that some Syx1a molecules are in a closed position within the cluster [134]. If Syx1a molecules are not recruited to the vesicle location, the vesicle only transiently interacts with the membrane [20]. Therefore, it is likely that the vesicle contains molecules that interact with Syx1a or Munc18 to establish a link(s) essential for stable docking. Since many copies (50-70) of Syx1a are within clusters [28] it is possible that many molecular links exist, allowing individual links to be weakly associated, but numerous. In our data, the motion of Syx1a was dependent upon the cluster positions and the motion of Syx was higher within the center of clusters than near a cluster (~200 nm away) or further outside of a cluster (> 0.5 µm away) (Figure 4.7H). This was unexpected, as a cluster indicates that molecules are relatively stable in their positions and some interaction is leading to the accumulation of molecules at that location. Therefore, we altered the protein via cleavage of the N-terminal Habc domain (Figure 4.8), depleted cholesterol (Figure 4.9), a known component of Syx1a clusters, and developed a dynamics model to further explain the findings.

The Habc of Syx1a is required for proper targeting of Syx clusters to docked granules in PC12 [22] and INS-1 cells [28]. This likely takes place through Munc18, where Munc18 binds the Habc domain [135], facilitates VAMP2 interactions [136] and promotes fusion in vitro. By removing the Habc domain, Munc18 is likely no longer bound as strongly to Syx1a [137]. Munc18 acts to chaperone Syx1a to the membrane [24], [99] and we observe a slight retention of SyxdNT within the cell in confocal imaging (Figure 4.8C). Binding between the Habc domain and Munc18 is also thought to keep Syx in a “closed” state reducing the exposure of the SNARE domain [136], possibly to aid in the regulation of SNARE complex formation. By removing the Habc domain, the mobility of Syx was no longer dependent on the distance to a cluster (Figure 4.8H). There is no significant difference between the mobility of SyxdNT molecules at the center of clusters (Figure 4.8H) when compared to other locations on the cell surface, suggesting that the Habc domain either aids in mobility within cluster by protecting the SNARE domain or the Habc aids in proper targeting which indirectly affects the mobility. The removal of the Habc could directly expose the SNARE motif, allowing more SNARE-SNARE interactions with other Syx molecules [23], [28] and this could decrease mobility at clusters.

Although protein-protein interactions play a key role in Syx cluster formation [28], the membrane environment also likely affects the dynamics. Syx clusters contain cholesterol [30] and cholesterol is essential for maintaining fluid cell membranes [138]. Even in simple membranes (POPC liposomes) increased cholesterol concentration led to clustering of Syx1a, in contrast to the initially observed dispersed Syx1 molecules [35]. Radiolabeling experiments showed that Syx1a is in direct contact with cholesterol [30] and cell fractionation assays show that SNARE proteins are contained in cholesterol-rich lipid rafts [139]. Cholesterol is a key component in cell membranes and makes up 35% of the plasma membrane lipids and Syx clusters are enriched in cholesterol relative to the rest of the plasma membrane, thus of the clusters likely contain even more cholesterol. Therefore, we hypothesized that cholesterol maintained the enhanced mobility observed at the center of clusters (Figure 4.7H). By sequestering cholesterol, the mobility of Syx was dramatically decreased throughout the cell (Figure 4.10), suggesting that cholesterol is needed for mobility within clusters and elsewhere.

Interestingly, the motion of molecules near the cluster decreased the most, with mobility at the cluster the lowest and an increasing trend the further away from the cluster center (Figure 4.9H). With cholesterol depletion from the plasma membrane using MBCD and known cholesterol enrichment at clusters, it is possible the reduced mobility is due to a change in the local membrane environment at the site of cluster. Cholesterol can alter membrane shape and thickness. Cholesterol can also affect the cytoskeleton and could play a role in the corralling of Syx molecules during cluster formation, as the effects of cholesterol depletion on protein dynamics is challenging to interpret through simple changes in the diffusion coefficient [140].

Despite depleting cholesterol, clusters remained present in PC12 cells (Figure 4.9B). Others have shown that the reduction of cholesterol reduces the clustering of Syx in PC12 membrane sheets [30]. In our work, clusters were still clearly observed in most cells (Figure 4.9B), however the cells were reduced in size. The presence of clusters post-depletion of cholesterol here suggests that Syx molecules are either still corralled or homo-oligimerize, as others have suggested or enough cholesterol remains present post MBCD treatment to retain clusters in live PC12 cells.

4.2.5 Conclusion

In this work we looked at single molecule mobility of Syx 1A with respect to cluster distance and saw a drastic increase of mobility at the center of the cluster (Figure 4.7). Looking at a truncated Syx1A construct, dNT, we observed slight flattening of the trend, possibly due to non-specific clustering of the molecules (Figure 4.8). Finally, removing cholesterol prevented mobility at the center of the cluster and lowered single molecule mobility throughout the cells (Figure 4.9). It is likely that local cholesterol content at cluster locations is vital to keeping clusters dynamic.

Chapter Five: Multivesicular Endosome Membrane Fusion and Future Work

SNARE proteins and Syx1a clusters, specifically, are locations of membrane fusion. Although this is clearly established and well-characterized in neuroendocrine cells, where Ca^{2+} stimulates secretion and the process is highly regulated, less is known about the role of SNARE proteins in constitutive membrane fusion. In this chapter, the constitutive membrane fusion of multi-vesicular endosomes (MVEs) and the colocalization of MVEs has been measured with respect to Syntaxin proteins (Syx1, Syx3, Syx4) in a model cell line (A549 and PC12). In the MVE fusion process, exosomes are released from cells and travel to other cells to pass on biomolecules that can affect other cells. Exosome secretion is highly upregulated in cancer cells, which is why A549 (a lung cancer cell line) was chosen. Here, I present a method for measuring protein recruitment during MVE membrane fusion to identify which proteins are involved in the process and show the preliminary results for Syx4. The background work has been accepted for publication in a review article [141], methods to analyze the data is under review, and the work on Syx proteins in the process is preliminary and unpublished.

5.1 Introduction: MVEs secrete exosomes

Exosomes are small vesicles that are secreted from cells, can signal to cells, and can be taken up by cells. Exosome biogenesis begins with the inward budding of an endosomal membrane to form intraluminal vesicles (ILVs, Figure 5.1). These ILVs contain cargo sorted from the cytoplasm and endosomal membrane and carry signatures of the cell, such as mRNAs, microRNAs, lipids, cytokines, transmembrane receptors, growth and transcription factors [142]. Multivesicular endosomes (MVEs) are known to fuse with lysosomes for ILV cargo degradation [143] (Figure 5.1, green arrow), but fusion with the plasma membrane and the release of exosomes from the cell was first proposed in 1974 [144] then demonstrated in 1983 [145], [146]. To release exosomes, MVEs are directed to the plasma membrane where they dock and fuse (Figure 5.1, blue arrows). The ILVs are then secreted and the term "exosome" is used to describe the now extracellular vesicles. After MVE fusion, exosomes can remain associated with the source cell, suggesting there is an additional step for environmental release dependent on molecules that adhere or tether exosomes to the cell surface (Figure 5.1, purple). Exosomes can thereby be regulated to have local interactions or diffuse away to interact with distant cells. Thus, exosomes release can convey cellular material for signaling or uptake which can affect health and cellular function [143], [147]–[152].

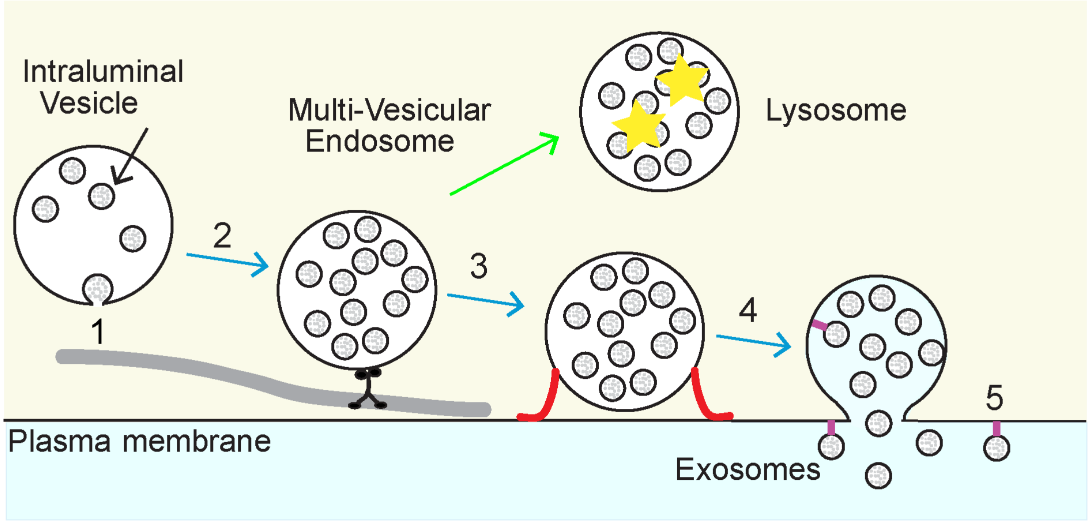

Figure 5.1 Five Stages of Exosome Secretion The exosome secretion process begins when 1) an endosome invaginates to form intraluminal vesicles (ILVs) making a multivesicular endosome (MVE). The MVE can then either fuse with lysosomes (green arrow) for cargo degradation by lysosomal enzymes (yellow stars) or 2) traffic to the plasma membrane to 3) dock and 4) fuse with the plasma membrane (blue arrows). This releases exosomes into the extracellular space, but many remain attached to the plasma membrane via tethering molecules (purple), limiting them to local interactions. 5) Once they detach from the cell, exosomes can diffuse away and be taken up by distant cells. [141]

For direct imaging of MVE fusion, two components are needed – a protein that is enriched on ILVs and a pH sensitive fluorophore. CD63 is a 4-pass transmembrane protein enriched on ILVs [153], [154], but not localized solely to ILVs [155]. Several labs have focused on CD63 as a probe of choice for visualizing MVE fusion [156]–[163]. A key feature of probes used are that the pH-sensitive fluorescent proteins are located within an extracellular loop, which places the fluorophore inside the acidic MVE lumen. Indeed, 70-90% of CD63-pHluorin is contained within acidic vesicles near the surface, as measured by dequenching the pHluorin fluorophore with NH_4Cl [158]. Recent EM studies suggest that two-thirds of CD63 resides on the ILV surface and one-third remains on the limiting endosomal membrane of MVEs [164]. CD63 with an N-or C-terminal label has also been used to measure fusion, although these probes localize the pH-sensitive fluorophore to the neutral cytosol and acidic lumen of ILVs, leading to higher background fluorescence before fusion and a reduced increase in signal upon fusion [165]. Additional CD63 probes exist, including a stabilized pHluorin, red fluorescent pH-sensitive probes like pHuji, or adding a second pH-insensitive fluorophore [158], [160].

The choice of a fusion probe can make a significant difference in MVE fusion frequency. One study showed little MVE fusion in HeLa cells, with 0% of CD63+ vesicles fusing [165], whereas a similar study using in HeLa cells measured numerous fusion events (~2-3 events/minute) [158]. Signal enhancement occurs when using a probe, where pHluorin is contained within the acidic lumen of the MVE, thus reducing the background signal relative to the cytosolic EGFP present in the probe. This makes fusion events easier to identify but visualizing MVEs prior to fusion is challenging because pHluorin is completely quenched at low pH. The use of a doubly tagged CD63 – a construct that contains both pHluorin and a c-terminal mScarlet – allowed for both the enhanced fusion signal and tracking of all CD63+ possible MVEs using dual color imaging [160]. These data suggest that probe to probe variations in the quantification of exosome secretion events exist.

To determine the kinetics components of CD63-pHluorin diffusion in the plasma membrane, fluorescence recovery after photobleaching (FRAP) experiments were performed with CD63-pHluorin on the surface of A549 cells (Figure 5.2). Recovery traces (Figure 5.2B) show that CD63-pHluorin is mobile on the plasma membrane and fitting of the data, as described in methods, revealed that CD63-pHluorin moved with a diffusion coefficient of 0.039 μm^2/s (Figure 5.2D). Interestingly, there was no temperature dependence observed for the motion of CD63 on the plasma membrane (Figure 5.2).

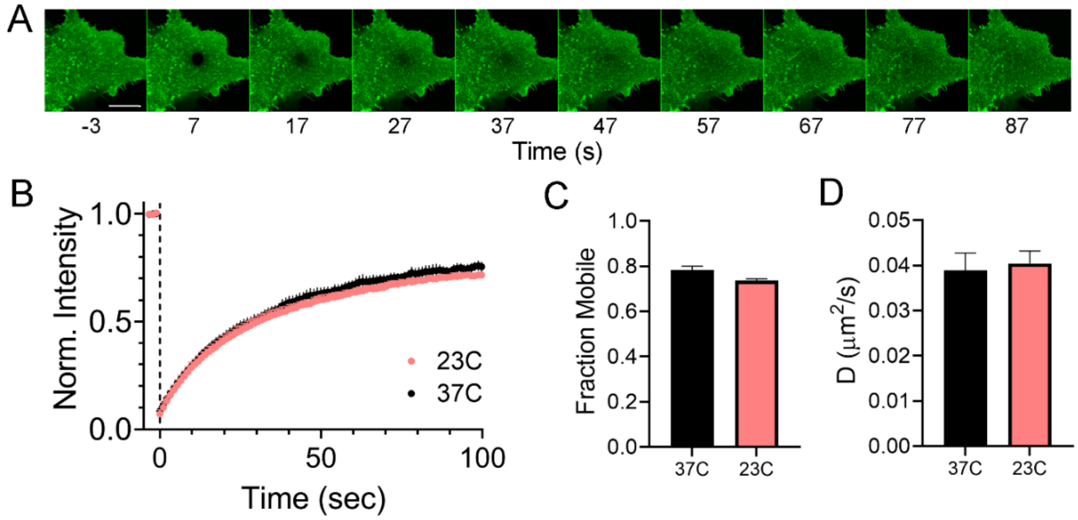

Figure 5.2 Diffusion rate of CD63-pHluorin in plasma membrane are similar at 23C and 37C. A) Montage showing photobleaching and recovery of CD63-pHluorin on plasma membrane of A549 cells. Confocal image of the bottom of the cell before photobleaching (-3s) is followed by the recovery process at intervals of 10s. Scale bar = 10 μm. B) Intensity of the bleached region in time at 23°C and 37°C (n=10 cells each). C) The mobile fraction at 23°C and 37°C. D) Diffusion coefficient for CD63 at 23°C and 37°C. Standard error is shown in all figures. There are no significant differences in plots C and D.

Colocalization Screening of Syntaxin with MVEs

To investigate which Syx molecules colocalize with MVEs, we used fluorescently labeled Syx with either EGFP or fluorescently labeled anti-myc antibodies in live PC12 cells. Here, PC12 cells were chosen because they express Syx1a. MVE locations were determined with the use of CD63-mCherry. It was seen that Syx1a, Syx3, and Syx4 all colocalize with CD63-mCh (Figure 5.3). Syx1a colocalization with neuropeptide Y(NPY) dense core vesicles was lower (ΔF/S) than Syx1a with CD63 (Figure 5.3), suggesting that more Syx1a is recruited for MVE fusion than for dense core vesicle fusion. One possibility for this is that more Syx1a is required for MVE fusion due to size of MVEs compared to dense core vesicles (up to 1 μm vs. 200 nm diameter). Colocalization was measured by first detecting vesicle locations followed by cropping of the identified region in both Syx and vesicle channels. Cropped regions are then averaged and quantified as ΔF (circle – annulus) where the annulus is a local background (Figure 5.3 B).

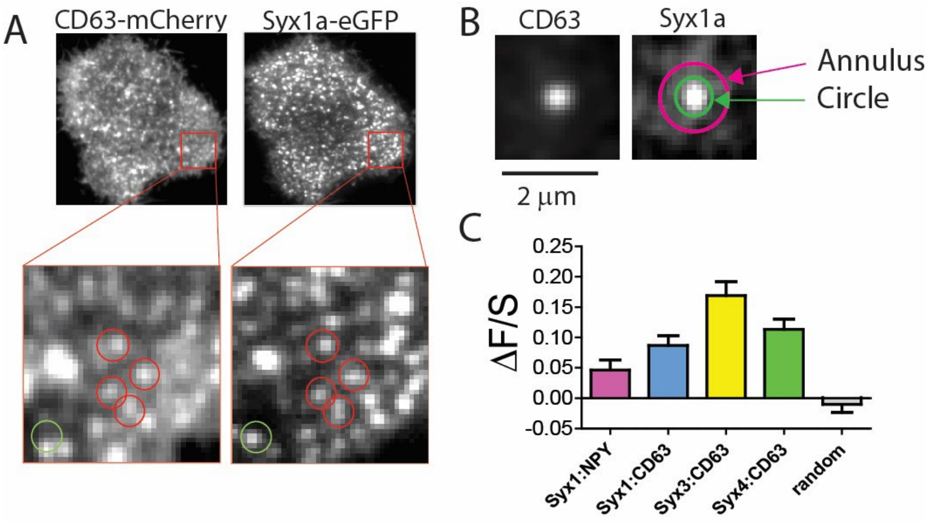

Figure 5.3: Syntaxin proteins colocalize with MVBs. A) Live PC12 cells expressing Syx1a-EGFP and CD63-mCherry (CTL) were imaged using TIRFM. An enlarged region shows that some vesicles colocalize to Syx1a clusters (red circles). B) CD63 vesicles and the corresponding Syx1a regions were cropped and averaged. The intensity within a circle – annulus (a local background), ΔF, was measured in the protein channel and then normalized for the expression level (S = annulus – background). C) Syx1a, Syx3, Syx4 were screened for colocalization and all show colocalization ($p<0.05$ for all when compared to the control, where the regions were randomly selected).

The role of Syntaxin 4 during MVE fusion

This colocalization and the fact that KO of Syx4 blocks exosome secretion in A549 or HeLa cells [158] led us to screen if Syx4 is present during fusion. In order to study interactions of MVEs with Syntaxins, we used CD63 pHlourin co-expressed with Syx4-myc and used a red fluorescent anti-myc antibody to probe locations of Syx4 during fusion. This myc tagged Syx was used so that only Syx4 on the plasma membrane and not Syx4 on the MVE surface would be labeled. The fusion average fusion events show a decrease of Syx4 at the location of fusion after fusion (Figure 5.4 E) while there is a downward trend in the non-fusing vesicle channel.

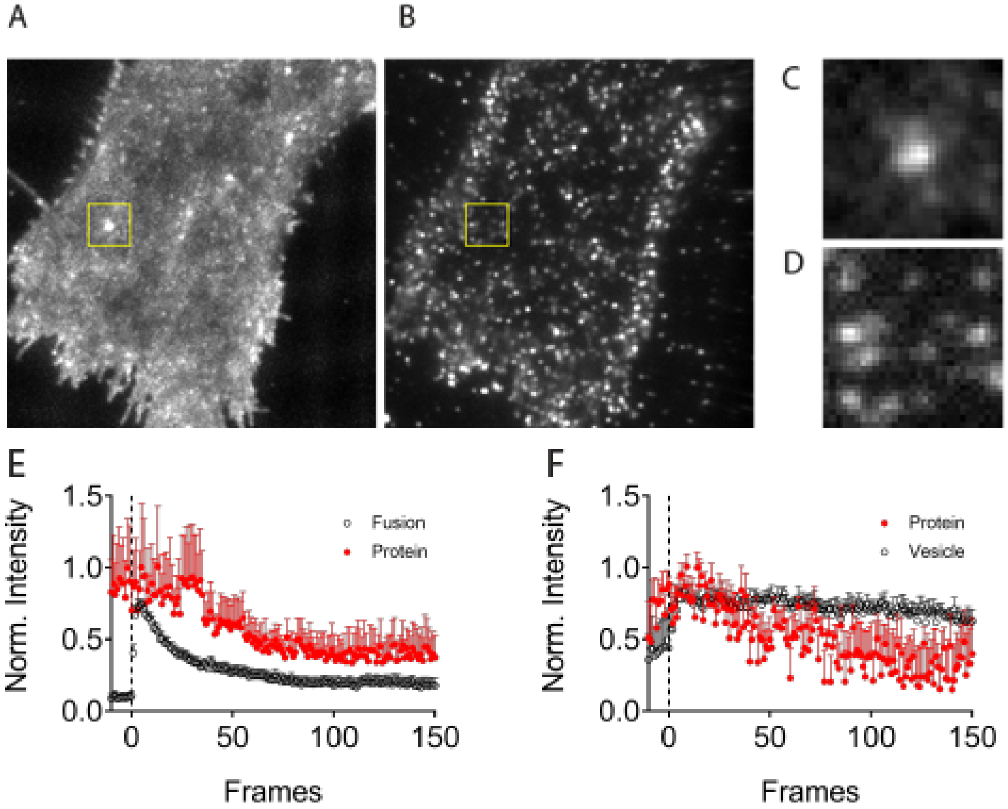

Figure 5.4 CD63-pHlourin co-expressed with Syx4 myc in A549 cells. A) A max intensity projection of CD63-pHluorin in order to show locations of fusion. B) Average image of Syx4 tagged with anti-myc antibody labeled with AF594. C) Average image of a cropped fusion event, shown by the yellow square in A, with 10 frames flanking the event

frame. D) Cropped and averaged Syx4 channel of the same location and frames. E) average time trace of the fusion events and the respective protein channel containing Syx4. F) time trace of moving vesicles and the associated protein channel.

Fluorescence Recovery After Photobleaching (FRAP)

FRAP was performed on A549 cells expressing CD63-pHluorin using an Olympus Fluoview 3000. Cells expressing CD63 on the plasma membrane were selected and a 1.99 µm radius spot was bleached using the tornado raster setting. Three images were collected prior to bleaching and images were collected for a total of 100 frames by taking one frame every 1.085s. The rate of recovery was fit, as described previously, to determine the diffusion coefficient of CD63 on the plasma membrane and the fraction mobile [65]. FRAP was performed at 23°C and 37°C.

Conclusions and Future work.

The study of MVE fusion is still relatively new and the components involved is unknown. Identification of Syntaxin that are involved in MVE fusionwould have impact on the field and possibly offer targets to interfere with the MVE fusion process, which is upregulated in a number of disease states. Additionally, the role of Syx clustering and cholesterol could be studied further to determine if this is analogous to stimulated exocytosis in secretory cells.

The experiments described here are preliminary and look at kinetics of the MVE marker CD63 along with colocalization experiments with various Syx molecules, suggesting their roles in MVE fusion in PC12 cells. Intensity traces of CD63 and a protein of interest at fusion events describe the accumulation and dispersion of proteins at the fusion site, signifying the involvement of these proteins with fusion. Similar colocalization experiments could be performed in A549 cells, along with fusion/intensity traces of proteins during fusion. Further experiments could involve the use inducing fusion with drugs such as ionomycin or depletion of cholesterol with MBCD could identify the roles of Ca2+ and the lipid environment in the process.

Processing of fusion events is a non-trivial process with identification of fusion events and alignment in time with respect to fusion occurring being the most challenging aspects. Further work could be done to refine processing and quantification of events along with characterization of events. The field of MVE fusion events is still young and could greatly benefit from screening experiments such as the ones previously described in this work.

References

[1] R. Phillips, J. Kondev, J. Theriot, H. G. Garcia, and N. Orme, “Physical Biology of the Cell,” *Physical Biology of the Cell*. 2012, doi: 10.1201/9781134111589.

[2] E. A. Cino and D. P. Tieleman, “Curvature-based sorting of eight lipid types in asymmetric buckled plasma membrane models,” *Biophys. J.*, vol. 121, no. 11, pp. 2060–2068, 2022, doi: 10.1016/j.bpj.2022.05.002.

[3] A. Callan-Jones, B. Sorre, and P. Bassereau, “Curvature-driven lipid sorting in biomembranes,” *Cold Spring Harb. Perspect. Biol.*, vol. 3, no. 2, pp. 1–14, 2011, doi: 10.1101/cshperspect.a004648.

[4] A. Tian and T. Baumgart, “Sorting of lipids and proteins in membrane curvature gradients,” *Biophys. J.*, vol. 96, no. 7, pp. 2676–2688, 2009, doi: 10.1016/j.bpj.2008.11.067.

[5] H. Strahl, S. Ronneau, B. S. González, D. Klutsch, C. Schaffner-Barbero, and L. W. Hamoen, “Transmembrane protein sorting driven by membrane curvature,” *Nat. Commun.*, vol. 6, 2015, doi: 10.1038/ncomms9728.

[6] S. G. Ostrowski, C. T. Van Bell, N. Winograd, and A. G. Ewing, “Mass spectrometric imaging of highly curved membranes during Tetrahymena mating.,” *Science*, vol. 305, no. 5680, pp. 71–73, Jul. 2004, doi: 10.1126/science.1099791.

[7] A. Roux, D. Cuvelier, P. Nassoy, J. Prost, P. Bassereau, and B. Goud, “Role of curvature and phase transition in lipid sorting and fission of membrane tubules,” *EMBO J.*, vol. 24, no. 8, pp. 1537–1545, 2005, doi: 10.1038/sj.emboj.7600631.

[8] M. A. Zhukovsky, A. Filograna, A. Luini, D. Corda, and C. Valente, “Phosphatidic acid in membrane rearrangements,” *FEBS Lett.*, vol. 593, no. 17, pp. 2428–2451,

2019, doi: 10.1002/1873-3468.13563.

[9] B. Antonny, “Membrane deformation by protein coats,” *Curr. Opin. Cell Biol.*, vol. 18, no. 4, pp. 386–394, 2006, doi: 10.1016/j.ceb.2006.06.003.

[10] R. Jin, R. Cao, and T. Baumgart, “Curvature dependence of BAR protein membrane association and dissociation kinetics,” *Sci. Rep.*, vol. 12, no. 1, pp. 1–9, 2022, doi: 10.1038/s41598-022-11221-9.

[11] M. B. Jensen *et al.*, “Membrane curvature sensing by amphipathic helices: A single liposome study using α-synuclein and annexin B12,” *J. Biol. Chem.*, vol. 286, no. 49, pp. 42603–42614, 2011, doi: 10.1074/jbc.M111.271130.

[12] B. Antonny, “Mechanisms of membrane curvature sensing,” *Annu. Rev. Biochem.*, vol. 80, pp. 101–123, 2011, doi: 10.1146/annurev-biochem-052809-155121.

[13] M. Kamal and R. Jockers, “Biological significance of GPCR heteromerization in the neuro-endocrine system,” *Front. Endocrinol. (Lausanne).*, vol. 2, no. FEB, pp. 1–14, 2010, doi: 10.3389/fendo.2011.00002.

[14] P. Pfeiffer, A. V. Egorov, F. Lorenz, J. H. Schleimer, A. Draguhn, and S. Schreiber, “Clusters of cooperative ion channels enable a membrane-potential-based mechanism for short-term memory,” *Elife*, vol. 9, pp. 1–27, 2020, doi: 10.7554/eLife.49974.

[15] A. Jha, T. S. van Zanten, J. M. Philippe, S. Mayor, and T. Lecuit, “Quantitative Control of GPCR Organization and Signaling by Endocytosis in Epithelial Morphogenesis,” *Curr. Biol.*, vol. 28, no. 10, pp. 1570-1584.e6, 2018, doi: 10.1016/j.cub.2018.03.068.

[16] S. Barg, M. K. Knowles, X. Chen, M. Midorikawa, and W. Almers, “Syntaxin

clusters assemble reversibly at sites of secretory granules in live cells," *Proc. Natl. Acad. Sci. U. S. A.*, vol. 107, no. 48, pp. 20804–20809, 2010, doi: 10.1073/pnas.1014823107.

[17] G. van den Bogaart, T. Lang, and R. Jahn, *Microdomains of SNARE proteins in the plasma membrane*, 1st ed., vol. 72. Elsevier Inc., 2013.

[18] E. Merklinger *et al.*, "The packing density of a supramolecular membrane protein cluster is controlled by cytoplasmic interactions," *Elife*, vol. 6, pp. 1–18, 2017, doi: 10.7554/eLife.20705.

[19] A. Honigmann *et al.*, "Phosphatidylinositol 4,5-bisphosphate clusters act as molecular beacons for vesicle recruitment," *Nat. Struct. Mol. Biol.*, vol. 20, no. 6, pp. 679–686, 2013, doi: 10.1038/nsmb.2570.

[20] N. R. Gandasi and S. Barg, "Contact-induced clustering of syntaxin and munc18 docks secretory granules at the exocytosis site.," *Nat. Commun.*, vol. 5, p. 3914, May 2014, doi: 10.1038/ncomms4914.

[21] C. B. Gundersen, "A membrane-fusion model that exploits a β-to-α transition in the hydrophobic domains of syntaxin 1A and synaptobrevin 2," *Int. J. Mol. Sci.*, vol. 18, no. 7, 2017, doi: 10.3390/ijms18071582.

[22] M. K. Knowles, S. Barg, L. Wan, M. Midorikawa, X. Chen, and W. Almers, "Single secretory granules of live cells recruit syntaxin-1 and synaptosomal associated protein 25 (SNAP-25) in large copy numbers," *Proc. Natl. Acad. Sci. U. S. A.*, vol. 107, no. 48, pp. 20810–20815, 2010, doi: 10.1073/pnas.1014840107.

[23] J. J. Sieber *et al.*, "Anatomy and dynamics of a supramolecular membrane protein cluster," *Science (80-.).*, vol. 317, no. 5841, pp. 1072–1076, 2007, doi:

10.1126/science.1141727.

[24] N. R. Gandasi and S. Barg, "Contact-induced clustering of syntaxin and munc18 docks secretory granules at the exocytosis site," *Nat. Commun.*, vol. 5, no. May, pp. 1–14, 2014, doi: 10.1038/ncomms4914.

[25] I. Fernandez, J. Ubach, I. Dulubova, X. Zhang, T. C. Südhof, and J. Rizo, "Three-dimensional structure of an evolutionarily conserved N-terminal domain of syntaxin 1A," *Cell*, vol. 94, no. 6, pp. 841–849, 1998, doi: 10.1016/S0092-8674(00)81742-0.

[26] R. B. Sutton, D. Fasshauer, R. Jahn, and A. T. Brunger, "Crystal structure of a SNARE complex involved in synaptic exocytosis at 2.4 Å resolution," *Nature*, vol. 395, no. 6700, pp. 347–353, 1998, doi: 10.1038/26412.

[27] D. Fasshauer, R. B. Sutton, A. T. Brunger, and R. Jahn, "Conserved structural features of the synaptic fusion complex: SNARE proteins reclassified as Q-and R-SNAREs (membrane fusionneurotransmissionclostridial neurotoxins)," *Neurobiol. Commun. by Peter B. Moore*, vol. 95, no. December, pp. 15781–15786, 1998.

[28] J. J. Sieber, K. I. Willig, R. Heintzmann, S. W. Hell, and T. Lang, "The SNARE motif is essential for the formation of syntaxin clusters in the plasma membrane," *Biophys. J.*, vol. 90, no. 8, pp. 2843–2851, 2006, doi: 10.1529/biophysj.105.079574.

[29] B. Liang, V. Kiessling, and L. K. Tamm, "Prefusion structure of syntaxin-1A suggests pathway for folding into neuronal trans-SNARE complex fusion intermediate," *Proc. Natl. Acad. Sci. U. S. A.*, vol. 110, no. 48, pp. 19384–19389, 2013, doi: 10.1073/pnas.1314699110.

[30] T. Lang *et al.*, “SNAREs are concentrated in cholesterol-dependent clusters that define docking and fusion sites for exocytosis,” *EMBO J.*, vol. 20, no. 9, pp. 2202–2213, 2001, doi: 10.1093/emboj/20.9.2202.

[31] J. C. Lerman, J. Robblee, R. Fairman, and F. M. Hughson, “Structural analysis of the neuronal SNARE protein syntaxin-1A,” *Biochemistry*, vol. 39, no. 29, pp. 8470–8479, 2000, doi: 10.1021/bi0003994.

[32] R. Laage, J. Rohde, B. Brosig, and D. Langosch, “A conserved membrane-spanning amino acid motif drives homomeric and supports heteromeric assembly of presynaptic SNARE proteins,” *J. Biol. Chem.*, vol. 275, no. 23, pp. 17481–17487, 2000, doi: 10.1074/jbc.M910092199.

[33] S. Sharma and M. Lindau, “T-SNARE Transmembrane Domain Clustering Modulates Lipid Organization and Membrane Curvature,” *J. Am. Chem. Soc.*, vol. 139, no. 51, pp. 18440–18443, 2017, doi: 10.1021/jacs.7b10677.

[34] M. B. Stone, S. A. Shelby, M. F. Nńñez, K. Wisser, and S. L. Veatch, “Protein sorting by lipid phase-like domains supports emergent signaling function in b lymphocyte plasma membranes,” *Elife*, vol. 6, pp. 1–33, 2017, doi: 10.7554/eLife.19891.

[35] D. H. Murray and L. K. Tamm, “Clustering of syntaxin-1A in model membranes is modulated by phosphatidylinositol 4,5-bisphosphate and cholesterol.,” *Biochemistry*, vol. 48, no. 21, pp. 4617–4625, Jun. 2009, doi: 10.1021/bi9003217.

[36] A. Y. Zhang, F. Yi, G. Zhang, E. Gulbins, and P. L. Li, “Lipid raft clustering and redox signaling platform formation in coronary arterial endothelial cells,” *Hypertension*, vol. 47, no. 1, pp. 74–80, 2006, doi:

10.1161/10.1161/01.HYP.0000196727.53300.62.

[37] L. G. Magal *et al.*, "Clustering and lateral concentration of raft lipids by the MAL protein.," *Mol. Biol. Cell*, vol. 20, no. 16, pp. 3751–3762, Aug. 2009, doi: 10.1091/mbc.e09-02-0142.

[38] C. A. Combs, "Fluorescence microscopy: A concise guide to current imaging methods," *Curr. Protoc. Neurosci.*, no. SUPPL.50, pp. 1–19, 2010, doi: 10.1002/0471142301.ns0205s00.

[39] M. J. Sanderson, I. Smith, I. Parker, and M. D. Bootman, "Cold Spring Harb Protoc," *Physiol. Behav.*, vol. 2014, no. 10, pp. 1–36, 2016, doi: 10.1101/pdb.top071795.Fluorescence.

[40] K. W. Dunn, M. M. Kamocka, and J. H. McDonald, "A practical guide to evaluating colocalization in biological microscopy.," *Am. J. Physiol. Cell Physiol.*, vol. 300, no. 4, pp. C723-42, Apr. 2011, doi: 10.1152/ajpcell.00462.2010.

[41] R. Devkota and M. Pilon, "FRAP: A Powerful Method to Evaluate Membrane Fluidity in Caenorhabditis elegans," *Bio-Protocol*, vol. 8, no. 13, pp. 1–8, 2018, doi: 10.21769/bioprotoc.2913.

[42] R. B. Sekar and A. Periasamy, "Fluorescence resonance energy transfer (FRET) microscopy imaging of live cell protein localizations," *J. Cell Biol.*, vol. 160, no. 5, pp. 629–633, 2003, doi: 10.1083/jcb.200210140.

[43] D. Axelrod, D. E. Koppel, J. Schlessinger, E. Elson, and W. W. Webb, "Mobility measurement by analysis of fluorescence photobleaching recovery kinetics," *Biophys. J.*, vol. 16, no. 9, pp. 1055–1069, 1976, doi: 10.1016/S0006-3495(76)85755-4.

[44] J. Lippincott-Schwartz, E. L. Snapp, and R. D. Phair, "The Development and Enhancement of FRAP as a Key Tool for Investigating Protein Dynamics," *Biophys. J.*, vol. 115, no. 7, pp. 1146–1155, 2018, doi: 10.1016/j.bpj.2018.08.007.

[45] K. N. Fish, "Total internal reflection fluorescence (TIRF) microscopy.," *Curr. Protoc. Cytom.*, vol. Chapter 12, p. Unit12.18, Oct. 2009, doi: 10.1002/0471142956.cy1218s50.

[46] D. Axelrod, T. P. Burghardt, and N. L. Thompson, "Total internal reflection fluorescence.," *Annu. Rev. Biophys. Bioeng.*, vol. 13, no. 17, pp. 247–268, 1984, doi: 10.1146/annurev.bb.13.060184.001335.

[47] M. L. Martin-Fernandez and D. T. Clarke, "Single molecule fluorescence detection and tracking in mammalian cells: The state-of-the-art and future perspectives," *Int. J. Mol. Sci.*, vol. 13, no. 11, pp. 14742–14765, 2012, doi: 10.3390/ijms131114742.

[48] C. Liu, Y.-L. Liu, E. P. Perillo, A. K. Dunn, and H.-C. Yeh, "Single-Molecule Tracking and Its Application in Biomolecular Binding Detection.," *IEEE J. Sel. Top. quantum Electron. a Publ. IEEE Lasers Electro-optics Soc.*, vol. 22, no. 4, 2016, doi: 10.1109/JSTQE.2016.2568160.

[49] H. Shen *et al.*, "Single Particle Tracking: From Theory to Biophysical Applications," *Chem. Rev.*, vol. 117, no. 11, pp. 7331–7376, Jun. 2017, doi: 10.1021/acs.chemrev.6b00815.

[50] C. Manzo and M. F. Garcia-Parajo, "A review of progress in single particle tracking: from methods to biophysical insights," *Reports Prog. Phys.*, vol. 78, no. 12, p. 124601, 2015, doi: 10.1088/0034-4885/78/12/124601.

[51] L. Daniel and S. Kai, "Lipid Rafts As a Membrane-Organizing Principle," *Science*

(80-.)., vol. 327, no. 5961, pp. 46–50, Jan. 2010, doi: 10.1126/science.1174621.

[52] A. D. Douglass and R. D. Vale, “Single-molecule microscopy reveals plasma membrane microdomains created by protein-protein networks that exclude or trap signaling molecules in T cells.,” *Cell*, vol. 121, no. 6, pp. 937–950, Jun. 2005, doi: 10.1016/j.cell.2005.04.009.

[53] T. Zech *et al.*, “Accumulation of raft lipids in T-cell plasma membrane domains engaged in TCR signalling.,” *EMBO J.*, vol. 28, no. 5, pp. 466–476, Mar. 2009, doi: 10.1038/emboj.2009.6.

[54] K. C. Taylor and C. R. Sanders, “Regulation of KCNQ/Kv7 family voltage-gated K(+) channels by lipids.,” *Biochim. Biophys. acta. Biomembr.*, vol. 1859, no. 4, pp. 586–597, Apr. 2017, doi: 10.1016/j.bbamem.2016.10.023.

[55] B. Svobodova and K. Groschner, “Mechanisms of lipid regulation and lipid gating in TRPC channels.,” *Cell Calcium*, vol. 59, no. 6, pp. 271–279, Jun. 2016, doi: 10.1016/j.ceca.2016.03.012.

[56] R. W. Klemm *et al.*, “Segregation of sphingolipids and sterols during formation of secretory vesicles at the trans-Golgi network.,” *J. Cell Biol.*, vol. 185, no. 4, pp. 601–612, May 2009, doi: 10.1083/jcb.200901145.

[57] S. Mukherjee, T. T. Soe, and F. R. Maxfield, “Endocytic sorting of lipid analogues differing solely in the chemistry of their hydrophobic tails.,” *J. Cell Biol.*, vol. 144, no. 6, pp. 1271–1284, Mar. 1999, doi: 10.1083/jcb.144.6.1271.

[58] L. K. Tamm and H. M. McConnell, “Supported phospholipid bilayers,” *Biophys. J.*, vol. 47, no. 1, pp. 105–113, 1985.

[59] C. Leidy, J. Ocampo, L. Duelund, O. G. Mouritsen, K. Jørgensen, and G. H.

Peters, “Membrane restructuring by phospholipase A2 is regulated by the presence of lipid domains.,” *Biophys. J.*, vol. 101, no. 1, pp. 90–99, Jul. 2011, doi: 10.1016/j.bpj.2011.02.062.

[60] S. L. Veatch, I. V Polozov, K. Gawrisch, and S. L. Keller, “Liquid domains in vesicles investigated by NMR and fluorescence microscopy,” *Biophys. J.*, vol. 86, no. 5, pp. 2910–2922, 2004.

[61] R. Koynova and M. Caffrey, “Phases and phase transitions of the phosphatidylcholines,” *Biochim. Biophys. Acta (BBA)-Reviews Biomembr.*, vol. 1376, no. 1, pp. 91–145, 1998.

[62] R. S. Petruzielo, F. A. Heberle, P. Drazba, J. Katsaras, and G. W. Feigenson, “Phase behavior and domain size in sphingomyelin-containing lipid bilayers,” *Biochim. Biophys. Acta (BBA)-Biomembranes*, vol. 1828, no. 4, pp. 1302–1313, 2013.

[63] F. Schmid, “Physical mechanisms of micro-and nanodomain formation in multicomponent lipid membranes,” *Biochim. Biophys. Acta (BBA)-Biomembranes*, vol. 1859, no. 4, pp. 509–528, 2017.

[64] T. Baumgart, S. T. Hess, and W. W. Webb, “Imaging coexisting fluid domains in biomembrane models coupling curvature and line tension,” *Nature*, vol. 425, no. 6960, pp. 821–824, 2003.

[65] J. C. Black, P. P. Cheney, T. Campbell, and M. K. Knowles, “Membrane curvature based lipid sorting using a nanoparticle patterned substrate,” *Soft Matter*, vol. 10, no. 12, pp. 2016–2023, 2014.

[66] M. Heinrich, A. Tian, C. Esposito, and T. Baumgart, “Dynamic sorting of lipids

and proteins in membrane tubes with a moving phase boundary," *Proc. Natl. Acad. Sci.*, vol. 107, no. 16, pp. 7208–7213, 2010.

[67] B. Sorre *et al.*, "Curvature-driven lipid sorting needs proximity to a demixing point and is aided by proteins," *Proc. Natl. Acad. Sci.*, vol. 106, no. 14, pp. 5622–5626, 2009.

[68] N. S. Hatzakis *et al.*, "How curved membranes recruit amphipathic helices and protein anchoring motifs," *Nat. Chem. Biol.*, vol. 5, no. 11, pp. 835–841, 2009.

[69] A. Tian, B. R. Capraro, C. Esposito, and T. Baumgart, "Bending stiffness depends on curvature of ternary lipid mixture tubular membranes," *Biophys. J.*, vol. 97, no. 6, pp. 1636–1646, 2009.

[70] R. Parthasarathy, C. Yu, and J. T. Groves, "Curvature-modulated phase separation in lipid bilayer membranes," *Langmuir*, vol. 22, no. 11, pp. 5095–5099, 2006.

[71] M. M. Kamal, D. Mills, M. Grzybek, and J. Howard, "Measurement of the membrane curvature preference of phospholipids reveals only weak coupling between lipid shape and leaflet curvature," *Proc. Natl. Acad. Sci.*, vol. 106, no. 52, pp. 22245–22250, 2009.

[72] B. Nuscher *et al.*, "α-Synuclein has a high affinity for packing defects in a bilayer membrane: a thermodynamics study," *J. Biol. Chem.*, vol. 279, no. 21, pp. 21966–21975, 2004.

[73] B. J. Peter *et al.*, "BAR domains as sensors of membrane curvature: the amphiphysin BAR structure," *Science (80-.).*, vol. 303, no. 5657, pp. 495–499, 2004.

[74] J.-B. Manneville *et al.*, "COPI coat assembly occurs on liquid-disordered domains

and the associated membrane deformations are limited by membrane tension," *Proc. Natl. Acad. Sci.*, vol. 105, no. 44, pp. 16946–16951, 2008.

[75] B. R. Capraro, Y. Yoon, W. Cho, and T. Baumgart, "Curvature sensing by the epsin N-terminal homology domain measured on cylindrical lipid membrane tethers," *J. Am. Chem. Soc.*, vol. 132, no. 4, pp. 1200–1201, 2010.

[76] H. Gerlach, V. Laumann, S. Martens, C. F. W. Becker, R. S. Goody, and M. Geyer, "HIV-1 Nef membrane association depends on charge, curvature, composition and sequence," *Nat. Chem. Biol.*, vol. 6, no. 1, pp. 46–53, 2010.

[77] W.-T. Hsieh *et al.*, "Curvature sorting of peripheral proteins on solid-supported wavy membranes," *Langmuir*, vol. 28, no. 35, pp. 12838–12843, 2012.

[78] B. Sorre *et al.*, "Nature of curvature coupling of amphiphysin with membranes depends on its bound density," *Proc. Natl. Acad. Sci.*, vol. 109, no. 1, pp. 173–178, 2012.

[79] P. S. Cremer and S. G. Boxer, "Formation and spreading of lipid bilayers on planar glass supports," *J. Phys. Chem. B*, vol. 103, no. 13, pp. 2554–2559, 1999.

[80] D. Axelrod, D. E. Koppel, J. Schlessinger, E. Elson, and W. W. Webb, "Mobility measurement by analysis of fluorescence photobleaching recovery kinetics," *Biophys. J.*, vol. 16, no. 9, pp. 1055–1069, 1976.

[81] A. Edelstein, N. Amodaj, K. Hoover, R. Vale, and N. Stuurman, "Computer control of microscopes using µManager," *Curr. Protoc. Mol. Biol.*, vol. 92, no. 1, pp. 14–20, 2010.

[82] "No Title." http://site.physics.georgetown.edu/matlab/.

[83] J. C. Crocker and D. G. Grier, "Methods of digital video microscopy for colloidal

studies," *J. Colloid Interface Sci.*, vol. 179, no. 1, pp. 298–310, 1996.

[84] B. T. Larson, K. A. Sochacki, J. M. Kindem, and J. W. Taraska, "Systematic spatial mapping of proteins at exocytic and endocytic structures.," *Mol. Biol. Cell*, vol. 25, no. 13, pp. 2084–2093, Jul. 2014, doi: 10.1091/mbc.E14-02-0771.

[85] N. Darnton, L. Turner, K. Breuer, and H. C. Berg, "Moving fluid with bacterial carpets," *Biophys. J.*, vol. 86, no. 3, pp. 1863–1870, 2004.

[86] J. D. Knight, M. G. Lerner, J. G. Marcano-Velázquez, R. W. Pastor, and J. J. Falke, "Single molecule diffusion of membrane-bound proteins: window into lipid contacts and bilayer dynamics," *Biophys. J.*, vol. 99, no. 9, pp. 2879–2887, 2010.

[87] E. E. Kooijman *et al.*, "Spontaneous curvature of phosphatidic acid and lysophosphatidic acid," *Biochemistry*, vol. 44, no. 6, pp. 2097–2102, 2005.

[88] "No Title." https://avantilipids.com/tech-support/physical-properties/phase-transition-temps/.

[89] A. W. Weisgerber and M. K. Knowles, "Membrane dynamics are slowed for Alexa594-labeled membrane proteins due to substrate interactions," *BBA Adv.*, vol. 1, p. 100026, 2021, doi: https://doi.org/10.1016/j.bbadva.2021.100026.

[90] G. Giannone *et al.*, "Dynamic superresolution imaging of endogenous proteins on living cells at ultra-high density," *Biophys. J.*, vol. 99, no. 4, pp. 1303–1310, 2010.

[91] C. A. Buttler *et al.*, "Single molecule fate of HIV-1 envelope reveals late-stage viral lattice incorporation," *Nat. Commun.*, vol. 9, no. 1, pp. 1–15, 2018.

[92] K. Lam and E. Tajkhorshid, "Membrane interactions of Cy3 and Cy5 fluorophores and their effects on membrane-protein dynamics," *Biophys. J.*, vol. 119, no. 1, pp. 24–34, 2020.

[93] L. D. Lavis, “Chemistry is dead. Long live chemistry!,” *Biochemistry*, vol. 56, no. 39, pp. 5165–5170, 2017.

[94] R. J. Rawle, A. M. V. Giraldo, S. G. Boxer, and P. M. Kasson, “Detecting and controlling dye effects in single-virus fusion experiments,” *Biophys. J.*, vol. 117, no. 3, pp. 445–452, 2019.

[95] L. D. Hughes, R. J. Rawle, and S. G. Boxer, “Choose your label wisely: Water-soluble fluorophores often interact with lipid bilayers,” *PLoS One*, vol. 9, no. 2, 2014, doi: 10.1371/journal.pone.0087649.

[96] N. C. Shaner, R. E. Campbell, P. A. Steinbach, B. N. G. Giepmans, A. E. Palmer, and R. Y. Tsien, “Improved monomeric red, orange and yellow fluorescent proteins derived from Discosoma sp. red fluorescent protein,” *Nat. Biotechnol.*, vol. 22, no. 12, pp. 1567–1572, 2004.

[97] D. M. Chudakov, M. V Matz, S. Lukyanov, and K. A. Lukyanov, “Fluorescent proteins and their applications in imaging living cells and tissues,” *Physiol. Rev.*, vol. 90, no. 3, pp. 1103–1163, 2010.

[98] T. W. M. De Groof, V. Bobkov, R. Heukers, and M. J. Smit, “Nanobodies: new avenues for imaging, stabilizing and modulating GPCRs,” *Mol. Cell. Endocrinol.*, vol. 484, pp. 15–24, 2019.

[99] R. Kasula *et al.*, “The Munc18-1 domain 3a hinge-loop controls syntaxin-1A nanodomain assembly and engagement with the SNARE complex during secretory vesicle priming,” *J. Cell Biol.*, vol. 214, no. 7, 2016, doi: 10.1083/jcb.201508118.

[100] K. J. Seitz and S. O. Rizzoli, “GFP nanobodies reveal recently-exocytosed pHluorin molecules,” *Sci. Rep.*, vol. 9, no. 1, pp. 1–10, 2019.

[101] L. C. Zanetti-Domingues, M. L. Martin-Fernandez, S. R. Needham, D. J. Rolfe, and D. T. Clarke, “A Systematic Investigation of Differential Effects of Cell Culture Substrates on the Extent of Artifacts in Single-Molecule Tracking,” *PLoS One*, vol. 7, no. 9, 2012, doi: 10.1371/journal.pone.0045655.

[102] L. C. Zanetti-Domingues, C. J. Tynan, D. J. Rolfe, D. T. Clarke, and M. Martin-Fernandez, “Hydrophobic Fluorescent Probes Introduce Artifacts into Single Molecule Tracking Experiments Due to Non-Specific Binding,” *PLoS One*, vol. 8, no. 9, 2013, doi: 10.1371/journal.pone.0074200.

[103] A. Orlowska *et al.*, “The effect of coatings and nerve growth factor on attachment and differentiation of Pheochromocytoma Cells,” *Materials (Basel).*, vol. 11, no. 1, pp. 1–10, 2017, doi: 10.3390/ma11010060.

[104] H. Bachman, J. Nicosia, M. Dysart, and T. H. Barker, “Utilizing fibronectin integrin-binding specificity to control cellular responses,” *Adv. wound care*, vol. 4, no. 8, pp. 501–511, 2015.

[105] K. J. Tomaselli, C. H. Damsky, and L. F. Reichardt, “Interactions of a neuronal cell line (PC12) with laminin, collagen IV, and fibronectin: Identification of integrin-related glycoproteins involved in attachment and process outgrowth,” *J. Cell Biol.*, vol. 105, no. 5, pp. 2347–2358, 1987, doi: 10.1083/jcb.105.5.2347.

[106] N. Chada, K. P. Sigdel, R. R. Sanganna Gari, T. R. Matin, L. L. Randall, and G. M. King, “Glass is a Viable Substrate for Precision Force Microscopy of Membrane Proteins,” *Sci. Rep.*, vol. 5, pp. 1–8, 2015, doi: 10.1038/srep12550.

[107] P. P. Cheney, M. D. Stachler, and M. K. Knowles, “Single molecule tracking of P-glycoprotein in live cells reveals dynamic heterogeneity,” in *2012 Annual*

International Conference of the IEEE Engineering in Medicine and Biology Society, 2012, pp. 3159–3162.

[108] P. P. Cheney, A. W. Weisgerber, A. M. Feuerbach, and M. K. Knowles, “Single lipid molecule dynamics on supported lipid bilayers with membrane curvature,” *Membranes (Basel).*, vol. 7, no. 1, pp. 1–13, 2017, doi: 10.3390/membranes7010015.

[109] E. Pigorsch, A. Elhaddaoui, and S. Turrell, “Studies of the binding mechanism of Congo red to poly(L-lysine) by absorption and circular dichroism spectroscopy,” *J. Mol. Struct.*, vol. 348, pp. 61–64, 1995, doi: 10.1016/0022-2860(95)08589-N.

[110] L. Guo, J. Y. Har, J. Sankaran, Y. Hong, B. Kannan, and T. Wohland, “Molecular diffusion measurement in lipid bilayers over wide concentration ranges: a comparative study,” *ChemPhysChem*, vol. 9, no. 5, pp. 721–728, 2008.

[111] M.-L. I. E. Harwardt, M. S. Dietz, M. Heilemann, and T. Wohland, “SPT and imaging FCS provide complementary information on the dynamics of plasma membrane molecules,” *Biophys. J.*, vol. 114, no. 10, pp. 2432–2443, 2018.

[112] R. Akeson and S. L. Warren, “PC12 adhesion and neurite formation on selected substrates are inhibited by some glycosaminoglycans and a fibronectin-derived tetrapeptide,” *Exp. Cell Res.*, vol. 162, no. 2, pp. 347–362, 1986.

[113] S. Johansson, L. Kjellén, M. Höök, and R. Timpl, “Substrate adhesion of rat hepatocytes: a comparison of laminin and fibronectin as attachment proteins.,” *J. Cell Biol.*, vol. 90, no. 1, pp. 260–264, 1981.

[114] B. Hua *et al.*, “An improved surface passivation method for single-molecule studies,” *Nat. Methods*, vol. 11, no. 12, pp. 1233–1236, 2014.

[115] N. C. Hartman and J. T. Groves, “Signaling clusters in the cell membrane.,” *Curr. Opin. Cell Biol.*, vol. 23, no. 4, pp. 370–376, Aug. 2011, doi: 10.1016/j.ceb.2011.05.003.

[116] K. S. Vrenken, K. Jalink, F. N. van Leeuwen, and J. Middelbeek, “Beyond ion-conduction: Channel-dependent and -independent roles of TRP channels during development and tissue homeostasis,” *Biochim. Biophys. Acta - Mol. Cell Res.*, vol. 1863, no. 6, Part B, pp. 1436–1446, 2016, doi: https://doi.org/10.1016/j.bbamcr.2015.11.008.

[117] D. Milovanovic and R. Jahn, “Organization and dynamics of SNARE proteins in the presynaptic membrane,” *Front. Physiol.*, vol. 6, no. MAR, pp. 1–11, 2015, doi: 10.3389/fphys.2015.00089.

[118] P. A. Thomason, P. M. Wolanin, and J. B. Stock, “Signal Transduction: Receptor Clusters as Information Processing Arrays,” *Curr. Biol.*, vol. 12, no. 11, pp. R399–R401, 2002, doi: https://doi.org/10.1016/S0960-9822(02)00885-0.

[119] A. J. B. Kreutzberger *et al.*, “In vitro fusion of single synaptic and dense core vesicles reproduces key physiological properties.,” *Nat. Commun.*, vol. 10, no. 1, p. 3904, Aug. 2019, doi: 10.1038/s41467-019-11873-8.

[120] G. van den Bogaart and R. Jahn, “Counting the SNAREs needed for membrane fusion,” *J. Mol. Cell Biol.*, vol. 3, no. 4, pp. 204–205, Aug. 2011, doi: 10.1093/jmcb/mjr004.

[121] P. Yin, N. R. Gandasi, S. Arora, M. Omar-Hmeadi, J. Saras, and S. Barg, “Syntaxin clusters at secretory granules in a munc18-bound conformation,” *Mol. Biol. Cell*, vol. 29, no. 22, pp. 2700–2708, 2018, doi: 10.1091/mbc.E17-09-0541.

[122] J. Kwik, S. Boyle, D. Fooksman, L. Margolis, M. P. Sheetz, and M. Edidin, “Membrane cholesterol, lateral mobility, and the phosphatidylinositol 4,5-bisphosphate-dependent organization of cell actin.,” *Proc. Natl. Acad. Sci. U. S. A.*, vol. 100, no. 24, pp. 13964–13969, Nov. 2003, doi: 10.1073/pnas.2336102100.

[123] J. Zhang, R. Xue, W.-Y. Ong, and P. Chen, “Roles of cholesterol in vesicle fusion and motion.,” *Biophys. J.*, vol. 97, no. 5, pp. 1371–1380, Sep. 2009, doi: 10.1016/j.bpj.2009.06.025.

[124] J. Pan, T. T. Mills, S. Tristram-Nagle, and J. F. Nagle, “Cholesterol perturbs lipid bilayers nonuniversally.,” *Phys. Rev. Lett.*, vol. 100, no. 19, p. 198103, May 2008, doi: 10.1103/PhysRevLett.100.198103.

[125] S.-T. Yang, A. J. B. Kreutzberger, J. Lee, V. Kiessling, and L. K. Tamm, “The role of cholesterol in membrane fusion.,” *Chem. Phys. Lipids*, vol. 199, pp. 136–143, Sep. 2016, doi: 10.1016/j.chemphyslip.2016.05.003.

[126] D. H. Murray and L. K. Tamm, “Molecular mechanism of cholesterol- and polyphosphoinositide-mediated syntaxin clustering.,” *Biochemistry*, vol. 50, no. 42, pp. 9014–9022, Oct. 2011, doi: 10.1021/bi201307u.

[127] M. Omar-Hmeadi, N. R. Gandasi, and S. Barg, “PtdIns(4,5)P 2 is not required for secretory granule docking,” *Traffic*, vol. 19, no. 6, pp. 436–445, 2018, doi: 10.1111/tra.12562.

[128] Y. B. Johari, A. C. Mercer, Y. Liu, A. J. Brown, and D. C. James, “Design of synthetic promoters for controlled expression of therapeutic genes in retinal pigment epithelial cells,” *Biotechnol. Bioeng.*, vol. 118, no. 5, pp. 2001–2015, May 2021, doi: https://doi.org/10.1002/bit.27713.

[129] J. Ries, C. Kaplan, E. Platonova, H. Eghlidi, and H. Ewers, “A simple, versatile method for GFP-based super-resolution microscopy via nanobodies,” *Nat. Methods*, vol. 9, no. 6, pp. 582–584, 2012, doi: 10.1038/nmeth.1991.

[130] H. Deschout *et al.*, “Precisely and accurately localizing single emitters in fluorescence microscopy,” *Nat. Methods*, vol. 11, no. 3, pp. 253–266, 2014, doi: 10.1038/nmeth.2843.

[131] C. Morey, C. N. Kienle, T. H. Klöpper, P. Burkhardt, and D. Fasshauer, “Evidence for a conserved inhibitory binding mode between the membrane fusion assembly factors Munc18 and syntaxin in animals.,” *J. Biol. Chem.*, vol. 292, no. 50, pp. 20449–20460, Dec. 2017, doi: 10.1074/jbc.M117.811182.

[132] K. P. Stepien, E. A. Prinslow, and J. Rizo, “Munc18-1 is crucial to overcome the inhibition of synaptic vesicle fusion by αSNAP,” *Nat. Commun.*, vol. 10, no. 1, pp. 1–18, 2019, doi: 10.1038/s41467-019-12188-4.

[133] M. G. Arnold, P. Adhikari, B. Kang, and H. Xu 徐昊, “Munc18a clusters SNARE-bearing liposomes prior to trans-SNARE zippering.,” *Biochem. J.*, vol. 474, no. 19, pp. 3339–3354, Sep. 2017, doi: 10.1042/BCJ20170494.

[134] P. Yin, N. R. Gandasi, S. Arora, M. Omar-Hmeadi, J. Saras, and S. Barg, “Syntaxin clusters at secretory granules in a munc18-bound conformation.,” *Mol. Biol. Cell*, vol. 29, no. 22, pp. 2700–2708, Nov. 2018, doi: 10.1091/mbc.E17-09-0541.

[135] Y.-K. Shin, “Two gigs of Munc18 in membrane fusion.,” *Proc. Natl. Acad. Sci. U. S. A.*, vol. 110, no. 35, pp. 14116–14117, Aug. 2013, doi: 10.1073/pnas.1313749110.

[136] Y. Schollmeier, J. M. Krause, S. Kreye, J. Malsam, and T. H. Söllner, "Resolving the Function of Distinct Munc18-1/SNARE Protein Interaction Modes in a Reconstituted Membrane Fusion Assay*," *J. Biol. Chem.*, vol. 286, no. 35, pp. 30582–30590, 2011, doi: https://doi.org/10.1074/jbc.M111.269886.

[137] P. Burkhardt, D. A. Hattendorf, W. I. Weis, and D. Fasshauer, "Munc18a controls SNARE assembly through its interaction with the syntaxin N-peptide.," *EMBO J.*, vol. 27, no. 7, pp. 923–933, Apr. 2008, doi: 10.1038/emboj.2008.37.

[138] W. K. Subczynski, M. Pasenkiewicz-Gierula, J. Widomska, L. Mainali, and M. Raguz, "High Cholesterol/Low Cholesterol: Effects in Biological Membranes: A Review.," *Cell Biochem. Biophys.*, vol. 75, no. 3–4, pp. 369–385, Dec. 2017, doi: 10.1007/s12013-017-0792-7.

[139] L. H. Chamberlain, R. D. Burgoyne, and G. W. Gould, "SNARE proteins are highly enriched in lipid rafts in PC12 cells: implications for the spatial control of exocytosis.," *Proc. Natl. Acad. Sci. U. S. A.*, vol. 98, no. 10, pp. 5619–5624, May 2001, doi: 10.1073/pnas.091502398.

[140] M. Vrljic, S. Y. Nishimura, W. E. Moerner, and H. M. McConnell, "Cholesterol depletion suppresses the translational diffusion of class II major histocompatibility complex proteins in the plasma membrane.," *Biophys. J.*, vol. 88, no. 1, pp. 334–347, Jan. 2005, doi: 10.1529/biophysj.104.045989.

[141] M. K. Weisgerber, A.W, Mahmood, A, Wehman, A.M., Knowles, "Molecular Regulation of Multivesicular Endosome Fusion and Exosome Secretion," *Exocytosis From Mol. to Cells*, vol. Chapter 15, 2022.

[142] E. Boilard, "Extracellular vesicles and their content in bioactive lipid mediators:

more than a sack of microRNA.," *J. Lipid Res.*, vol. 59, no. 11, pp. 2037–2046, Nov. 2018, doi: 10.1194/jlr.R084640.

[143] G. van Niel, G. D'Angelo, and G. Raposo, "Shedding light on the cell biology of extracellular vesicles.," *Nat. Rev. Mol. Cell Biol.*, vol. 19, no. 4, pp. 213–228, Apr. 2018, doi: 10.1038/nrm.2017.125.

[144] E. A. Nunez, J. Wallis, and M. D. Gershon, "Secretory processes in follicular cells of the bat thyroid. 3. The occurrence of extracellular vesicles and colloid droplets during arousal from hibernation.," *Am. J. Anat.*, vol. 141, no. 2, pp. 179–201, Oct. 1974, doi: 10.1002/aja.1001410203.

[145] C. Harding, J. Heuser, and P. Stahl, "Receptor-mediated endocytosis of transferrin and recycling of the transferrin receptor in rat reticulocytes.," *J. Cell Biol.*, vol. 97, no. 2, pp. 329–339, Aug. 1983, doi: 10.1083/jcb.97.2.329.

[146] B. T. Pan and R. M. Johnstone, "Fate of the transferrin receptor during maturation of sheep reticulocytes in vitro: selective externalization of the receptor.," *Cell*, vol. 33, no. 3, pp. 967–978, Jul. 1983, doi: 10.1016/0092-8674(83)90040-5.

[147] J. Clancy and C. D'Souza-Schorey, "Extracellular Vesicles in Cancer: Purpose and Promise.," *Cancer J.*, vol. 24, no. 2, pp. 65–69, 2018, doi: 10.1097/PPO.0000000000000306.

[148] M. Colombo, G. Raposo, and C. Théry, "Biogenesis, secretion, and intercellular interactions of exosomes and other extracellular vesicles," *Annu. Rev. Cell Dev. Biol.*, vol. 30, pp. 255–289, 2014, doi: 10.1146/annurev-cellbio-101512-122326.

[149] J. Kowal, M. Tkach, and C. Théry, "Biogenesis and secretion of exosomes.," *Curr. Opin. Cell Biol.*, vol. 29, pp. 116–125, Aug. 2014, doi: 10.1016/j.ceb.2014.05.004.

[150] J. Meldolesi, “Exosomes and Ectosomes in Intercellular Communication.,” *Curr. Biol.*, vol. 28, no. 8, pp. R435–R444, Apr. 2018, doi: 10.1016/j.cub.2018.01.059.

[151] W. Sun, J.-D. Luo, H. Jiang, and D. D. Duan, “Tumor exosomes: a double-edged sword in cancer therapy.,” *Acta Pharmacol. Sin.*, vol. 39, no. 4, pp. 534–541, Apr. 2018, doi: 10.1038/aps.2018.17.

[152] M. Tkach and C. Théry, “Communication by Extracellular Vesicles: Where We Are and Where We Need to Go.,” *Cell*, vol. 164, no. 6, pp. 1226–1232, Mar. 2016, doi: 10.1016/j.cell.2016.01.043.

[153] S. Mathivanan, C. J. Fahner, G. E. Reid, and R. J. Simpson, “ExoCarta 2012: database of exosomal proteins, RNA and lipids.,” *Nucleic Acids Res.*, vol. 40, no. Database issue, pp. D1241-4, Jan. 2012, doi: 10.1093/nar/gkr828.

[154] F. Momen-Heravi *et al.*, “Current methods for the isolation of extracellular vesicles.,” *Biol. Chem.*, vol. 394, no. 10, pp. 1253–1262, Oct. 2013, doi: 10.1515/hsz-2013-0141.

[155] S. N. Hurwitz, M. M. Conlon, M. A. Rider, N. C. Brownstein, and D. G. J. Meckes, “Nanoparticle analysis sheds budding insights into genetic drivers of extracellular vesicle biogenesis.,” *J. Extracell. vesicles*, vol. 5, p. 31295, 2016, doi: 10.3402/jev.v5.31295.

[156] B. H. Sung, T. Ketova, D. Hoshino, A. Zijlstra, and A. M. Weaver, “Directional cell movement through tissues is controlled by exosome secretion,” *Nat. Commun.*, vol. 6, no. 1, p. 7164, 2015, doi: 10.1038/ncomms8164.

[157] S. W. Messenger, S. S. Woo, Z. Sun, and T. F. J. Martin, “A Ca2+-stimulated exosome release pathway in cancer cells is regulated by Munc13-4,” *J. Cell Biol.*,

vol. 217, no. 8, pp. 2877–2890, 2018, doi: 10.1083/jcb.201710132.

[158] F. J. Verweij *et al.*, “Quantifying exosome secretion from single cells reveals a modulatory role for GPCR signaling,” *J. Cell Biol.*, vol. 217, no. 3, pp. 1129–1142, 2018, doi: 10.1083/jcb.201703206.

[159] F. J. Verweij *et al.*, “The power of imaging to understand extracellular vesicle biology in vivo.,” *Nat. Methods*, vol. 18, no. 9, pp. 1013–1026, Sep. 2021, doi: 10.1038/s41592-021-01206-3.

[160] B. H. Sung *et al.*, “A live cell reporter of exosome secretion and uptake reveals pathfinding behavior of migrating cells,” *Nat. Commun.*, vol. 11, no. 1, p. 2092, 2020, doi: 10.1038/s41467-020-15747-2.

[161] B. H. Sung and A. M. Weaver, “Exosome secretion promotes chemotaxis of cancer cells.,” *Cell Adh. Migr.*, vol. 11, no. 2, pp. 187–195, Mar. 2017, doi: 10.1080/19336918.2016.1273307.

[162] S. Sinha *et al.*, “Cortactin promotes exosome secretion by controlling branched actin dynamics.,” *J. Cell Biol.*, vol. 214, no. 2, pp. 197–213, Jul. 2016, doi: 10.1083/jcb.201601025.

[163] D. Hoshino *et al.*, “Exosome secretion is enhanced by invadopodia and drives invasive behavior.,” *Cell Rep.*, vol. 5, no. 5, pp. 1159–1168, Dec. 2013, doi: 10.1016/j.celrep.2013.10.050.

[164] P. Perrin *et al.*, “Retrofusion of intralumenal MVB membranes parallels viral infection and coexists with exosome release,” *Curr. Biol.*, vol. 31, no. 17, pp. 3884-3893.e4, 2021, doi: https://doi.org/10.1016/j.cub.2021.06.022.

[165] J. K. Jaiswal, N. W. Andrews, and S. M. Simon, “Membrane proximal lysosomes

are the major vesicles responsible for calcium-dependent exocytosis in nonsecretory cells.," *J. Cell Biol.*, vol. 159, no. 4, pp. 625–635, Nov. 2002, doi: 10.1083/jcb.200208154.